Atmos. Meas. Tech. Discuss., 3, 4967–5077, 2010
www.atmos-meas-tech-discuss.net/3/4967/2010/
doi:10.5194/amtd-3-4967-2010

Atmospheric Measurement Techniques Discussions

Statistically optimized inversion algorithm for enhanced retrieval of aerosol properties from spectral multi-angle polarimetric satellite observations

O. Dubovik[1], **M. Herman**[1], **A. Holdak**[1], **T. Lapyonok**[1], **D. Tanré**[1], **J. L. Deuzé**[1], **F. Ducos**[1], **A. Sinyuk**[3], **and A. Lopatin**[1,2]

[1]Laboratoire d'Optique Atmosphérique, CNRS UMR 8518, Université de Lille 1, Villeneuve d'Ascq, France
[2]Institute of Physics, Laboratory of Scattering Media, 68 Nezavisimosti avenue, Minsk, 220072, Belarus
[3]NASA/GSFC, Greenbelt, MD, USA

Received: 7 August 2010 – Accepted: 25 October 2010 – Published: 16 November 2010

Correspondence to: O. Dubovik (dubovik@loa.univ-lille1.fr)

Published by Copernicus Publications on behalf of the European Geosciences Union.

Abstract

The proposed development is an attempt to enhance aerosol retrieval by emphasizing statistical optimization in inversion of advanced satellite observations. This optimization concept improves retrieval accuracy relying on the knowledge of measurement error distribution. Efficient application of such optimization requires pronounced data redundancy (excess of the measurements number over number of unknowns) that is not common in satellite observations. The POLDER imager on board of the PARASOL micro-satellite registers spectral polarimetric characteristics of the reflected atmospheric radiation at up to 16 viewing directions over each observed pixel. The completeness of such observations is notably higher than for most currently operating passive satellite aerosol sensors. This provides an opportunity for profound utilization of statistical optimization principles in satellite data inversion. The proposed retrieval scheme is designed as statistically optimized multi-variable fitting of the all available angular observations of total and polarized radiances obtained by POLDER sensor in the window spectral channels where absorption by gaseous is minimal. The total number of such observations by PARASOL always exceeds a hundred over each pixel and the statistical optimization concept promises to be efficient even if the algorithm retrieves several tens of aerosol parameters. Based on this idea, the proposed algorithm uses a large number of unknowns and is aimed on retrieval of extended set of parameters affecting measured radiation.

The algorithm is designed to retrieve complete aerosol properties globally. Over land, the algorithm retrieves the parameters of underlying surface simultaneously with aerosol. In all situations, the approach is anticipated to achieve a robust retrieval of complete aerosol properties including information about aerosol particle sizes, shape, absorption and composition (refractive index). In order to achieve reliable retrieval from PARASOL observations even over very reflective desert surfaces, the algorithm was designed as simultaneous inversion of a large group of pixels within one or several images. Such, multi-pixel retrieval regime takes advantage from known limitations

on spatial and temporal variability in both aerosol and surface properties. Specifically the variations of the retrieved parameters horizontally from pixel-to-pixel and/or temporary from day-to-day are enforced to be smooth by additional appropriately set a priori constraints. This concept is expected to provide satellite retrieval of higher consistency, because the retrieval over each single pixel will be benefiting from co-incident aerosol information from neighboring pixels, as well, from the information about surface reflectance (over land) obtained in preceding and consequent observations over the same pixel.

The paper provides in depth description of the proposed inversion concept, illustrates the algorithm performance by a series of numerical tests and presents the examples of preliminary retrieval results obtained from actual PARASOL observations. It is should be noted that many aspects of the described algorithm design considerably benefited from experience accumulated in the preceding effort on developments of currently operating AERONET and PARASOL retrievals, as well as, several core software components were inherited from those earlier algorithms.

1 Introduction

The research presented in this paper aims to develop new retrieval algorithm optimized for deriving maximum information content using the data redundancy available from advanced satellite observations, such as those from POLDER/PARASOL observations. The design of POLDER imager allows collecting rather comprehensive characterization of angular distribution of both total and polarized radiation reflected to the space. The observations in window channels where the effect of absorption by atmospheric gases are minimal are usually used for aerosol retrievals. The complete set of such observations collected operationally by POLDER/PARASOL over each pixel includes angular measurements of both total and polarized radiances at 0.49, 0.675 and 0.87 µm and angular measurements of only total radiances at 0.44, 0.565 and 1.02 µm. The

AMTD

3, 4967–5077, 2010

number of viewing directions is similar for all spectral channels and varies from 14 to 16 depending on observed geographical location.

The completeness of such observations is significantly higher comparing to any currently operating passive satellite aerosol sensors. In addition PARASOL provides nearly global coverage every 2 days. Therefore, such complete set of PARASOL observations potentially provides very valuable basis for enhanced characterization of global aerosol.

However, rigorous interpretation of redundant satellite observation is a very challenging task. Indeed, the optimized inversion requires applying complex multi-variable inversion algorithms. Such methods are time-consuming and challenging for implementation. This is why the rigorous methods of inversion optimization are not generally used for processing very large data sets provided by satellite aerosol imagers. Instead, most of satellite aerosol retrievals use the look-up tables of simulated satellite signals pre-computed for some limited selected scenarios of aerosol and underlying surface combinations. The modeled scenario that provides the best match of the observed radiances is accepted as the retrieved solution. With some modification, this strategy is adopted in the most of aerosol satellite retrievals because it allows rapid operational processing of satellite images. For example, it is successfully employed in retrievals of single-view AVHRR (Stowe et al., 1997; Mishchenko et al., 1999; Higurashi and Nakajima 1999), TOMS (Torres et al., 1998), MODIS (Kaufman et al., 1997; Tanré et al., 1997; Remer et al., 2005), etc. At the same time, applying the same methodology for processing observations from imagers with multi-viewing capabilities, such as MISR (Diner et al., 1998; Martonchik et al., 1998; Kahn et al., 2007, 2009), SEVIRI (Govaert et al., 2010; Wagner et al., 2010; Carrer et al., 2010), or POLDER (Deuzé et al., 2001; Herman et al., 2005), reveals some deficiencies of the look-up table retrievals. The multi-directional observations have notably higher sensitivity to the details of aerosol and surface properties, and the retrieval of larger number of parameters is expected. Correspondingly, the required comprehensive look-up tables of such observations may have larger dimensions and, thus, be less suitable for operational use.

AMTD

3, 4967–5077, 2010

Statistically optimized inversion algorithm for enhanced retrieval

O. Dubovik et al.

As a result, most look-up table based algorithms rely only on the selected sub-sets of the observations with highest sensitivity to the aerosol parameters and retrieve reduced set of characteristics. For example, the current POLDER/PARASOL operational retrieval algorithm over ocean (Herman et al., 2005) uses only total and polarized radiances at two spectral channels (0.67 and 0.87 µm). The look-up table algorithm works efficiently for these two channels because they are sensitive to the scattering of both fine and coarse mode aerosols and are insensitive to vertical variability of aerosol and not strongly affected by water-leaving radiation. The POLDER/PARASOL retrieval over land (Deuzé et al., 2001) uses only polarized radiance at the same two channels. Such strategy is used because the contribution of aerosol into reflected polarized radiance generally dominates over the contribution of the land reflectance, while contribution of land surface into total reflected radiance is usually comparable or stronger than that of aerosol. Therefore, as discussed by Deuzé et al. (2001), utilization of only polarized radiances allows one to derive aerosol properties and to avoid challenging issue of separation of surface and aerosol contributions into the total reflectance. Although this algorithm has successfully provided valuable aerosol retrievals from POLDER observations, several shortcomings were identified in the POLDER aerosol products. First, PARASOL retrieval over land provides information only about fine aerosol particles, because the contribution of large aerosol over land (predominantly non-spherical dust) to the polarized reflected radiances is often small. In addition, the correct interpretation of PARASOL observations of desert dust even over ocean surface is challenging due to difficulties to model appropriately the light scattering by non-spherical particles of desert dust (Gérard et al., 2005). Second, since the PARASOL algorithm, both over land and ocean, relies on the observations of only two spectral channels, the retrieved aerosol spectral properties are not always fully consistent with the observations at other channels.

The retrieval algorithm proposed here fits the complete set of PARASOL observation in all spectral channels (with the exception of the channels dominated by gaseous absorption such as 0.763, 0.765 and 0.910 µm) and including both measurements of total

AMTD
3, 4967–5077, 2010

radiances and polarized radiances (if available). Based on this strategy, the algorithm is driven by larger number of unknown parameters and aimed on retrieval of an extended set of parameters affecting measured radiation. For example, the approach allows the retrieval of both the optical properties of aerosol and underlying surface from PARASOL observations over land. Also, comparing to the current operational PARASOL retrieval, the proposed algorithm is designed to provide more detailed information about aerosol properties including the particle size distribution, complex refractive index, parameters characterizing aerosol particle shape and vertical distribution. This setup of the aerosol retrieval algorithm is based on accumulated experience and current understanding the high potential of using spectral multi-angular polarimetric observations form space for improving global aerosol monitoring. Diverse aspects of aerosol retrieval improvements by using advanced satellite observations have been already demonstrated and outlined in numerous previous studies. For example, the studies by Kahn et al. (2007, 2009), Kalashnikova et al. (2005), Kalashnikova and Kahn (2006) demonstrated the possibility of deriving not only aerosol loading but also some information about aerosol particle size, morphology and shape from observations by MISR imager that provides multiple view observations of total reflectance in 9 directions in 4 spectral channels (0.44, 0.55, 0.67 and 0.87 µm). These studies have suggested a high importance of using multi-angular observation geometry for deriving more detailed aerosol information. However, most of known comparisons of the aerosol parameters derived from multi-viewing images (such as MISR and POLDER) with the aerosol products of single view satellite sensors do not indicate clear advantage of multi-viewing observation for aerosol monitoring. For example, Kokhanovsky et al. (2007) compared the aerosol retrievals obtained from different satellite platforms over land with ground-based AERONET observations and indicated significant differences in currently available satellite products and did not reveal any notable advantage of one particular satellite sensor. The study suggested that retrieval indeterminacies are likely part of the observed discrepancies, and their reduction will likely be aided by new missions incorporating spectral multi-angular polarimeters. Indeed, sensitivity analysis of Mishchenko and Travis (1997a)

AMTD
3, 4967–5077, 2010

related the possibility of potential important improvements of satellite aerosol retrievals with use of spectral multi-angular polarization as well as intensity of reflected sunlight. Latter studies by Chowdhary et al. (2002, 2005) demonstrated the possibility of retrieving the detailed aerosol properties from spectral multi-angular Research Scanning airborne Polarimeter (RSP) over water. This polarimeter was aircraft-based prototype of the Aerosol Polarimetry Sensor (APS) the instrument projected to be a part of a future NASA Glory mission (Mishchenko et al., 2007). The analysis of RSP observations over land by Waquet et al. (2007, 2009) illustrated the possibility of reliable aerosol retrievals over reflective land surfaces. It should be noted here that Kokhanovsky et al. (2007) did not identify any superiority of POLDER results (included into the comparisons) over other satellite imagers. This fact has several probable explanations. First, although POLDER sensor has multi-viewing polarimetric capabilities, the spectral range of POLDER observation is notably narrower that spectral coverage of some single viewing sensors, such as a MODIS. (Similar remark is valid for comparisons on multi-viewing MISR satellite instrument.) Second, the algorithm processing POLDER observations was not designed to take full advantage of positive redundancy of spectral multi-angle polarimetric observations. Indeed, the POLDER retrieval algorithm by Deuzé et al. (2001) oriented on rapid operational processing uses only polarized radiances at only two visible spectral channels. Therefore, the positive polarimetric information from other spectral channels, as well as, any information from total reflectance observation was not used. Waquet et al. (2007) demonstrated that using polarimetirc observations in wider spectral range is essential for aerosol retrieval over land from polarimetry observations. Waquet et al. (2007, 2009) followed Deuzé et al. (2001) approach and used only polarized radiances. At the same time, Waquet et al. (2007, 2009) algorithm was driven by a large number of unknowns and was of significantly higher complexity than POLDER algorithm. Algorithm of such level of complexity has never been applied to POLDER/PARASOL observations. In addition, one could expect that including total reflectance into such enhanced retrieval scheme could result in additional improvements of the aerosol retrieval. Indeed, the spectral angular

AMTD
3, 4967–5077, 2010

measurements of total reflectance are shown to provide valuable aerosol information even over land surfaces (e.g. Martonchik et al., 2004; Liu et al., 2004; Kahn et al., 2005; Diner et al., 2005, etc). In addition, rigorous sensitivity studies suggest high importance of using observations of both total and polarized radiances for reliable aerosol retrieval (Mishchenko et al., 1997a; Hasekamp and Landgraf, 2007). That is why the retrieval concept described in this paper pursues inversion of both total and polarized radiances and includes implementations of several important algorithm refinements. The realization of this concept is expected to result into enhancement of completeness and accuracy of POLDER aerosol retrieval.

The presented algorithm developments essentially rely on the available positive research heritage from previous remote sensing aerosol retrieval developments, in particular those from the POLDER and AERONET retrieval activities. The general inversion scheme will be designed as multi-term Least Square Method (LSM) fitting by Dubovik and King (2000). Such inversion strategy allows for the use of a continuous space of solutions instead of a limited set of predetermined solutions as used in look-up table based algorithms. During more than a decade Dubovik and King (2000) algorithm was successfully employed for processing observation of AErosol RObothic NETwork (AERONET) of ground-based sun/sky-radiometers (Holben et al., 1998). During this period the algorithm has passed notable evolution and several useful modifications were added into inversion procedure. The modifications of that algorithm were effectively applied for interpretation of co-incident up and down-looking remote sensing observations. For example, Sinuyk et al. (2007) conducted the retrieval of both atmospheric aerosol and land surface properties from a combination of AERONET data with co-incident MISR or POLDER satellite observations. Gatebe et al. (2010) implemented the joint retrieval of detailed properties of multi-layered aerosol and underlying surface reflectance from a combination of AERONET data and airborne measurements by Cloud-Absorption Radiometer (CAR). The main details of the resulting fine-tuned numerical inversion scheme are discussed by Dubovik (2004) and below in the Sect. 3 of current paper. The modeling of PARASOL observed reflectances is implemented using approaches and computer codes developed previously for accurate computing radiative transfer equation solution, modeling aerosol single scattering and surface reflectance properties. Specifically, the multiple solar light interactions with the atmosphere and underlying surface are accounted using the successive order of scattering radiative transfer code by Lenoble et al. (2007). This approach and actual computer code have been used and refined in POLDER-1, POLDER-2 and POLDER/PARASOL data analysis. The land surface reflectance of total solar radiance is approximated by the model of Rahman et al. (1993) that has already been successfully used for interpretation of MISR (e.g. Martonchik et al., 1998), SEVIRI (e.g. Govaert et al., 2010) and RSP (e.g. Litvinov et al., 2010a) observations. The reflectance of polarized radiation by land surface is approximated by using the models developed by Nadal and Breon (1999) and Maignan et al. (2009) from the observations by POLDER. These models were also validated by RSP observations (Litvinov et al., 2010a). The modeling of aerosol single scattering properties is adopted from AERONET developments. This scattering model seems rather suitable for applying to multi-angular polarimetric observations, since this model was demonstrated to accurately reproduce the observations by ground-based radiometers that have high sensitivity to the fine features of angular and spectral aerosol scattering. For example, the software developed by Dubovik et al. (2006) for AERONET allows for very fast simulations of scattering by non-spherical aerosol. As discussed by Herman et al. (2005) and Gérard et al. (2005) the adequate modeling of scattering by non-spherical aerosol particles is critical for analysis of PARASOL observations.

In addition, as a part of PARASOL aerosol algorithm improvement, a new aspect has been introduced into the concept of satellite data inversion. Specifically, in order to overcome some difficulties related with the limited information of the PARASOL observations over single pixel, the retrieval is organized as simultaneous inversion of a large group of pixels within one or several images. For example, derivation of aerosol properties over bright lands is known as an extremely difficult task. The multi-pixel retrieval regime takes advantages from known limitations on spatial and temporal variability in both aerosol and surfaces properties. Similar ideas have already been used in different forms for improving satellite retrievals. For example, Martonchik et al. (1998) derive the surface reflectance properties from a group of near-by MISR pixels in the zone of 16 × 16 km relying on similarity of aerosol properties over this area. Govaerts et al. (2010) have built the SEVIRI aerosol and surface retrieval concept assuming rather limited time variability of the land surface reflectance properties. Even more explicitly the idea was used in studies by Lyapustin et al. (2008) and Lyapustin and Wang (2009), who used the limited time variability of land surface for screening cloud-contaminated data or the limited space variability of aerosol properties for constraining aerosol retrieval from MODIS observations. Here, the satellite retrieval is designed as statistically optimized simultaneous fitting the observations over a group of pixels implemented under additional inter-pixel constraints. Specifically the variations of the retrieved parameters horizontally from pixel-to-pixel or temporary from day-to-day over the same pixel are limited by the additional a priori constraints, in the similar manner as it is applied in inverse modeling by Dubovik et al. (2008). The inclusion of these additional constraints is expected to provide retrieval of higher consistency for aerosol retrievals from satellites, because the retrieval over each single pixel will be benefiting from co-incident aerosol information from neighboring pixels, as well, from the information about surface reflectance (over land) obtained in preceding and consequent observations over the same pixel.

It should be noted that this paper focuses on detailed implementation of core ideas for a new PARASOL retrieval algorithm, however it does not address many aspects for operational implementation of the algorithm. For example, issues such as cloud-screening, retrieval time requirements and other important aspects of algorithm implementation for operational processing are to be addressed in follow-on studies.

2 General structure of the algorithm

The general structure of the algorithm is shown in Fig. 1. In order to make the algorithm more flexible it is divided into several interacting but rather independent modules. Each module has rather particular function. The interactions between the modules are minimized to straightforward exchange of very limited set of parameters. The “Forward Model” and “Numerical Inversion” are two most complex and elaborated modules in the developed algorithm. The organization of the algorithm by modules enhances the flexibility in algorithm utilization. For example, the “Numerical Inversion” module implements quite universal operations that have no particular relations to the physical nature of the inverted observations. This module can, in principle, be used in any other application not related to atmospheric remote sensing. The “Forward Model” module does not have such universal applicability as the “Numerical Inversion” module. Nonetheless, the “Forward Model” module is developed in a quite universal way allowing modeling quite broad variety of atmospheric remote sensing. As a result of such organization of the algorithm, it can equally be applied (with minimal changes) for inverting observations from other satellite sensor or from ground. In addition such algorithm structure was helpful in adapting physical models and computer routine fragments inherited from previous AERONET and POLDER developments.

The following several Sections of the paper provide full description of the “Forward Model” and “Numerical Inversion” algorithm modules. A number of optional adjustments are suggested for setting both aerosol physical model and retrieval scheme. Although the algorithm is tuned for inverting PARASOL observations, some aspects of aerosol parameterization and inversion implementation (in particular a priori constraint settings) can be modified and adjusted for optimizing the algorithm performance if it is applied to other remote sensing observations. For example, two alternative strategies are suggested for implementing numerical inversion of satellite images observations: conventional pixel-by-pixel inversion and a new multi-pixel inversion strategy. According to this new multi-pixel approach, the retrieval developed as simultaneous inversion

AMTD
3, 4967–5077, 2010

of a large group of pixels within one or several images. Such retrieval regime takes advantage from known limitations on spatial and temporal variability in both aerosol and surface properties.

3 Forward model of POLDER/PARASOL observations

The aerosol retrieval algorithm is designed to invert the POLDER/PARASOL observations acquired in window channels shown in Table 1, that is: the total radiance in 6 window channels: 0.44, 0.49, 0.565, 0.675, 0.87 and 1.02 µm, and the polarized radiance in 3 of these channels: 0.49, 0.675 and 0.87 µm, reflected by a ground pixel. In each channel, observations of the same pixel are performed nearly simultaneously in up to 16 viewing directions (Deschamps et al., 1994). It is assumed that the reflected light consists in linearly polarized light. In the 3 polarized channels, besides the total reflected radiance, I, the measurements provide the polarized radiance, in the form of the 2 Stokes' parameters Q and U referred to axes perpendicular and parallel to the local meridian plane, i.e. $Q = I_p \cos(2\alpha)$ and $U = I_p \sin(2\alpha)$ where I_p is the polarized reflected radiance and α is the angle between the meridian plane and the polarization direction.

Let $\boldsymbol{I} = (I, Q, U, V)^T$ and $\boldsymbol{E}_0 = (E_0,\ 0,\ 0,\ 0)^T$ stand, respectively, for the Stokes' vectors of the observed electromagnetic radiation and of the incident un-polarized solar radiation; the subscript "T" denotes transposition and V is assumed to be negligible. The Stokes' vector $\boldsymbol{I} = (I,\ Q,\ U,\ V)^T = \boldsymbol{I}(\mu_0; \mu_1; \varphi_0; \varphi_1; \lambda)$ depends on the solar zenith angle ϑ_0 ($\mu_0 = \cos(\vartheta_0)$), the observation zenith angle ϑ_1 ($\mu_0 = \cos(\vartheta_1)$), the solar and observation azimuth angles φ_0 and φ_1, and wavelength λ. The reflected radiance may be written:

$$\boldsymbol{I}\,(\mu_0; \mu_1; \varphi_0; \varphi_1; \lambda) \ = \ \mathbf{L}\ \left[\mathbf{M}_{\mathrm{scat}}\,(\Theta;\ \lambda)\ +\ \mathbf{M}_{\mathrm{reflec}}\,(\mu_0; \mu_1; \varphi_0; \varphi_1; \lambda)\right]\ \boldsymbol{E}_0\ +\ \text{mult. scat.}, \quad (1)$$

where the terms $\mathbf{M}_{\mathrm{scat}}$ and $\mathbf{M}_{\mathrm{reflec}}$ correspond to the light reflected as a result of single interaction of incident solar light, respectively, with the atmosphere and surface. In

AMTD
3, 4967–5077, 2010

Eq. (1) it is assumed that polarized light is referred to axes perpendicular and parallel to the scattering and reflection planes (here, both formed by the solar and viewing directions); and the matrix **L** transforms the Stokes' vector into the plane of observations (details are given inreferred to Lenoble et al., 2007).

Under assumption of plane parallel multi-layered atmosphere, the single scattering term, $\mathbf{M}_{\mathrm{scat}}$, at the top of the atmosphere can be expressed as:

$$\mathbf{M}_{\mathrm{scat}}\left(\Theta;\lambda\right) = \frac{\mu_0}{\mu_0+\mu_1} \sum_{i=1,\ \dots,\ N} \left(e^{-m\tau_{i-1}} \left(1 - e^{-m\Delta\tau_i}\right) \frac{\omega_0^i}{4\pi} \mathbf{P}_i\left(\Theta;\lambda\right) \right), \tag{2}$$

where $\Delta\tau_i$ is the optical thickness of the i-th atmospheric layer ($i=1$, ..., N numbered from the top to the bottom of the atmosphere) and τ_i is the optical depth of the bottom of layer i (i.e. $\tau_i = \sum_{k=1,\ \dots,\ j} \Delta\tau_k$); $\mathbf{P}_i(\Theta;\lambda)$ and ω_0^i denote the phase matrix and single scattering albedo of the i-th atmospheric layer.

The optical properties τ_i, $\mathbf{P}_i(\Theta;\lambda)$ and ω_0^i of each atmospheric layer include the contributions of aerosol (characterized in i-th layer by $\Delta\tau_{i,\mathrm{a}}$, $\omega_{0,j}^{\mathrm{a}}$ and $\mathbf{P}_i^{\mathrm{a}}(\Theta;\lambda)$), molecular scattering (characterized in i-th layer by $\Delta\tau_{i,\mathrm{mol}}$, $\omega_{0,j}^{\mathrm{mol}}=1$ and $\mathbf{P}_i^{\mathrm{mol}}(\Theta;\lambda)$) and atmospheric gases (characterized in i-th layer by $\Delta\tau_{i,\mathrm{gas}}$ and $\omega_{0,j}^{\mathrm{gas}}=0$). The resulting single scattering albedo ω_0^i and phase matrix $\mathbf{P}_i(\Theta;\lambda)$ of the i-th atmospheric layer are:

$$\omega_0^i = \frac{\omega_{0,i}^{\mathrm{a}}\,\Delta\tau_{i,\mathrm{a}} + \Delta\tau_{i,\mathrm{mol}}}{\Delta\tau_{i,\mathrm{a}} + \Delta\tau_{i,\mathrm{mol}} + \Delta\tau_{i,\mathrm{gas}}}, \tag{3}$$

and

$$\mathbf{P}_i\left(\Theta;\lambda\right) = \frac{\omega_0^{\mathrm{a}}\Delta\tau_{i,\mathrm{a}}\,\mathbf{P}_i^{\mathrm{a}}\left(\Theta;\lambda\right) + \Delta\tau_{i,\mathrm{mol}}\,\mathbf{P}_i^{\mathrm{mol}}\left(\Theta;\lambda\right)}{\Delta\tau_{i,\mathrm{a}} + \Delta\tau_{i,\mathrm{mol}} + \Delta\tau_{i,\mathrm{gas}}}, \tag{4}$$

AMTD
3, 4967–5077, 2010

and the extinction optical thickness, τ, of the atmosphere is the sum of the corresponding components:

$$\tau = \tau_a + \tau_{mol} + \tau_{gas}. \tag{5}$$

The properties of atmospheric molecular scattering τ_{mol} and $\mathbf{P}^{mol}(\Theta;\lambda)$ are well known and can be calculated prior observations with sufficient accuracy. The extinction of atmospheric gases τ_{gas} has rather minor contributions in the POLDER/PARSOL window channels and can be accounted using known climatologies, as well as using available information from ancillary observations. For example, the present development uses the same procedure as used in the operational algorithm by Deuzé et al. (2001). That procedure corrects the water vapor absorption using PARASOL measurements in 0.910 µm spectral band. The minor absorption from ozone, NO_2 and O_2 are accounted using the climatology data. Thus, the most challenging part in modeling single scattering properties of the atmosphere is the modeling of aerosol contribution, i.e. aerosol extinction τ_a, single scattering albedo ω_0^a and phase matrix $\mathbf{P}^a(\Theta;\lambda)$. These properties depend on aerosol microphysics: particle size, shape and composition (refractive index). All these characteristics are driven by the parameters included in the vector of unknowns and correspondingly they retrieved from the observations.

The single reflection $\mathbf{M}_{reflec}$ at the top of atmosphere can be calculated as:

$$\mathbf{M}_{reflec}\,(\mu_0;\mu_1;\varphi_0;\varphi_1;\lambda) = \frac{\mu_0}{\pi}\, e^{-m\tau^*}\,\mathbf{R}\,(\mu_0;\mu_1;\varphi_0;\varphi_1;\lambda) \tag{6}$$

where reflection matrix $\mathbf{R}(\mu_0;\mu_1;\varphi_0;\varphi_1;\lambda)$ describes the surface reflection properties in the plane formed by the solar and viewing directions. For the ocean surface the reflection $\mathbf{R}(\mu_0;\mu_1;\varphi_0;\varphi_1;\lambda)$ is mainly governed by the wind speed at sea level as suggested by the Cox-Munk model (Cox and Munk, 1954) employed in the currently operational POLDER algorithm (Deuzé et al., 2001; Herman el al., 2005). In a contrast, the reflection matrix of land surface may differ very strongly from location to location. Therefore, in the present algorithm, the key properties of the land surface reflectance are included in the set of unknowns and retrieved from the observations.

Discussion Paper | Discussion Paper | Discussion Paper | Discussion Paper |

AMTD

3, 4967–5077, 2010

Statistically optimized inversion algorithm for enhanced retrieval

O. Dubovik et al.

As follows from Eq. (1), once the single scattering terms $\mathbf{M}_{\text{scat}}$ and $\mathbf{M}_{\text{reflec}}$ are defined one needs to account for multiple interactions of scattered light with atmosphere and surface. In the present algorithm these interactions are accounted by rigorously solving radiative transfer equation. Thus, the forward model of reflected radiances measured by POLDER/PARASOL contains three main modeling components: (i) aerosol single scattering, (ii) surface reflection and (iii) solving full radiative transfer equation for accounting for multiple scattering. The following parts of this section will describe each of these components in details.

It should be noted, that forward model for reproducing PARASOL/POLDER observations is designed by means of adapting the atmospheric modeling strategies and computer routines developed within previous POLDER and AERONET activities. At the same time, several important modifications required for optimizing the forward modeling performance have been implemented in present PARASOL algorithm. Specifically, the models of land surface reflectance have been introduced into the radiative transfer calculations, the number of aerosol parameters driving the model has been reduced, the different regimes of the radiative transfer calculations have been designed for allowing faster but less accurate calculations. These and other forward model modification allowed the performance of the developed "on-line" inversion procedure to attain the standards required for operational processing (achieving sufficient speed of computations, etc).

Figure 2 shows the data flow within the "Forward model" block of the algorithm. Three main complementary efforts are involved in the modeling atmospheric radiation filed observed by POLDER sensor:

- Modeling of single scattering properties of the atmospheric aerosol;
- modeling of the surface reflectance properties;
- Accounting for multiple scattering effects using full radiative transfer model.

These aspects are described in details below in this Section.

AMTD
3, 4967–5077, 2010

3.1 Aerosol single scattering properties

The modeling of the aerosol scattering matrices has been implemented following the ideas employed in AERONET retrieval algorithm by Dubovik and King (2000), Dubovik et al. (2002b, 2006).

In order to account for aerosol non-sphericity, the atmospheric aerosol is modeled as an ensemble of randomly oriented spheroids. Specifically, AERONET operational retrieval uses the concept by Dubovik et al. (2006) and models the particles for each size bin as mixture of spherical and non-spherical aerosol components. The non-spherical component was modeled by ensemble of randomly oriented spheroids (ellipsoids of revolution). According to this concept, the modeling of the total aerosol optical thickness τ of non-spherical aerosol can be written as the following:

$$\tau(\lambda) = \int_{r_{\min}}^{r_{\max}} \int_{\varepsilon_{\min}}^{\varepsilon_{\max}} c_{\tau}^{\varepsilon}(\lambda; k; n; r; \varepsilon) \frac{dN(\varepsilon)}{d\ln r} \frac{dN(r)}{d\ln r} d\ln\varepsilon \, d\ln r, \tag{7}$$

where $c_{\tau}^{\varepsilon}(\lambda; k; n; r; \varepsilon)$ denotes the extinction cross-sections of spherical particle and randomly oriented spheroid, λ – wavelength, n and k – real and imaginary parts of the refractive index, ε spheroid axis ratio ($\varepsilon = a/b$, a – axis of spheroid rotational symmetry, b – axis perpendicular to the axis of spheroid rotational symmetry), r – radius of volume-equivalent sphere. The characteristics r and ε are used here for describing size and shape of the ensemble of spheroids. Analogously to the combination of a and b, the combination of r and ε allows unique definition of the spheroid shape instead. As discussed by Mishchenko et al. (1997), the usage of r and ε is convenient for separating the effect of particle shape and size in analysis of aerosol mixture light scattering. Then the functions $\frac{dN(r)}{d\ln r}$ and $\frac{dN(\varepsilon)}{d\ln r}$ denote the number particle size and the number particle shape (axis ratio) distributions accordingly.

AMTD
3, 4967–5077, 2010

For performing fast and accurate calculations of aerosol extinction by polydisperse non-spherical aerosols, the size and shape integration can be approximated by the double sum, e.g.

$$\int_{r_{\min}}^{r_{\max}} \int_{\varepsilon_{\min}}^{\varepsilon_{\max}} c_\tau^\varepsilon\,(\lambda;\,k;\,n;\,r;\,\varepsilon)\,\frac{d N\,(\varepsilon)}{d\,\ln r}\,\frac{d N\,(r)}{d\,\ln r}\,d\,\ln \varepsilon\,d\,\ln r \tag{8}$$

$$= \sum_{k=1,\,\ldots,\,N_\varepsilon}\ \sum_{k=1,\,\ldots,\,N_\varepsilon} \mathbf{K}_\tau^\varepsilon\,(\lambda;\,k;\,n;\,r_i;\,\varepsilon_k)\,\frac{d N\,(\varepsilon_k)}{d\,\ln r}\,\frac{d V\,(r_i)}{d\,\ln r},$$

where

$$\mathbf{K}_\tau^\varepsilon\,(\lambda;\,k;\,n;\,r_i;\,\varepsilon_k) = \int_{\ln r_i-\Delta\ln r}^{\ln r_i+\Delta\ln r}\ \int_{\ln\varepsilon_k-\Delta\ln\varepsilon}^{\ln\varepsilon_k+\Delta\ln\varepsilon} \frac{c_\tau^\varepsilon(\lambda;\,k;\,n;\,r;\,\varepsilon)}{v(r)}\,A_k\,(\varepsilon)\,B_i\,(r)\,d\,\ln\varepsilon\,d\,\ln r. \tag{9}$$

where $v(r)$ is the volume of particle, $\frac{dV(r)}{d\ln r} = v(r)\frac{dN(r)}{d\ln r}$ is the volume particle size distribution, $A_k(\varepsilon)$ and $B_i(r)$ are the functions providing correspondingly the interpolation of shape distribution between the selected points ε_k and the interpolation of size distribution the over selected points r_i. In study by Dubovik et al. (2002b, 2006), the coefficients $A_k(\varepsilon)$ for integrating over axis ratio were assumed as rectangular functions $A_k(\varepsilon) = \text{const}$. For approximating size distribution between the used size bins r_i, the trapezoidal approximation was chosen by Dubovik and King (2000). Such kind of interpolation is traditionally applied in aerosol applications (e.g. see Twomey, 1977), where the functions $B_i(r)$ are defined as isosceles triangles.

It should be noted that in Eq. (8) the integral over sized is approximated by a sum using values of volume size distribution $dV(r)/d\ln r$ (in place of the number size distribution $dN(r)/d\ln r$) defined in logarithmically equidistant points r_i. Correspondingly, $v(r)$ denotes the volume of the particle. Both the volume size distribution and logarithm of radius were chosen for the convenience of the algorithm implementation. In principle, the particle number distributions $dN(r)/d\ln r$ or $dN(r)/dr$ could be equally used

AMTD
3, 4967–5077, 2010

in Eq. (8) (e.g. see King et al., 1978; King 1982). At the same time, the usage of both the volume of the particle (instead of number) and logarithmic scale in binning of the size distribution helps to optimize the approximation given by Eq. (8). First, these choices help to improve the accuracy of this approximation (a smaller number of points N_r provides appropriate accuracy). Second, under this representation, the kernels $\mathbf{K}_\tau^\varepsilon(\lambda;\, k;\, n;\, r_i;\, \varepsilon_k)$ for different points r_i are closer in the values. This is one of favorable condition for implementing inversion. Therefore, volume size distribution $dV(r)/d\ln r$ is often used as retrieved aerosol characteristic in the algorithms applied to invert the optical data of high sensitivity to aerosol particle size. For example, the similar size distribution representation was used in earlier studies by Nakajima et al. (1983, 1996) for retrieving aerosol properties from ground-based sky-radiometers. In AERONET retrieval, Dubovik and King (2000) represented volume size distribution $dV(r)/d\ln r$ by $N_r = 22$ points r_i. These points are equidistant in logarithmic space and cover size range from 0.05 to 15 microns. This size range was chosen following the sensitivity analysis by Dubovik et al. (2000), which showed that the aerosol particles of smaller and larger sizes produce negligible contribution into AERONET radiometer observations. This range of aerosol particle sizes is slightly wide than the one used in the earlier studies by Nakajima et al. (1996). As discussed later in this paper, the size range of aerosol is modified for retrieving aerosol from PARASOL observations.

Using the approximation given by Eqs. (8–9), Dubovik et al. (2006) has developed a numerical tool for fast calculations of scattering properties of spheroid mixture. The quadrature coefficients $K_\tau^\varepsilon(\lambda;\, k;\, n;\, r_i;\, \varepsilon_k)$ for the extinction, as well as, for absorption cross-sections and scattering matrices have been calculated and stored into the look-up tables for a wide range of n and k ($1.3 \le n \le 1.7$; $0.0005 \le k \le 0.5$). The calculations were done for spheroids with axis ratio ε ranging from ~0.3 (flattened spheroids) to ~3.0 (elongated spheroids) and for 41 narrow size bins covering the size-parameter range from ~0.012 to ~625. The look-up tables were arranged into a software package allowing fast, accurate, and flexible modeling of scattering by randomly oriented spheroids with different size and shape distributions. In addition, Dubovik et al. (2006)

AMTD
3, 4967–5077, 2010

used the developed software and showed that spheroids can closely reproduce single-scattering matrices of mineral dust measured in laboratory by Volten et al. (2001). It was shown that scattering matrices have rather limited sensitivity to the minor details of axis ratio distribution $\frac{dN(\varepsilon_k)}{d\ln r}$. Therefore, Dubovik et al. (2006) have suggested and demonstrated that AERONET retrieval may rely on rather simple assumption that shape (axis ratio) distribution $\frac{dN(\varepsilon_k)}{d\ln r}$ in the non-spherical fraction of any tropospheric aerosol is the same. Based on this conclusion the aerosol scattering model was set in AERONET retrieval as a mixture of *spherical* and *non-spherical* fractions, and $\frac{dN(\varepsilon_k)}{d\ln r}$ obtained by Dubovik et al. (2006) from fitting Volten et al. (2001) observations was employed as shape distribution for *non-spherical* fraction. Based on this assumption, the integration over ε in Eq. (7) can be done once for all for each size bins, and, therefore, the calculations of aerosol optical properties ($\tau_a(\lambda)$, ω_0^a and $\mathbf{P}^a(\Theta;\lambda)$) in AERONET retrieval is implemented in a practically convenient form. For example, for modeling $\tau_a(\lambda)$ one can write:

$$\tau_a(\lambda) = \tau_{sph}(\lambda) + \tau_{nons}(\lambda) = \sum_{i=1,\ldots,N_r} \left(C_{sph}\,\mathbf{K}_\tau^{sph}(\lambda;k;n;r_i) + (1 - C_{sph})\,\mathbf{K}_\tau^{nons}(\lambda;k;n;r_i)\right)\frac{dV(r_i)}{d\ln r}, \tag{10a}$$

where

$$\mathbf{K}_\tau^{sph}(\lambda;k;n;r_i) = \int_{\ln r_i - \Delta\ln r}^{\ln r_i + \Delta\ln r} \frac{c_\tau^{sph}(\lambda;k;n;r)}{v(r)} B_k(r)\, d\ln r, \tag{10b}$$

Discussion Paper | Discussion Paper | Discussion Paper | Discussion Paper |
AMTD
3, 4967–5077, 2010
Statistically optimized inversion algorithm for enhanced retrieval
O. Dubovik et al.

$$\mathbf{K}_{\tau}^{\text{nons}}(\lambda;k;n;r_i) = \int\limits_{\ln r_i-\Delta \ln r}^{\ln r_i+\Delta \ln r} B_i(r) \tag{10c}$$

$$\left(\int\limits_{\varepsilon_{\min}}^{\varepsilon_{\max}} \frac{c_{\tau}^{\varepsilon}(\lambda;k;n;r;\varepsilon)}{v(r)} \frac{dN(\varepsilon)}{d\ln\varepsilon}\, d\ln\varepsilon\right) d\ln r,$$

where C_{sph} is the fraction of the spherical particles. Note, that while the preparation of the core look-up tables $\mathbf{K}_{\tau}^{\text{nons}}(\lambda;k;n;r_i)$ required several years of computations, the resulting software allows very fast simulations of scattering by non-spherical aerosols. The calculation takes a faction of a second for any realistic combination of aerosol size distribution and complex refractive index. At present, it is probably the only approach that can calculate scattering matrices for non-spherical particles as part of the retrieval without relying on look-up tables of scattering matrices. Once the forward model in AERONET retrieval was updated with non-spherical aerosol light scattering modeling capabilities by Dubovik et al. (2006) (as shown in Eq. 10) the fraction C_{sph} was included in the set of retrieved parameters along with the concentrations for 22 bins of size distribution.

It is noteworthy that the spheroid model developed by Dubovik et al. (2002b, 2006) appeared to be rather useful for AERONET and other aerosol remote sensing applications. First, the utilization of this model has significantly improved the AERONET operational retrieval of aerosol with pronounced coarse mode fraction (e.g. see Reid et al., 2003; Eck et al., 2005; Dubovik et al., 2006). The same model has been shown to reproduce adequately the ground-based polarimetric photometer observations of non-spherical desert dust. Specifically, the efficient application of the model to the polarimetric observations has been shown by Dubovik et al. (2006) for a case study and Li et al. (2009) for an extended series of the observations. In addition, it was shown that the spheroid model allows qualitative reproduction of the main characteristic features of lidar observations of non-spherical desert dust. For example, the increase of extinction-to-backscattering lidar ratio and a high depolarization of signal regularly observed in lidar observations of desert dust, and traditionally associated with aerosol particle non-sphericity, can be adequately reproduced using spheroid-based model (see discussion by Dubovik et al., 2006). Cattral at al. (2005) showed that lidar ratios calculated from aerosol properties derived from AERONET observations using spheroid model agree well with known lidar observations of desert dust. Furthermore, Veselovskii et al. (2010) have used the approach suggested by Dubovik et al. (2006) and incorporated the spheroid model into the algorithm retrieving aerosol properties from lidar observations. That is, probably, one of the first attempt to interpret quantitatively the sensitivity of the lidar observations to particle non-sphericity. The non-spherical coarse aerosol models derived from climatologies of AERONET retrievals had been successfully incorporated into MODIS and SEVIRI satellite retrieval (Levy et al., 2007a,b; Govaerts et al., 2010; Wagner et al., 2010). The AERONET retrievals are being used for making accurate calculations of atmospheric broadband fluxes and aerosol radiative forcing. These calculations were shown to agree very reasonably with available coincident ground-based flux observations in desert regions (Derimian et al., 2008) and globally (Garcia et al., 2008). Derimian et al. (2008) demonstrated that the neglect of desert dust non-sphericity in climatic assessment leads to ∼10% systematic overestimation of cooling of the atmosphere by desert dust aerosol on the top of the atmosphere.

The retrieval algorithm developed here for POLDER/PARASOL uses the same modeling strategy as described above. Correspondingly, solution is sought in continues space of aerosol size distribution parameters, aerosol particle shape and complex refractive indices (see Table 1). However, due to differences in information content of AERONET and POLDER measurements, the retrieved size distribution is represented by a smaller number of bins N_r. Instead of $N_r = 22$, retrieved by AERONET, here N_r is reduced to 16 and even significantly smaller numbers. In order to assure that the aerosol model remains adequate and its accuracy is acceptable even if number of aerosol bins is small, the performance of Dubovik et al. (2006) software

AMTD
3, 4967–5077, 2010

Statistically optimized inversion algorithm for enhanced retrieval

O. Dubovik et al.

was analyzed for situations corresponding to POLDER/PARASOL measurements with reduced number of aerosol bins. It was found that the accuracy of the calculations remains practically unchanged if the aerosol size bins corresponding to very small and very large particles have been eliminated, i.e. $N_r = 16$ covers size range from $r_{min} = 0.07\,\mu m$ to $r_{max} = 10\,\mu m$. The contribution of smaller and larger particles into POLDER/PARASOL observations is negligible. Nonetheless, the need for optimizing the software of Dubovik et al. (2006) by using even smaller number of aerosol bins: $N_r \leq 10$, was identified. It was found that sufficiently accurate modeling of POLDER/PARASOL observations can be achieved if the shape of each single bin is optimized. Specifically, utilizations of log-normally shaped bins provided notable improvements if $N_r \leq 10$. The conducted small series of calculations suggested some advantages of modeling aerosol size distribution as superposition of the log-normal functions with fixed parameters:

$$\frac{dV\ (r)}{d\ \ln r} = \sum_{i=1,\ \ldots,\ N} \frac{c_{V,i}}{\sqrt{2\ \pi}\sigma_i} \exp\left[-\frac{(\ln r\ -\ \ln r_{V,i})^2}{2\ \sigma_i^2}\right] = \sum_{i=1,\ \ldots,\ N} c_i \frac{dv_i\ (r)}{d\ \ln r}, \tag{11a}$$

i.e.

$$c_i\ =\ c_{V,i} \text{ and } \frac{dv_i\ (r)}{d\ \ln r} = \frac{1}{\sqrt{2\pi}\ \sigma_i} \exp\left[-\frac{(\ln r\ -\ \ln r_{V,i})^2}{2\ \sigma_i^2}\right]. \tag{11b}$$

For example, Fig. 3 illustrates that a small number of log-normal bins retains the realistically smooth shape of atmospheric aerosol size distribution, while applying triangular or trapezium approximation leads to appearance of inadequate features (apparent triangle tops) in the size distribution. Thus, the new option allowing the usage of log-normally shaped bins was included into Dubovik et al. (2006).

AMTD

3, 4967–5077, 2010

3.2 Modeling surface reflectance

The reflective properties of ocean surface are taken into account using Cox-Munk model (Cox and Munk, 1954) analogously to the currently operational POLDER algorithm (Deuzé et al., 2001; Herman el al., 2005). The modeling of the reflectance by the land surfaces has been adjusted to the needs of newly developed POLDER/PARASOL retrieval. The aerosol retrieval algorithm by Deuzé et al. (2001) over land relies only on the PARASOL measurements of polarized reflectance and, correspondingly, it does not consider the detailed directional scattering properties of total reflectance by land surface. Therefore, the "forward model" was modified to account adequately for both total and polarized properties of surface reflectance.

In remote sensing applications the effects of directionality of land surface reflectance are often accounted for by semi-empirical models driven by a small number of internal parameters. For example, the Ross-Li model (Ross, 1981; Li and Strahler, 1992; Wanner et al., 1995) is employed for characterization of directional properties of land surface reflectance derived from MODIS observation (Justice et al., 1998). The Rahman-Pinty-Verstraete (RPV) model (Rahman et al., 1993) is successfully used for the analysis of MISR observations by Martonchik et al. (1998) and SEVIRI by Govaerts et al. (2010) and Wagner et al. (2010). The comparisons of the models with satellite (Maignan et al., 2004, 2009) and aircraft (Litvinov et al., 2010a,b) data showed that, generally, both Ross-Li and RPV models are, comparably well, capable to reproduce the multi-angle observations of land surfaces. Since, RPV model was applied more extensively to interpretation multi-directional images (e.g. MISR, SEVIRI), it has been retained, in present POLDER/PARASOL algorithm, as a primary formulation for modeling Bi-directional Reflectance Function (BRF). Rahman et al. (1993) describe BRF as:

$$\rho_{\mathrm{RPV}}\left(\vartheta_1;\varphi_1;\vartheta_2;\varphi_2\right) = \rho_0 \frac{\cos^{k-1}\vartheta_1 \cos^{k-1}\vartheta_2}{\left(\cos\vartheta_1 + \cos\vartheta_2\right)^{k-1}} F\left(g\right)\left(1 + \frac{1-h_0}{1+G}\right), \tag{12a}$$

AMTD

3, 4967–5077, 2010

Statistically optimized inversion algorithm for enhanced retrieval

O. Dubovik et al.

$$F(g) = \frac{1 - \Theta^2}{\left[1 + \Theta^2 - 2\,\Theta \cos(\pi - \alpha_i)\right]^{1.5}} \tag{12b}$$

$$\cos\alpha_i = \cos\theta_1 \cos\theta_2 - \sin\theta_1 \sin\theta_2 \cos(\varphi_1 - \varphi_2), \tag{12c}$$

$$G = \left[\tan^2\theta_1 + \tan^2\theta_2 - 2\tan\theta_1 \tan\theta_2 \cos(\varphi_1 - \varphi_2)\right]^{1/2}. \tag{12d}$$

This model provides bi-directional reflectance as a function of four following empirical parameters: $\rho_o(\lambda)$ characterizes intensity of reflectance. $\kappa(\lambda)$ characterizes anisotropy of reflectance, $\Theta(\lambda)$ characterizes forward/backscattering contributions in total reflectance, $h_0(\lambda)$ is a "hot spot" parameter. All these parameters are considered as unknowns and included in the set of the retrieved parameters (see Table 1).

The available airborne and satellite polarimetric observations in the visible and infrared showed that the Bi-directional Polarized Reflectance Function (BPRF) of land surface tends to have rather small values (compared to BRF) with no spectral dependence (e.g., Rondeaux and Herman, 1991; Nadal and Breìon, 1999; Maignan et al., 2004, 2009; Waquet et al., 2009a,b; Litvinov et al., 2010a,b). Most theoretical models developed for approximating of observed BPRF are based on the Fresnel equations of light reflection from the surface. For example, Nadal and Breìon (1999) have proposed simple two-parameter non-linear function of the Fresnel reflection for characterization of atmospheric aerosol over land surfaces based on POLDER observations land surface reflectance. Recently, Maignan et al. (2009) have introduced a new linear BPDF model with only one free parameter and demonstrated that this simple model allows a similar fit to the POLDER measurements as more complex non-linear model by Nadal and Breìon (1999). This model has been used in the present POLDER/PARASOL retrieval algorithm as a primary model of polarized reflectance of land surface.

The model by Maignan et al. (2009) describes the polarized reflectance as:

$$\rho_s(\vartheta_1; \varphi_1; \vartheta_2; \varphi_2) = \rho_{\mathrm{Maignan}}\, F_{12}(\alpha_i, n), \tag{13a}$$

AMTD
3, 4967–5077, 2010

Statistically optimized inversion algorithm for enhanced retrieval

O. Dubovik et al.

where BPRF is given as linear function of polarized component $F_{12}(\alpha_i, n)$ of the Fresnel reflection matrix (dependent on incident angle α_i and refractive index n) multiplied by an empirical coefficient:

$$\rho_{\text{Maignan}}(\vartheta_1; \varphi_1; \vartheta_2; \varphi_2) = \frac{B \exp(-\tan(\alpha_i)) \exp(-v)}{4(\mu_0 + \mu_1)}. \tag{13b}$$

The attenuation term $\exp(-v)$ reflects the observed tendency of decreasing polarized reflectance with increasing vegetation cover, where v is the Normalized Difference Vegetation Index (NDVI). The NDVI value v was obtained from the reflectance measurements concomitant with the polarization observations, B is a free parameter that should be chosen to fit the observed BPRF angular dependence.

Thus, in present algorithm the land surface reflectance properties are modeled using Eqs. (12) and (13) for simulating BRF and BPRF accordingly. However, since these formulations are semi-empirical and derived completely independently, one needs to exclude physically unrealistic combinations of BRF and BPRF. Therefore, in order to assure that the surface reflectance of polarized radiation in any geometry does not exceed the reflectance of total radiation, the reflectance matrix $\mathbf{R}(\mu_0; \mu_1; \varphi_0; \varphi_1; \lambda)$ of the land surface is represented a sum of two surface reflection phenomena:

$$\mathbf{R}(\mu_0;\mu_1;\varphi_0;\varphi_1;\lambda) = \mathbf{R}_{\text{diff}} + \mathbf{R}_{\text{spec}}, \tag{14a}$$

where the matrix for diffuse unpolarized reflectance $\mathbf{R}_{\text{diff}}$ is modeled using Eq. (12):

$$\mathbf{R}_{\text{diff}}(\mu_0;\mu_1;\varphi_0;\varphi_1;\lambda) = \rho_{\text{RPV}} \begin{pmatrix} 1 & 0 & 0 & 0 \\ 0 & 0 & 0 & 0 \\ 0 & 0 & 0 & 0 \\ 0 & 0 & 0 & 0 \end{pmatrix}, \tag{14b}$$

and the matrix for specular reflectance $\mathbf{R}_{\text{spec}}$ is modeled as matrix of Fresnel reflectance $\mathbf{F}(\alpha_i, n)$ scaled by $\rho_{\text{Maignan}}(\vartheta_1; \varphi_1; \vartheta_2; \varphi_2)$ empirical coeficient:

$$\mathbf{R}_{\text{spec}}(\vartheta_1; \varphi_1; \vartheta_2; \varphi_2; \lambda) = \rho_{\text{Maignan}} \mathbf{F}(\alpha_i, n), \tag{14c}$$

AMTD
3, 4967–5077, 2010

Statistically optimized inversion algorithm for enhanced retrieval

O. Dubovik et al.

where the Fresnel matrix $\mathbf{F}(\alpha_i, n)$ defined for Stokes parameters referred to directions parallel and perpendicular to the reflection plane can be written as (e.g. see Lenoble et al., 2007):

$$\mathbf{F}\,(\alpha_i, n) = \frac{1}{2}\begin{pmatrix} r_l^2 + r_r^2 & r_l^2 - r_r^2 & 0 & 0 \\ r_l^2 - r_r^2 & r_l^2 + r_r^2 & 0 & 0 \\ 0 & 0 & 2\,r_l\,r_r & 0 \\ 0 & 0 & 0 & 2\,r_l\,r_r \end{pmatrix}. \tag{15a}$$

The Fresnel matrix $\mathbf{F}(\alpha_i, n)$ depends on incident angle α_i and refractive index n. The coefficients r_r and r_l are defined as

$$r_r = \frac{\sin\,(\alpha_r - \alpha_i)}{\sin\,(\alpha_r + \alpha_i)} \text{ and } r_l = \frac{\tan\,(\alpha_r - \alpha_i)}{\tan\,(\alpha_r + \alpha_i)}, \tag{15b}$$

where the refraction angle α_r is related to α_i through the Snell-Descartes refraction law given as:

$$\sin\,(\alpha_i) = n \sin\,(\alpha_r). \tag{15c}$$

The straightforward analysis of above equations shows that the definition of $\mathbf{R}$ (μ_0; μ_1; φ_0; φ_1; λ) given by Eq. (14) secures the physically correct ratio between polarized and total radiation components ($R_{ij} \leq R_{11}$) for any combination of ρ_{RPV} and $\rho_{Maignan}$.

Thus, in the present algorithm, the BRF and BPRF properties are driven by four free spectral parameters of RPV model – $\rho_o\,(\lambda)$, $\kappa\,(\lambda)$, $\Theta\,(\lambda)$, $h_0\,(\lambda)$ – and one free (generally spectrally dependent) parameter $B\,(\lambda)$. All these parameters have been added into the retrieved vector of unknowns as shown in Table 1.

It should be noted, however, that the Rahman et al. (1993) and Maignan et al. (2009) formulations, chosen as primary models for BRF and BPRF in present algorithm, have limited accuracy (e.g. see Litvinov et al., 2010a,b). Therefore both the forward model and inversion module of present algorithm have an assumed option of changing the both or either BRF or BPRF models. For example, in the present algorithm version, the

AMTD
3, 4967–5077, 2010

BRF can be simulated using Ross-Li model and BPRF can be modeled using Nadal-Breon (1999) formulation. Nonetheless, the utilizations of these secondary BRF or BPRF models will not be discussed in details.

3.3 Full forward radiative model

Accounting for multiple scattering effects in the atmosphere is implemented by the successive order of scattering radiative transfer code (Lenoble et al., 2007) that was used in PARASOL operational retrievals (Deuze et al., 2001; Herman el al., 2005). The code provides full information about the atmospheric radiation field under the assumption of the plane parallel atmosphere. In order to reduce calculation time for inverting PARASOL observations, the V component in the Stokes vector has been neglected. Hansen (1971) has demonstrated that the radiation properties measured by passive remote sensing exhibit negligible circular polarization of the electromagnetic field. The developed version of successive order of scattering radiative transfer code allows calculations of atmospheric radiances for N_k several aerosol components. Each aerosol component can be described by defined vertical profile of spectral extinction $\tau_k(h,\ \lambda)$ and altitude independent phase matrix $\mathbf{P}_k(\Theta,\ \lambda)$ and single scattering albedo $\omega_0^k(\lambda)$.

In the present set up of the aerosol retrieval code the vertically invariant $\mathbf{P}_k(\Theta,\lambda)$ and $\omega_0^k(\lambda)$ are driven by (see Sect. 2.1 and Table 1): the shape of the size distribution $dV_k(r_i)/d\ln r$ giving the aerosol particle volume in the total atmospheric column per unit of the surface area (in the unites of $\mu m^3/\mu m^2$); the real $n_k(\lambda)$ and imaginary $k_k(\lambda)$ parts of the complex refractive index; the fraction of the spherical particles $C_{k,\mathrm{sph}}$. The spectral dependence of optical thickness $\tau_k(\lambda)/\tau_k(\lambda_i)$ is also vertically invariant and defined by these parameters, while the absolute value of $\tau_k(\lambda)$ additionally depends on the total volume of the aerosol in the atmospheric column: $C_{k,\mathrm{V}} = \sum_{i=1,\ \ldots,\ N_i} \left(\frac{dV_k(r)_i}{d\ln r}\right)$. In order to account for vertical variability of the aerosol extinction$\tau_k(h,\ \lambda)$, the additional characteristic $c_k(h)$ was added. The function $c_k(h)$ defines the vertical distribution of

AMTD
3, 4967–5077, 2010

Statistically optimized inversion algorithm for enhanced retrieval

O. Dubovik et al.

aerosol concentration and the optical thickness of k-th aerosol component in each of i-th atmospheric layer is defined as:

$$\Delta\,\tau_{i,k}\,(\lambda)\;=\;\int\limits_{h_{i+1}}^{h_i}\tau_k\,(\lambda)\,c_k\,(h)\,dh. \tag{16a}$$

The aerosol concentration profile $c_k(h)$ is assumed as a Gaussian function normalized to unity, i.e.:

$$c_k\,(h)\;\sim\;\exp\left(-\frac{\left(h\,-\,h_{k,0}\right)^2}{\sigma_k^2}\right)\;\text{and}\;\int\limits_{h_{\mathrm{BOT}}}^{h_{\mathrm{TOA}}}c_k\,(h)\,dh\;=\;1, \tag{16b}$$

where h_{BOA} – Bottom Of the Atmosphere (BOT) height and h_{TOA} – Top Of the Atmosphere (TOA) height. In the retrieval, the standard deviation characterizing the width of the aerosol layer is fixed to $\sigma_k = 0.75$ km. Therefore, only one parameter characterizing aerosol vertical distribution is included into the retrieval: $h_{k,0}$ – the mean altitude of the k-th aerosol component layer. The present version of the POLDER/PARASOL retrieval code is set to retrieve only one aerosol component, while the possibility of retrieving several aerosol components with different vertical distributions is also assumed (see Table 1).

In addition, in order to harmonize the radiative transfer code with the structure and needs of general inversion approach several modifications have been implemented. Specifically, the modifications were aimed to increase the speed of calculations by allowing admissible decrease of the accuracy of modeling. The three possible tradeoffs permitting reduction of computation time without any significant loss of retrieval accuracy were identified and implemented.

Discussion Paper | Discussion Paper | Discussion Paper | Discussion Paper |

AMTD

3, 4967–5077, 2010

Statistically optimized inversion algorithm for enhanced retrieval

O. Dubovik et al.

3.3.1 Adjustable number of the terms in the expansion of the phase matrix and in the quadrature of directional integration

The accuracy of radiative transfer calculations strongly depends on the number of terms M used in Fourier expansion of the phase matrix into Legendre polynomial and number of terms N used in Gaussian quadrature for zenithal integration. The values should satisfy to the inequality $4N-1>2M$ to retain conservation of the energy in the successive order of scattering integration. The values M and N should be sufficiently large to provide accurate calculation. However, the larger M and N the longer calculation time. At the same time, the high accuracy of the modeling is not always required during the retrieval. For example, studies by Dubovik and King (2000) showed that when observations of ground-based radiometers are inverted, the successful retrieval can be achieved using the approximate and quick calculations of the first derivatives. Correspondingly, the retrieval time can be significantly decreased because the calculations of the first derivatives is the most time consuming component of Newtonian's retrieval algorithms. Following this strategy, the operational retrieval of aerosol from AERONET data relies on analytical single scattering approximation in for calculations of derivates. The possibility of using this possible trade-off in POLDER retrieval algorithm was tested. It has been concluded that using single scattering approximation is not sufficient for conducting retrieval from satellite observations. Nonetheless, it has been found that the Jacobians estimated numerically as finite differences on basis of the full radiative transfer calculations implemented with significantly reduced values of M and N provide the fast and accurate retrievals. This approach is used in the present algorithm.

The utilization of linearized radiative transfer code (e.g. see Hasekamp and Landgraf, 2005a) that provides all derivatives in respect to aerosol and surface properties in a single run would be alternative and promising strategy of accelerating satellite observation inversion. This strategy was not used in present study because the linearization of radiative transfer code is rather complex effort that requires significant

AMTD
3, 4967–5077, 2010

time investments. The possibility of using this approach will be considered in the future studies. At the same time, retrieval algorithm relying on the numerical calculation of the first derivatives is probably more flexible in practical applications. Indeed, in present POLDER/PARASOL algorithm the set of the retrieved aerosol or/and surface parameters can flexibly changed with no modifications in the calculations of the first derivatives. If the derivatives are calculated analytically, achieving such flexibility could be more difficult.

3.3.2 Truncation of the phase matrix

The truncation of the phase function is an technique where the scattering effects from the sharply increasing forward peak of the phase function are calculated separately from those of the rest of the phase function, which permits the accurate but much faster modeling of diffuse radiation. For example the AERONET aerosol operational retrieval by Dubovik and King (2000) employs the discrete ordinate radiative transfer code by Nakajima and Tanaka (1988) that uses the efficient procedure of the phase function truncation and provides very fast and accurate calculation of down-welling diffuse radiation in moderately thick atmospheres. The detailed discussion of different methods of implementing the phase matrix truncation and their comparison is given in the recent paper by Rozanov and Lyapustin (2010).

Following the ideas of Nakajima and Tanaka (1988) the truncation of the phase matrix has been implemented in the successive order of scattering code as a part of present studies. In the developed version of the PARASOL algorithm the use of truncation is optional but recommended. The utilization of the phase matrix truncation allows for decreasing the number of terms M in the expansion of the truncated phase function and N in the Gaussian quadrature for azimuth integration. According to the results of the conducted tests accurate PARASOL retrieval can be achieved with the following recommended values: $M = 21$ and $N = 10$ – for calculating fit to PARASOL observations; $M = 15$ and $N = 7$ – for calculating Jacobian matrices.

AMTD
3, 4967–5077, 2010

3.3.3 Flexible angular representation in the phase function

The successive order of scattering radiative transfer code uses the phase function values at N_{ang} angles corresponding to the points of Gaussian quadrature. These values are provided to the radiative transfer code from the Dubovik et al. (2006) software generating aerosol single scattering properties. The software provides the phase function for the set of fixed scattering angles allowing sufficiently accurate modeling of angular variability of scattering. For example, in AERONET retrieval the phase function is calculated at 83 Gaussian points. At the same time, the speed of aerosol single scattering modeling depends on the number of the used scattering angles. In order to enhance the flexibility of the retrieval code the possibility of using the phase function at nearly arbitrary set of scattering angels has been implemented, with the values of the phase function at the required Gaussian points derived from the software data by convenient interpolation The results of the series of the numerical tests have shown that PARASOL/POLDER observations can be adequately modeled using set of $N_{ang} = 35$ selected scattering angles.

4 Numerical inversion

In a contrast to the majority of existing satellite retrieval algorithms, this effort is one of the first attempts to develop aerosol satellite retrieval as statistically optimized multivariable fitting. Such strategy does not rely on the pre-assumed classes of the potential solutions. Instead the solution is sought in a continuous space of solutions under statistically formulated criteria optimizing the error distribution of the retrieved parameters. The implementation of, at least, some elements of such strategy were pursued in the earlier developments of satellite retrieval algorithms. For example, the statistical optimization of the retrieval solutions was used for inversion of MISR observations by Martonchik et al. (1998), in the retrieval algorithms proposed by Chowdhary et al. (2002, 2005) and by Waquet et al. (2007, 2009a) for inverting anticipated

GLORY/APS observations and applied to RSP data, in the retrieval approach suggested by Hasekamp and Landgraf (2007) for applying to multiple-viewing-angle intensity and polarization measurements, in the retrieval algorithm developed by Govaerts et al. (2010) for processing SEVIRI/MSG observations.

The inversion methodology used here follows the developments by Dubovik and King (2000), Dubovik (2004), Dubovik et al. (2008). The methodology has several original (compare to standard inverse methods) features optimized for remote sensing applications. As shown in detailed description by Dubovik (2004), the methodology addresses such important aspects of inversion optimization as accounting for errors in the satellite observations, inversion of multi-source data with different levels of accuracy, accounting for a priori and ancillary information, estimating retrieval errors, clarifying potential of employing different mathematical inverse operations (e.g. comparing iterative versus matrix inversion methods), accelerating iterative convergence, etc. The concept uses the principles of statistical estimation and suggests a generalized multi-term *Least Square* type formulation that complementarily unites advantages of a variety of practical inversion approaches, such as *Phillips-Tikhonov-Twomey* constrained inversion (Phillips, 1962; Tikhonov, 1963; Twomey, 1963), *Kalman filter* (Kalman, 1961), *Newton-Gauss* and *Levenberg-Marquardt* iterations, etc. This approach provides significant transparency and flexibility in development of remote sensing algorithms for deriving such continuous characteristics as vertical profiles, size distributions, spectral dependencies of some parameters, etc. For example, compared to the popular "Optimal Estimation" equations (Rodgers, 2000), the multi-term Least Square type formulation allows harmonious utilization of not only a priori estimate term but instead, or in addition, using a priori terms limiting derivatives of the solution (see discussion by Dubovik, 2004 and Dubovik et al., 2008). This methodology has resulted from the multi-year efforts on developing inversion algorithms for retrieving comprehensive aerosol properties from AERONET ground-based observations.

Two alternative scenarios are proposed for inverting satellite observations: *single-pixel* retrieval and *multiple-pixel* retrieval. The *single-pixel* retrieval is a conventional

AMTD
3, 4967–5077, 2010

Title Page
Abstract | Introduction
Conclusions | References
Tables | Figures
◀| |▶
◀ ▶
Back | Close
Full Screen / Esc
Printer-friendly Version
Interactive Discussion

approach when observations of the satellite instrument over each single pixel (e.g. 6 × 6 km in case of POLDER/PARASOL) are inverted completely independently. The *multiple-pixel* retrieval is a newly suggested approach when the observations of the satellite instrument over a group of pixels are inverted simultaneously and extra a priori constraints on the inter-pixel variability of the retrieved parameters is applied. It is expected that applying such constrains will help to improve reliability of the retrieval.

4.1 Single-pixel retrieval

This part of the inverse procedure is adopted, with some modifications, from AERONET (Dubovik and King, 2000) inversion algorithm. There are two key aspects in the algorithm organization: the general *organization of observation fitting* and the a priori data representation.

4.1.1 Single-pixel observation fitting

Formally, the retrieval algorithm is designed as multi-term LSM (detailed discussion is given by Dubovik, 2004) that implements statistically optimum fitting of several sets of observations and a priori constraints under assumption of normally distributed uncertainties. It provides the solution of the following system of equations:

$$\left\{ O^* = \begin{array}{rcl} \boldsymbol{f}^* & = & \boldsymbol{f}(\boldsymbol{a}) + \Delta \boldsymbol{f} \\ (\Delta \boldsymbol{a})^* & = & \mathbf{S}\,\boldsymbol{a} + \Delta(\Delta\,\boldsymbol{a}) \\ \boldsymbol{a}^* & = & \boldsymbol{a} + \Delta\,\boldsymbol{a}^* \end{array} \right. . \tag{17}$$

Here, $\boldsymbol{f}^*$ is a vector of the PARASOL measurements, $\Delta \boldsymbol{f}$ is a vector of measurement uncertainties, $\boldsymbol{a}$ is a vector of unknowns. The second line in Eq. (17) represents the a priori smoothness assumptions used to constrain variability of size distribution and spectral dependencies of the real and imaginary parts of the refractive indices, as well as, the spectral dependencies of parameters of surface reflectance model. The matrix $\mathbf{S}$ includes the coefficients for calculating *m*-th differences (numeral equivalent

AMTD
3, 4967–5077, 2010

of the derivatives) of $dV(r_j)/d\ln r$, $n(\lambda_j)$, $k(\lambda_j)$, $\rho_o(\lambda_j)$, $\kappa(\lambda_j)$, $\Theta(\lambda_j)$; $\boldsymbol{O}^*$ – vector of zeros and $\Delta(\Delta \boldsymbol{a})$ – vector of the uncertainties characterizing the deviations of the differences from the zeros. Formally, this equation states that all these m-th differences are equal to zeros $\boldsymbol{O}^*$ within the uncertainties $\Delta(\Delta \boldsymbol{a})$. The third line in Eq. (17) includes the vector of a priori estimates $\boldsymbol{a}^*$ and $\Delta \boldsymbol{a}^*$ is vector of the uncertainties in a priori estimates.

In order to account for the non-negative character of the observed radiances and retrieved aerosol – $dV(r_j)/d\ln r$, $n(\lambda_j)$, $k(\lambda_j)$ – and surface reflectance – $\rho_o(\lambda_j)$ – parameters, the assumption of log-normal error distribution was used. The noise distribution is apparently the most appropriate for the positively defined values. The log-normal noise distribution implies that the logarithms of the observed positively defined values are normally distributed. Thus, for convenience of formulating the statistically optimized solution of Eq. (17) the logarithmic transformation is used for both measured f_j and retrieved a_i parameters (see detailed discussions on validity of applying this transformation in the publications by Dubovik and King, 2000; Dubovik, 2004). Correspondingly, the errors $\Delta \boldsymbol{f}$, $\Delta(\Delta \boldsymbol{a})$, and $\Delta \boldsymbol{a}^*$ are assumed normally distributed. Table 2 shows the exact definitions of each element of the vectors $\boldsymbol{f}^*$ and $\boldsymbol{a}$. In addition, Table 2 shows the variability ranges allowed for each retrieved parameter.

The statistically optimized solution of Eq. (17) defined on the base of Maximum Likelihood Method corresponds to the minimum of the following quadratic form:

$$\Psi\left(\boldsymbol{a}^p\right) = \Psi_f\left(\boldsymbol{a}^p\right) + \Psi_\Delta\left(\boldsymbol{a}^p\right) + \Psi_a\left(\boldsymbol{a}^p\right)$$
$$= \frac{1}{2}\left(\left(\Delta \boldsymbol{f}^p\right)^T \left(\mathbf{W}_f\right)^{-1} \Delta \boldsymbol{f}^p + \gamma_\Delta \boldsymbol{a}^p \boldsymbol{\Omega} \boldsymbol{a}^p + \gamma_a \left(\boldsymbol{a}^p - \boldsymbol{a}^*\right)^T \mathbf{W}_a^{-1} \left(\boldsymbol{a}^p - \boldsymbol{a}^*\right)\right), \tag{18a}$$

In generally non-linear case the minimum can be obtained by the following iterative procedure:

$$\boldsymbol{a}^{p+1} = \boldsymbol{a}^p - t_p \Delta \boldsymbol{a}^p, \tag{18b}$$

where $\Delta \boldsymbol{a}^p$ is a solution of the p-th so-called, in statistical estimation formalism, *Normal System*

$$\mathbf{A}_p \Delta \boldsymbol{a}^p = \nabla \Psi\left(\boldsymbol{a}^p\right). \tag{18c}$$

The matrix in the left side of Eq. (18c) is also known as *Fisher Matrix* $\mathbf{A}_p$ and the right side of the Eq. (18c) represents the gradient $\nabla\Psi(\boldsymbol{a}^p)$ of quadratic form $\Psi(\boldsymbol{a}^p)$ in vicinity of $\boldsymbol{a}^p$:

$$\mathbf{A}_p = \mathbf{K}_p^T \mathbf{W}_f^{-1} \mathbf{K}_p + \gamma_\Delta \boldsymbol{\Omega} + \gamma_a \mathbf{W}_a^{-1}, \tag{18d}$$

$$\nabla \Psi \left(\boldsymbol{a}^p\right) = \mathbf{K}_p^T \mathbf{W}^{-1} \Delta \boldsymbol{f}^p + \gamma_\Delta \boldsymbol{\Omega}\, \boldsymbol{a}^p + \gamma_a \mathbf{W}_a^{-1} \left(\boldsymbol{a}^p - \boldsymbol{a}^*\right), \tag{18e}$$

where $\Delta \boldsymbol{f}^p = \boldsymbol{f}(\boldsymbol{a}^p) - \boldsymbol{f}^*$, $\mathbf{K}_p$ – Jacobi matrix of the first derivatives $\frac{\partial f_j(\boldsymbol{a}^p)}{\partial a_i}$. It should be noted that *Fisher Matrix* $\mathbf{A}_p$ can be considered as divergence of the quadratic form (i.e. second derivatives): $\mathbf{A}_p = \mathrm{div}(\Psi(\boldsymbol{a}^p)) = \nabla \times \nabla\Psi(\boldsymbol{a}^p)$. Correspondingly, Eq. (18a) can be also written as follows:

$$\left(\nabla \times \nabla \Psi \left(\boldsymbol{a}^p\right)\right) \Delta \boldsymbol{a}^p = \nabla \Psi \left(\boldsymbol{a}^p\right). \tag{18f}$$

In present inversion strategy all equations are expressed via $\mathbf{W}$ – weighting matrices that defined by dividing the correspondent covariance matrix $\mathbf{C}$ by its first diagonal element ε^2, i.e. $\mathbf{W} = (1/\varepsilon^2)\mathbf{C}$. This formal transformation of the inversion equations allows rather transparent interpretation of Lagrange multipliers γ – parameters determining the contributions of a priori terms into solution. Following the concept proposed by Dubovik and King (2000) the Lagrange multipliers γ_a and γ_Δ are defined as:

$$\gamma_\Delta = \varepsilon_f^2/\varepsilon_\Delta^2 \text{ and } \gamma_a = \varepsilon_f^2/\varepsilon_a^2, \tag{19a}$$

where ε_f^2, ε_Δ^2 and ε_a^2 are the first diagonal elements of correspondent covariance matrices $\mathbf{C}_f$, $\mathbf{C}_\Delta$ and $\mathbf{C}_a$. Note, that if one can assume a simplified situation when the POLDER observations f*, a priori estimates of differences $(\Delta \boldsymbol{a})^*$ and a priori estimates of parameters $\boldsymbol{a}^*$ are independent and have the same accuracy, i.e. $\mathbf{C}_f = \varepsilon_f^2 \mathbf{I}_{(N_f \times N_f)}$, $\mathbf{C}_\Delta = \varepsilon_\Delta^2 \mathbf{I}_{(N_\Delta \times N_\Delta)}$ and $\mathbf{C}_a = \varepsilon_a^2 \mathbf{I}_{(N_a \times N_a)}$, then correspondent weighting matrices are simply equal to the unity matrices: $\mathbf{W}_f = \mathbf{I}_{(N_f \times N_f)}$, $\mathbf{W}_\Delta = \mathbf{I}_{(N_\Delta \times N_\Delta)}$ and $\mathbf{W}_a = \mathbf{I}_{(N_a \times N_a)}$.

AMTD
3, 4967–5077, 2010

In addition, as discussed by Dubovik (2004), straightforward increasing N_f by adding redundant very similar observations is not necessarily beneficial for the retrieval. For example, from practical viewpoint, adding many observations with identical or nearly identical observation conditions does not bring new information and does not improve the accuracy of the solution. However, formally even such addition of observations artificially increases the impact of the measurement term on the solution compare to a priori second and thirds term in Eq. (18). Therefore, the Lagrange multipliers γ are scaled as:

$$\gamma_\Delta = \frac{N_f\ \varepsilon_f^2}{N_\Delta\ \varepsilon_\Delta^2} \text{ and } \gamma_a = \frac{N_f\ \varepsilon_f^2}{N_a\ \varepsilon_a^2}. \tag{19b}$$

As suggested by Dubovik (2004) such scaling reflects the inevitable decrease of accuracy of single observation ε_f^2 if the number of observation N_f increases excessively. The above equation is written under an assumption that increasing the number of measurements in the coordinated set of remote sensing observations inevitably results to the decrease of the accuracy of each single measurement in this observation set. For example, if a satellite sensor takes one single observation, the expected variance of measurement error is $\varepsilon_{f,N}^2$. If the same sensor makes N_f space- and/or time-coordinated observations the variance of the error in each single observation increases by the factor N_f, i.e. $\varepsilon_{f,N}^2 \sim N_f \varepsilon_{f,1}^2$. This increase can be explained by the fact that the consistency of the N_f coordinated observations should be assured by controlling N_f relations between the N_f observations. The control of each of those relationships introduces a random error $\varepsilon_{f,N}^2$, correspondingly the error variance of a single measurement in N_f dimensional observation increases in N_f times.

The coefficient $t_p \le 1$ in Eq. (17a) is adjusted to provide monotonic decrease of $\Psi(\boldsymbol{a}^p)$, i.e.

$$\Psi\left(\boldsymbol{a}^{p+1}\right) < \Psi\left(\boldsymbol{a}^p\right). \tag{20a}$$

If all assumptions are correct the minimum value of above quadratic form can be theoretically estimated as follows:

$$\Psi\left(\boldsymbol{a}\right) \approx \left(N_{\mathrm{f}} + N_{\Delta} + N_{\mathrm{a}*} - N_{\mathrm{a}}\right) \varepsilon_{\mathrm{f}}^{2} \tag{20b}$$

Note that minimum value of $\Psi(\boldsymbol{a}^{\mathrm{p}})$ relates with $\varepsilon_{\mathrm{f}}^{2}$ because earlier the weighting matrices were used instead of using directly the covariance matrices. Once the value of measurement error is known $\varepsilon_{\mathrm{f}}^{2}$, Eq. (20b) can be used to verify the consistency of the retrieval. Specifically, the inability to achieve the above minimum can indicate the presence of unidentified biases or inadequacy in the assumptions made.

It should be noted that the control of $\Psi_{\mathrm{f}}(\boldsymbol{a}^{\mathrm{p}})$ (the first term of quadratic form in Eq. 18a) – "measurement residual" is very useful too for diagnostics of the retrieval dynamics. Specifically, the final value of "measurement residual" $\Psi_{\mathrm{f}}(\boldsymbol{a}^{\mathrm{p}})$ should be close to the level of the expected measurement noise. Indeed, if the algorithm has found the right solution the value of the total residual $\Psi(\boldsymbol{a}^{\mathrm{p}})$ should be rather small and determined mainly by the random errors of observations. The values of a priori term should not be significant, because generally the weights of a priori terms are minor compare the weight of the observation terms. However, at early iterations when the solution approximation is very far from the solution, the "measurement residual" $\Psi_{\mathrm{f}}(\boldsymbol{a}^{\mathrm{p}})$ is dominated by linearization errors and has the value much higher than the level of the expected measurement noise. Therefore, since accuracy of a priori data is independent of the iteration, the weight of the a priori term should be increased. Correspondingly, this additional enhancement of the a priori data impact on the solution improves the convergence of non-linear fitting. For example, in developed POLDER/PARASOL algorithm, following Dubovik and King (2000) and Dubovik (2004) the strength of a priori constraints is adjusted dynamically as a function of the measurement residual $\Psi_{\mathrm{f}}(\boldsymbol{a})$:

$$\varepsilon_{\mathrm{f}}^{2}\left(\boldsymbol{a}^{\mathrm{p}}\right) \approx \frac{\Psi_{\mathrm{f}}\left(\boldsymbol{a}^{\mathrm{p}}\right)}{\left(N_{\mathrm{f}} - N_{\mathrm{a}}\right)}, \tag{20c}$$

where $\Psi_f(\boldsymbol{a}^p)$ reflects the accuracy of POLDER observation fit at p-th iteration and provides an indication of how the iterations converge to the solution. For example, at the last iteration, when the solution estimate $\boldsymbol{a}^{p_{last}}$ is expected to be in a small vicinity of the actual solution the value of the residual $\Psi_f(\boldsymbol{a})$ of the measurement fit can be estimated as:

$$\Psi_f\left(\boldsymbol{a}^{p_{last}}\right) \approx (N_f - N_a)\,\varepsilon_f^2. \tag{20d}$$

Using estimate $\varepsilon_f^2(\boldsymbol{a}^p)$ by Eq. (20c) adjusts the values Lagrange multipliers γ_Δ and γ_a in Eq. (18) and enhances the contribution of a priori constraints at the earlier iterations. As suggested by Dubovik (2004) this dynamic determination of a priori constraints improves convergence of non-linear iterations analogously to Levenberg-Marquardt formulations. At the same time, in difference with original Levenberg-Marquardt method, the idea of enhancing constraints on the solutions at earlier iterations in the formulations by Dubovik (2004) is included harmoniously within the framework of united statistical estimation approach. For example, if no smoothness constraints are used (i.e. the smoothness terms in the right sides of Eqs. (17) and (18) are eliminated) and no a priori estimates $\boldsymbol{a}^*$ are available, then one can assume $\boldsymbol{a}^* = \boldsymbol{a}^p$, Eq. (18) become equivalent to Levenberg-Marquardt formulations (see details in Dubovik, 2004).

Thus, the inversion procedure described above is driven by the limited set of the input characteristics that includes the weighting matrices $\mathbf{W}_{...}$ and corresponding variances $\boldsymbol{\varepsilon}_{...}$. The vector of POLDER/PARASOL measurements includes 2 components:

$$\boldsymbol{f}^* = \begin{pmatrix} \boldsymbol{f}_I^* \\ \boldsymbol{f}_P^* \end{pmatrix}, \tag{21a}$$

where index "I" denotes total reflectance observations and index "P" denotes the observations of the degree of linear polarization (see Table 2). Since the total radiance and degree of linear polarization are measured with different accuracy, the covariance matrix assumed for logarithms of measurements $\boldsymbol{f}^*$: has array structure:

$$\mathbf{C}_f = \begin{pmatrix} \mathbf{C}_I & \mathbf{0} \\ \mathbf{0} & \mathbf{C}_P \end{pmatrix} = \begin{pmatrix} \varepsilon_I^2 \, \mathbf{I}_I & \mathbf{0} \\ \mathbf{0} & \varepsilon_P^2 \, \mathbf{I}_P \end{pmatrix}, \tag{21b}$$

Correspondingly, the weighting matrix $\mathbf{W}_f$ is defined as:

$$\mathbf{W}_f = \begin{pmatrix} \mathbf{I}_I & \mathbf{0} \\ \mathbf{0} & \gamma_P \, \mathbf{I}_P \end{pmatrix} \tag{21c}$$

where $\mathbf{I}_{\ldots}$ denote the unity matrices of correspondent dimension and γ_P is a ratio of the total and polarized reflectance variances:

$$\gamma_p = \varepsilon_p^2 / \varepsilon_I^2 \; \varepsilon_p. \tag{21d}$$

The variance of the errors in measurements of total reflectance is expected at the level of 2% relative the magnitude of observed radiance I, i.e. $\varepsilon_I = \Delta(\ln I) \approx \frac{\Delta I}{I} = 0.02$. The variance of the errors in measurements of the degree of linear polarization is expected at the absolute level of 1%, i.e. $\Delta P = 0.01$ and $\varepsilon_p = \Delta(\ln P) \approx \frac{\Delta P}{P} = \frac{0.01}{P}$. Equation (23a) assumes the simplest structure of the covariance matrix when intensity and polarization observations are equally accurate for all spectral channels and angles of observations. If more detailed information about covariance matrix is available it can be trivially integrated into Eq. (23).

In contrast to the numerous remote sensing algorithm relying on a priori estimates as suggested by Rodgers (2000), the a priori estimates $\boldsymbol{a}^*$ were not used at all, i.e. $\varepsilon_a^2 = \infty$ (although in practical application to the using of, at least for land surface parameters, the climatological values with adequately estimated variances) is rather reasonable. Thus, in contrast to the methodology by Rodgers (2000), the retrieval was constrained here using exclusively the a priori smoothness constraints as discussed in the follow on Section.

4.1.2 A priori smoothness constraints in single pixel fitting

The vector $\boldsymbol{a}$ includes several components:

$$\boldsymbol{a} = \left(\boldsymbol{a}_{\mathrm{v}}\ \boldsymbol{a}_{n}\ \boldsymbol{a}_{\mathrm{k}}\ a_{\mathrm{sph}}\ a_{\mathrm{Vc}}\ a_{\mathrm{h}}\ \boldsymbol{a}_{\mathrm{brf},1}\ \boldsymbol{a}_{\mathrm{brf},2}\ \boldsymbol{a}_{\mathrm{brf},3}\ \boldsymbol{a}_{\mathrm{bprf}}\right)^{T}, \tag{22}$$

where $\boldsymbol{a}_{\mathrm{v}}$, $\boldsymbol{a}_{n}$, $\boldsymbol{a}_{\mathrm{k}}$, a_{sph} denote the components of the vector $\boldsymbol{a}$ corresponding to the $dV(r_i)/d\ln r$, $n(\lambda_i)$, $k(\lambda_i)$ and C, a_{h} is equal to the logarithm of mean altitude of the aerosol layer h_{a}. The element a_{Vc} is the logarithm of total volume concentration, while $\boldsymbol{a}_{\mathrm{v}}$ includes logarithms of values $dV(r)/d\ln r$ normalized by total volume concentration. This modification (compare to AERONET algorithm) allows decoupling the retrieval of the total amount of aerosol from the shape of the size distribution. This decoupling of the size distribution parameter is essential for satellite imager algorithm, since it allows applying different constraints on the shape of size distribution and aerosol loading. The three components $\boldsymbol{a}_{\mathrm{brf},1}$, $\boldsymbol{a}_{\mathrm{brf},2}$ and $\boldsymbol{a}_{\mathrm{brf},3}$ that are related to the logarithms of spectrally dependent parameters $\rho_{\mathrm{o}}(\lambda)$, $k(\lambda)$ and $\theta(\lambda)$ of employed RPV model. Note, that here "hot spot" parameter $h_0(\lambda)$ that present in Eq. (12) is not included in the vector $\boldsymbol{a}$, because it is not retrieved near-backscattering direction not observed (it is significant only in narrow range of scattering angles around backscattering direction). At the same time, $h_0(\lambda)$ is retrieved if "hot spot" is observed. In such situation it is included in the retrieval similarly to other BRF parameters – $\rho_{\mathrm{o}}(\lambda)$, $k(\lambda)$ and $\theta(\lambda)$. The vector $\boldsymbol{a}_{\mathrm{bprf}}$ includes the logarithms of the spectrally dependent free parameter $B(\lambda)$ of the employed Maignon et al. (2009) model. The detail description of each element of the vector $\boldsymbol{a}$ is given in the Table 2.

The a priori smoothness constraints are applied in the PARASOL algorithm on several different components of the vector $\boldsymbol{a}$ differently. For example, for $\boldsymbol{a}$ given by Eq. (17), the matrix $\mathbf{S}$ has the following array structure:

AMTD
3, 4967–5077, 2010

$$
\mathbf{S}\boldsymbol{a} = \begin{pmatrix}
\mathbf{S}_v & \mathbf{0} & \mathbf{0} & \mathbf{0} & \mathbf{0} & \mathbf{0} & \mathbf{0} & \mathbf{0} & \mathbf{0} & \mathbf{0} \\
\mathbf{0} & \mathbf{S}_n & \mathbf{0} & \mathbf{0} & \mathbf{0} & \mathbf{0} & \mathbf{0} & \mathbf{0} & \mathbf{0} & \mathbf{0} \\
\mathbf{0} & \mathbf{0} & \mathbf{S}_k & \mathbf{0} & \mathbf{0} & \mathbf{0} & \mathbf{0} & \mathbf{0} & \mathbf{0} & \mathbf{0} \\
0 & 0 & 0 & 0 & 0 & 0 & 0 & 0 & 0 & 0 \\
0 & 0 & 0 & 0 & 0 & 0 & 0 & 0 & 0 & 0 \\
0 & 0 & 0 & 0 & 0 & 0 & 0 & 0 & 0 & 0 \\
\mathbf{0} & \mathbf{0} & \mathbf{0} & \mathbf{0} & \mathbf{0} & \mathbf{0} & \mathbf{S}_{\mathrm{brf},1} & \mathbf{0} & \mathbf{0} & \mathbf{0} \\
\mathbf{0} & \mathbf{0} & \mathbf{0} & \mathbf{0} & \mathbf{0} & \mathbf{0} & \mathbf{0} & \mathbf{S}_{\mathrm{brf},2} & \mathbf{0} & \mathbf{0} \\
\mathbf{0} & \mathbf{0} & \mathbf{0} & \mathbf{0} & \mathbf{0} & \mathbf{0} & \mathbf{0} & \mathbf{0} & \mathbf{S}_{\mathrm{brf},3} & \mathbf{0} \\
\mathbf{0} & \mathbf{0} & \mathbf{0} & \mathbf{0} & \mathbf{0} & \mathbf{0} & \mathbf{0} & \mathbf{0} & \mathbf{0} & \mathbf{S}_{\mathrm{bprf}}
\end{pmatrix}
\begin{pmatrix}
\boldsymbol{a}_v \\ \boldsymbol{a}_n \\ \boldsymbol{a}_k \\ a_{\mathrm{sph}} \\ a_{\mathrm{Vc}} \\ a_{\mathrm{h}} \\ \boldsymbol{a}_{\mathrm{brf},1} \\ \boldsymbol{a}_{\mathrm{brf},2} \\ \boldsymbol{a}_{\mathrm{brf},3} \\ \boldsymbol{a}_{\mathrm{bprf}}
\end{pmatrix}, \tag{23}
$$

where the correspondent matrices $\mathbf{S}_{\dots}$ have different dimensions and represent differences of different order – 3 for size distribution, 1 for $n(\lambda)$, 2 for $k(\lambda)$, 2 for $\rho_o(\lambda)$, 1 for $\kappa(\lambda)$, $\theta(\lambda)$ and $B(\lambda)$. The lines in Eq. (23) corresponding to a_{h}, a_{Vc} and a_{sph} contain only zeros because no smoothness constraint can be applied.

The utilization of the smoothness constraints was originated by the papers by Phillips (1962), Tikhonov (1963) and Twomey (1963). In these studies the solution $\hat{\boldsymbol{a}}$ was constrained by minimizing m-th differences Δ^m of the vector $\hat{\boldsymbol{a}}$ components:

$$
\begin{aligned}
\Delta^1 &= \hat{\boldsymbol{a}}_{i+1} - \hat{\boldsymbol{a}}_i, \quad (m = 1), \\
\Delta^2 &= \hat{\boldsymbol{a}}_{i+2} - 2\,\hat{\boldsymbol{a}}_{i+1} + \hat{\boldsymbol{a}} - i \quad (m = 2), \\
\Delta^3 &= \hat{\boldsymbol{a}}_{i+3} - 3\,\hat{\boldsymbol{a}}_{i+2} + 3\,\hat{\boldsymbol{a}}_{i+1} = \hat{\boldsymbol{a}}_i, \quad (m = 3).
\end{aligned} \tag{24}
$$

The minimization of the differences is usually considered to be an implicit constraint on derivatives. The correspondent smoothness matrix $\boldsymbol{\Omega}$ in Eq. (18) are defined as:

$$
\boldsymbol{\Omega} = (\mathbf{S}_m)^T\,(\mathbf{S}_m), \tag{25a}
$$

Discussion Paper | Discussion Paper | Discussion Paper | Discussion Paper |

AMTD

3, 4967–5077, 2010

Statistically optimized inversion algorithm for enhanced retrieval

O. Dubovik et al.

where $\mathbf{S}_m$ is matrix of m-th differences (i.e. $\mathbf{\Delta}^m = \mathbf{S}_m \hat{\boldsymbol{a}}$). For example, $\mathbf{S}_2$ ($m = 2$) is:

$$\mathbf{S}_2 = \begin{pmatrix} 1 & -2 & 1 & 0 \ldots & & & \\ 0 & 1 & -2 & 1 & 0 \ldots & & \\ 0 & 0 & 1 & -2 & 1 & 0 \ldots & \\ \ldots & \ldots & \ldots & \ldots & \ldots & \ldots & \ldots \\ \ldots & \ldots & \ldots & & 0 & 1 & -2 \; 1 \end{pmatrix}. \tag{25b}$$

The present development follows the concept of Dubovik and King (2000) and Dubovik (2004) that considers smoothness constraints explicitly as a priori estimates of the derivatives of the retrieved characteristic $y(x_i)$.

The values of m-th derivatives g_m of the function $y(x)$ characterize the degree of its non-linearity and, therefore, can be used as a measure of $y(x)$ smoothness. For example, smooth functions $y(x)$, such as, a constant, straight line, parabola, etc can be identified by m-th derivatives as follows:

$$\begin{aligned} g_1(x) &= dy(x)/dx = 0 \Rightarrow y_1(x) = C; \\ g_2(x) &= d^2y(x)/dx^2 = 0 \Rightarrow y_2(x) = Bx + C; \\ g_3(x) &= d^3y(x)/dx^3 = 0 \Rightarrow y_3(x) = Ax^2 + Bx + C \end{aligned} . \tag{26}$$

These derivatives g_m can be approximated by differences between values of the function $a_i = y(x_i)$ in N_a discrete points x_i as:

$$\begin{aligned} &\frac{dy(x_i)}{dx} \approx \frac{\Delta^1 y(x_i)}{\Delta_1 x_i} = \frac{y(x_i + \Delta x_i) - y(x_i)}{\Delta_1 x_i} = \frac{y(x_{i+1}) - y(x_i)}{\Delta_1 x_i}; \\ &\frac{d^2 y(x_{i''})}{dx^2} \approx \frac{\Delta^2 y(x_i)}{\Delta_2(x_i)} = \frac{\Delta^1 y(x_{i+1})/\Delta_1(x_{i+1}) - \Delta^1 y(x_i)/\Delta_1(x_i)}{(\Delta_1 x_i + \Delta_1 x_{i+1})/2} = \ldots; \\ &\frac{d^3 y(x_{i'''})}{dz^3} \approx \frac{\Delta^3 y(x_i)}{\Delta_3(x_i)} = \frac{\Delta^2 y(x_{i+1})/\Delta_2(x_{i+1}) - \Delta^2 y(x_i)/\Delta_2(x_i)}{(\Delta_2(x_i) + \Delta_2(x_{i+1}))/2} = \ldots; \end{aligned} \tag{27}$$

AMTD
3, 4967–5077, 2010

where

$$\Delta_1(x_i) = x_{i+1} - x_i;\ \Delta_2(x_i) = (\Delta_1(x_i) + \Delta_1(x_{i+1}))/2; \Delta_3(x_i) = (\Delta_2(x_i) + \Delta_1(x_{i+1}))/2;$$

$$x_{i'} = x_i + \Delta_1(x_i)/2; x_{i''} = x_i + (\Delta_1(x_i) + \Delta_2\ (x_i))/2; x_{i'''} = x_i + (\Delta_1(x_i) + \Delta_2\ (x_i) + \Delta_3\ (x_i))/2.$$

In retrievals of the function $y(x_i)$ in N_a discrete points x_i, the expectations of limited derivatives of $y(x)$ can be explicitly employed as smoothness constrains. Namely, if the retrieved function is expected to be close to a constant, straight line, parabola, etc one can use zero m-th derivatives (as follows from Eq. 26) as a priori estimates: $\boldsymbol{g}^*_m = \mathbf{0}$.

In difference with Eq. (24), Eq. (26) allow applying smoothness constraints in more general situations when $\Delta_1(x_i) \neq$const. For example, in present algorithm there is a number of spectral parameters that are functions of λ and the algorithm deals with their values defined for each spectral channel λ_i. Obviously the $(\lambda_{i+1} - \lambda_i) \neq$const and using standard definition of differences by Eq. (26) for smoothing spectral parameters – e.g. $n(\lambda)$, $\rho_o(\lambda)$ etc – is not completely correct. Applying the limitations on the derivatives defined by Eq. (27) is more rigorous. Although using Eq. (27) leads to loose of transparency in definitions of matrices $\mathbf{S}_k$ (they do not have such simple definition as shown in Eq. 25), generating those matrices on algorithmic level is rather straightforward.

In order to estimate correctly the strength of a priori constraints Dubovik and King (2000) and Dubovik (2004) suggested using the analogy of $\Psi_\Delta(\boldsymbol{a})$ to the integral norm of the derivatives. Namely, the quadratic term $\Psi_\Delta(\boldsymbol{a})$ can be considered as an estimate of the norm of the m-th derivatives obtained using the values of $y(x)$ at N_a discrete points x_i:

$$\int \left(\frac{d^m\ y\ (x)}{d^m\ x} \right)^2 dx \approx \sum_{i=m+1}^{N_a} \left(\frac{\Delta^m\ y\ (x_i)}{\Delta_m\ (x_i)} \right)^2 \Delta_m\ (x_i) = \boldsymbol{a}^T\ \mathbf{S}_m^T\ \mathbf{S}_m\ \boldsymbol{a} \approx \Psi_\Delta\ (\boldsymbol{a}). \quad (28)$$

Correspondently, the uncertainty of a priori smoothness constraits on each retrieved characteristic can be defined as follows:

$$\varepsilon^2_{\Delta,i} \approx \int_{x_{\min}}^{x_{\max}} \left(\frac{d^m\, y_i\,(x)}{d^m x} \right)^2 dx, \tag{29}$$

where $y_i(x)$ denotes the function $dV(r)/d\ln r$, $n(\lambda)$, $k(\lambda)$, $\rho_o(\lambda)$, $\kappa(\lambda)$, $\theta(\lambda)$ and $B(\lambda)$ for $i = 1, 2, \ldots, 7$ correspondingly; $\varepsilon_\Delta = \varepsilon_{\Delta,1}$. The values of $\varepsilon^2_{\Delta,i}$ driving the strength of each a priori constraint were calculated using most unsmooth (variable) examples of correspondent physical functions, i.e. most unsmooth size distributions, spectral dependencies of refractive indices and BRF parameters. The detailed description of this concept for setting smoothness constraints is given in the papers by Dubovik and King (2000) and Dubovik (2004).

Thus, the smoothness matrix in Eq. (18) is defined as follows:

$$\boldsymbol{\gamma}_\Delta\, \boldsymbol{\Omega} = \begin{pmatrix} \boldsymbol{\gamma}_{\Delta,1}\,\boldsymbol{\Omega}_1 & \mathbf{0} & \mathbf{0} & \mathbf{0} & \mathbf{0} & \mathbf{0} & \mathbf{0} & \mathbf{0} & \mathbf{0} & \mathbf{0} \\ \mathbf{0} & \boldsymbol{\gamma}_{\Delta,2}\,\boldsymbol{\Omega}_2 & \mathbf{0} & \mathbf{0} & \mathbf{0} & \mathbf{0} & \mathbf{0} & \mathbf{0} & \mathbf{0} & \mathbf{0} \\ \mathbf{0} & \mathbf{0} & \boldsymbol{\gamma}_{\Delta,3}\,\boldsymbol{\Omega}_3 & \mathbf{0} & \mathbf{0} & \mathbf{0} & \mathbf{0} & \mathbf{0} & \mathbf{0} & \mathbf{0} \\ 0 & 0 & 0 & 0 & 0 & 0 & 0 & 0 & 0 & 0 \\ 0 & 0 & 0 & 0 & 0 & 0 & 0 & 0 & 0 & 0 \\ 0 & 0 & 0 & 0 & 0 & 0 & 0 & 0 & 0 & 0 \\ \mathbf{0} & \mathbf{0} & \mathbf{0} & \mathbf{0} & \mathbf{0} & \mathbf{0} & \boldsymbol{\gamma}_{\Delta,4}\,\boldsymbol{\Omega}_4 & \mathbf{0} & \mathbf{0} & \mathbf{0} \\ \mathbf{0} & \mathbf{0} & \mathbf{0} & \mathbf{0} & \mathbf{0} & \mathbf{0} & \mathbf{0} & \boldsymbol{\gamma}_{\Delta,5}\,\boldsymbol{\Omega}_5 & \mathbf{0} & \mathbf{0} \\ \mathbf{0} & \mathbf{0} & \mathbf{0} & \mathbf{0} & \mathbf{0} & \mathbf{0} & \mathbf{0} & \mathbf{0} & \boldsymbol{\gamma}_{\Delta,6}\,\boldsymbol{\Omega}_6 & \mathbf{0} \\ \mathbf{0} & \mathbf{0} & \mathbf{0} & \mathbf{0} & \mathbf{0} & \mathbf{0} & \mathbf{0} & \mathbf{0} & \mathbf{0} & \boldsymbol{\gamma}_{\Delta,7}\,\boldsymbol{\Omega}_7 \end{pmatrix}, \tag{30}$$

where $\boldsymbol{\Omega}_i = \mathbf{S}_i^T \mathbf{S}_i$ and the difference matrices $\mathbf{S}_i$ ($i = 1, \ldots, 7$) to $\mathbf{S}_v$, $\mathbf{S}_n$, $\mathbf{S}_k$, $\mathbf{S}_{\mathrm{brf},1}$, $\mathbf{S}_{\mathrm{brf},2}$, $\mathbf{S}_{\mathrm{brf},3}$, $\mathbf{S}_{\mathrm{brpf}}$. It should be noted that for making formulations more transparent only one coefficient $\boldsymbol{\gamma}_\Delta$ was shown in Eq. (18). However, the actual algorithm uses 6 (or even 7 if $h_0(\lambda_i)$ is retrieved) scaling coefficients $\boldsymbol{\gamma}_{\Delta,i}$:

$$\boldsymbol{\gamma}_{\Delta,i} = \varepsilon_f^2 / \varepsilon^2_{\Delta,j} \tag{31}$$

AMTD

3, 4967–5077, 2010

These coefficients were estimated using Eq. (29). Table 3 shows the orders of the differences used for smoothness constrains and the correspondent values of Lagrange multipliers $\gamma_{\Delta,i}$. The general structure of the numerical inversion data flow implemented for the retrieval of aerosol over single pixel is summarized in Fig. 4.

4.2 Multiple-pixel retrieval

In a contrast with the most of satellite retrievals, the algorithm developed here does implement the measurement fitting for each single pixel independently. Instead, the fitting is implemented for a group of pixels and is constrained by the extra a priori limitations on inter-pixel variability of aerosol and/or surface reflectance properties. This approach for improving the stability of satellite data inversions, because the information content of the reflected radiation from single pixel is sometime insufficient for unique retrieval of all retrieved parameters. For example, deriving aerosol properties over bright lands is known as an extremely difficult task. On the other hand, if the surface reflectance and aerosol properties happen to be the same for a certain time period or over some area, one can trivially achieve higher redundancy in the retrieval by applying single pixel algorithm to the observations collected from such multiple pixels. This fundamental tendency can be formulated as a priori known statistical limitation that can serve as an extra constraint making multi-pixel retrieval more robust and reliable. Dubovik et al. (2008) discussed using this concept in a frame of statistical estimation formalism for improving global aerosol inverse modeling retrievals.

4.2.1 Multiple-pixel observation fitting

For making the equations more compact the equation system of Eq. (17) defined for i-th single pixel can be denoted as follows:

$$\begin{cases} \boldsymbol{f}_i^* = \boldsymbol{f}_i\,(\boldsymbol{a}) + \Delta\,\boldsymbol{f}_i \\ \boldsymbol{O}_i^* = \mathbf{S}_i\,\boldsymbol{a}_i + \Delta\,(\Delta\,\boldsymbol{a}_i) \\ \boldsymbol{a}_i^* = \boldsymbol{a}_i + \Delta\,\boldsymbol{a}_i^* \end{cases} \Rightarrow \boldsymbol{f}_i^* = \boldsymbol{f}_i\,(\boldsymbol{a}_i) + \Delta\,\boldsymbol{f}_i, \tag{32a}$$

AMTD
3, 4967–5077, 2010

Then, the inversion of multi-pixel observations can be considered as solution the following combined equation system:

$$\begin{cases} \boldsymbol{f}_1^* = \boldsymbol{f}_1\,(\boldsymbol{a}_1) + \Delta\,\boldsymbol{f}_1 \\ \boldsymbol{f}_2^* = \boldsymbol{f}_2\,(\boldsymbol{a}_2) + \Delta\,\boldsymbol{f}_2 \\ \boldsymbol{f}_3^* = \boldsymbol{f}_3\,(\boldsymbol{a}_3) + \Delta\,\boldsymbol{f}_3 \\ \qquad \ldots \\ \boldsymbol{O}_x^* = \mathbf{S}_x\,\boldsymbol{a} + \Delta\,(\Delta_x\,\boldsymbol{a}) \\ \boldsymbol{O}_y^* = \mathbf{S}_y\,\boldsymbol{a} + \Delta\,(\Delta_y\,\boldsymbol{a}) \\ \boldsymbol{O}_t^* = \mathbf{S}_t\,\boldsymbol{a} + \Delta\,(\Delta_t\,\boldsymbol{a}) \end{cases}, \tag{32b}$$

where index "i" ($i = 1, 2, 3, \ldots$) denotes the number of each single pixel. Correspondingly, the total vector of unknowns $\boldsymbol{a}$ is composed from the vectors of unknowns $\boldsymbol{a}_i$ of each i-th pixel:

$$\boldsymbol{a} = \begin{pmatrix} \boldsymbol{a}_1 \\ \boldsymbol{a}_2 \\ \boldsymbol{a}_3 \\ \ldots \end{pmatrix}. \tag{33}$$

The matrices $\mathbf{S}_x$, $\mathbf{S}_y$ and $\mathbf{S}_t$ include the coefficients for calculating m-th differences (-numeral equivalent of m-th derivatives) of spatial (x-/y-) or temporal (t-) inter-pixel variability for each retrieved parameter a_k characterizing $dV(r_j)/d\ln r$, $n(\lambda_j)$, $k(\lambda_j)$, $\rho_o(\lambda_j)$, $\kappa(\lambda_j)$, $\Theta(\lambda_j)$; $\boldsymbol{O}_x^*$, $\boldsymbol{O}_y^*$, $\boldsymbol{O}_t^*$ – vectors of zeros and $\Delta(\Delta_x \boldsymbol{a})$, $\Delta(\Delta_y \boldsymbol{a})$ and $\Delta(\Delta_t \boldsymbol{a})$ – vectors of the uncertainties characterizing the deviations of the differences from the zeros.

The solution of the multi-pixel system can be implemented using formally the same sequence of the operations as shown in single pixel case. However, the minimized quadratic form $\Psi(\boldsymbol{a}^{\mathrm{p}})$, its gradient $\nabla\Psi(\boldsymbol{a}^{rmp})$ and Fisher Matrix $\mathbf{A}_{\mathrm{p}}$ formulated for inversion of combined multi-pixel Eq. (32) would be defined via correspondent single-pixel terms:

AMTD
3, 4967–5077, 2010
Statistically optimized inversion algorithm for enhanced retrieval
O. Dubovik et al.

$$\Psi\left(\boldsymbol{a}^{\mathrm{p}}\right) = \left(\sum_{i=1}^{N_{\text{pixels}}} \Psi_i\left(\boldsymbol{a}^{\mathrm{p}}\right)\right) + \left(\boldsymbol{a}^{\mathrm{p}}\right)^T \boldsymbol{\Omega}_{\text{inter}}\, \boldsymbol{a}^{\mathrm{p}}, \tag{34a}$$

$$\mathbf{A}_{\mathrm{p}} = \left[\begin{pmatrix} \mathbf{A}_{1,\mathrm{p}} & \mathbf{0} & \dots & \mathbf{0} \\ \mathbf{0} & \mathbf{A}_{2,\mathrm{p}} & \dots & \mathbf{0} \\ \dots & \dots & \dots & \dots \\ \mathbf{0} & \mathbf{0} & \dots & \mathbf{A}_{N,\mathrm{p}} \end{pmatrix} + \boldsymbol{\Omega}_{\text{inter}}\right], \tag{34b}$$

$$\nabla\Psi\left(\boldsymbol{a}^{\mathrm{p}}\right) = \left[\begin{matrix} \nabla\Psi_1\left(\boldsymbol{a}_1^{\mathrm{p}}\right) \\ \nabla\Psi_2\left(\boldsymbol{a}_2^{\mathrm{p}}\right) \\ \dots \\ \nabla\Psi_n\left(\boldsymbol{a}_n^{\mathrm{p}}\right) \end{matrix} + \boldsymbol{\Omega}_{\text{inter}}\, \boldsymbol{a}^{\mathrm{p}}\right], \tag{34c}$$

where $\Psi(\boldsymbol{a}^{\mathrm{p}})$, $\nabla\Psi\left(\boldsymbol{a}^{\mathrm{p}}\right)$ and $\mathbf{A}_{i,\mathrm{p}}$ are defined for N single pixels.

The smoothing inter-pixel matrix $\boldsymbol{\Omega}_{\text{inter}}$ is defined as:

$$\boldsymbol{\Omega}_{\text{inter}} = \gamma_x\, \mathbf{S}_x^T\, \mathbf{S}_x + \gamma_y\, \mathbf{S}_y^T\, \mathbf{S}_y + \gamma_t\, \mathbf{S}_t^T\, \mathbf{S}_t. \tag{34d}$$

It is easy to observe that if inter-pixel matrix $\boldsymbol{\Omega}_{\text{inter}}$ is eliminated the solution of the multi-pixel system of N pixels can be considered as solution of N independent single pixel systems. However, the matrix $\boldsymbol{\Omega}_{\text{inter}}$ has non-zero non-diagonal elements and $\nabla\Psi(\boldsymbol{a}^{\mathrm{p}})$ is not equal to a simple sum of $\nabla\Psi_i(\boldsymbol{a}_i^{\mathrm{p}})$. Therefore, the solution of the multi-pixel system of N pixels is not equivalent to the solution of N independent single pixel systems. At the same time, as shown in the Appendix A the inter-pixel smoothness matrix $\boldsymbol{\Omega}_{\text{inter}}$ is sparse and contains many zeros. This fact allows using multi-pixel constraints without significant increase of computation time. The definition of this matrix can be designed as follows.

Also, the values of Lagrange parameters γ_x, γ_y and γ_t are defined using similar concept discussed for applying smoothness constraints on variability aerosol and surface parameters in single pixel inversion scenario as shown in Eq. (29). The only difference is that in Eq. (29) the function $y_i(x)$ denotes the variability of each single parameter of aerosol or surface over x-, y- or t-coordinates. Note, that while Eq. (34) suggests the same strength of all constraints (that is done for clarity of formulation), the variability limitations can be very different for each single parameter. This is achieved by rather straightforward re-scaling of smoothing matrices corresponding to each single limitation (i.e. smoothing variability of each a_i over each of x-, y- or t-coordinates can be different). Also differences/derivatives of different order can be used in each single constraint. This strategy is fully implemented in the current algorithm.

The Table 4 outlines the details of inter-pixel constraints employed in the developed algorithm. Figure 5 shows the design of multi-pixel inversion algorithm as a rather straightforward generalization of single-pixel inversion.

The diagram in Fig. 6 emphasizes the similarity of multi-pixel inversion with N_{pixel} single-pixel retrievals. The difference is only in the additions of the inter-pixel smoothing terms into the N_{pixel} – pixel joint *Normal System*. As outlined above the matrix $\mathbf{\Omega}_{\text{inter}}$ defining the inter-pixel smoothing terms is very sparse and transparent, therefore computer time required for definition of these smoothing terms is insignificant compare to other calculations performed in the inversion. Another difference is that multi-pixel approach requires solving the N_{pixel} pixels joint *Normal System* that can have rather high dimension. At the same time, the *Fisher matrix* $\mathbf{A}_{\text{p}}$ of this system is also very sparse and a number of numerical tools are available for optimizing the solution of linear system with such structure.

4.2.2 Inter-connection between neighboring groups in multiple-pixel fitting

The previous Section described the simultaneous inversion of a group of pixels. The proposed multi-pixel strategy uses expected continuity in pixel-to-pixel variability of aerosol and land surface properties as an additional retrieval constraint. At the same time pixel group has limited size: $N_x \times N_y \times N_t$. One can naturally expect the continuity/similarity of aerosol and surface properties observed the edges of this pixel group

AMTD
3, 4967–5077, 2010

Statistically optimized inversion algorithm for enhanced retrieval

O. Dubovik et al.

and with the properties in the pixels-neighbors located just outside of the $N_x \times N_y \times N_t$ pixel group. These additional constraints enforcing continuity of retrieved properties between different inverted groups of pixels can be rather logically added to the inversion formulations described in preceding Sections. As shown by detailed derivation in Appendix B, the additional conditions of continuity of aerosol and surface properties with the values of correspondent parameter in the neighborhood of the inverted pixel group can be implemented by adding extra terms in the Eqs. (34). Specifically, the minimized quadratic form $\Psi(\boldsymbol{a}^{\mathrm{p}})$, its gradient $\nabla\Psi(\boldsymbol{a}^{\mathrm{p}})$ and Fisher Matrix $\mathbf{A}_{\mathrm{p}}$ will include the extra-terms $\Psi_{\mathrm{edge}}(\boldsymbol{a}^{\mathrm{p}})$, $\nabla\Psi_{\mathrm{edge}}(\boldsymbol{a}^{\mathrm{p}})$ and $(\mathbf{A}_{\mathrm{p}})_{\mathrm{edge}}$ accordingly. As demonstrated in Appendix B, these additional terms are rather transparent and can be calculated with very minor computational efforts. At the same time, this way of equation organization provides rather practically powerful additional tool of constraining the retrieval. Indeed, the inversion of the satellite observations over large geographical area and extended time period can not be implemented simultaneously due to natural limitations of the computer resources. Instead, the large records of the satellite observations can be inverted sequentially by small pixel parcels/groups of limited $N_x \times N_y \times N_t$ size. Adding intergroup constraints makes such sequential retrieval nearly equivalent to simultaneous inversion of all data. The only difference is that the retrieval for each small pixel group would not benefit from the information contained in the observations over the pixels inverted in subsequent retrieval acts. At the same time, the retrieval would fully benefit from all preceding retrievals. Thus, taking into account that spatial and temporal correlation of aerosol and surface properties has rather limited range one can expect that sequential pixel parcel-by-parcel retrieval with the inter-parcel continuity constraints should produce the extended fields of the retrieved parameters of high consistency enforced by unified inter-pixel constraints.

It is worthwhile mentioning the analogy of the sequential parcel-by-parcel retrieval with the *Kalman Filter* type retrieval sequences. For example, if the "edge" inter-pixel constraints are implemented using only first differences, and if they were applied only in time dimension (when the retrieved values of unknowns in the given time are used to constrain the solution in consequent time moment), then the technique described above in this Section becomes full equivalent of known *Kalman Filter* retrieval technique (Kalman, 1960).

4.2.3 Assuming common parameters for several different pixels in the retrieval

The multi-pixel retrieval scheme suggested in above Sections takes the benefits of the limited spatial variability of aerosol or land surface for different pixels or temporary for the same pixel. However, there are some situations when it reasonable to assume that some parameters do not change at all from pixel to pixel. For example, in the retrieval algorithms developed for geostationary observations, the land surface reflectance parameters and most of aerosol parameters are assumed diurnally constant (e.g. Govaert et al., 2010). Moreover, even in the retrievals of aerosol from polar-orbiting observations (e.g. POLDER, MODIS), neglecting surface properties variations on small time scales can be reasonable assumption. Therefore, a possibility of assuming the inter-pixel invariant parameters can be useful option for constraining the retrieval and verifying the importance of neglected variations.

Inclusion of such assumptions, in principle, can be implemented by a significant increase of the corresponding Lagrange multiplier in Eq. (34b) and Eqs. (B22–B25) (in Appendix B). This would enforce very high correlation between correspondent retrieved parameters make them practically equal. However, such enforcement of the full dependence of the retrieved parameters has serious deficiencies. Indeed, the increase of γ_t would result into a strong increase the smoothness matrices $\mathbf{\Omega}_{\text{inter}}$ and $\mathbf{\Omega}_{\text{edge}}$ contributions into the total *Fisher matrix* in Eqs. (B34) and (B24) (in Appendix B). This would enforce very high correlation between correspondent retrieved parameters, by making them practically equal. Correspondently, making contributions of $\mathbf{\Omega}_{\text{inter}}$ and $\mathbf{\Omega}_{\text{edge}}$ dominant would doubtlessly produce degenerated *Normal systems*. Therefore, if one can expect that properties of aerosol or surface in different pixels do not change, the retrieval of a single group of those constant parameters for many observation pixels seems more logical than the retrieval of several groups of the parameters (one group

AMTD

3, 4967–5077, 2010

Statistically optimized inversion algorithm for enhanced retrieval

O. Dubovik et al.

per each pixel) forced by the enhanced smoothness constraints to have very close values in different pixels. For example, this retrieval approach leads to significantly smaller number of the simultaneously retrieved parameters that essentially simplifies the numerical inversion. However, if the algorithm is based on this straightforward strategy it looses flexibility, because practical implementation of the algorithm allowing easy increase or decrease of the number of fixed parameters is logistically very challenging. Therefore, here another approach is suggested. The approach uses the general formulation of the inversion strategy via inter-pixel smoothness constraints even for retrieval scenarios when some derived parameters are fixed to be the same for different observations (e.g. assuming that some parameters of BRF are intra-day independent over the same pixel) or even for one set of observation (e.g. assuming that some parameters of BRF are spectrally independent in any single pixel).

The approach is the following. First, the *Normal system* is built under the assumption that every single parameter that drives the forward model is retrieved. Then, as shown in Appendix C, fixing several parameters equal in the inversion can be achieved by rather simple modification of the *Normal system* without any other changes in the inversion algorithm. Assuming one has defined *Fisher matrix* $\mathbf{A}^{(N)}$ and gradient $\nabla\Psi^{(N)}$ for deriving N parameters a_i. Then if it was decided that $n+1$ parameters are equal, i.e. $a_i = a_{i_k}$ ($k = 1, \ldots, n+1$), this assumption can be implemented simply by decreasing dimensions of *Fisher matrix* and *gradient* by summing up $n+1$ of lines and columns of the equal parameters. As a result the solution can be obtained by solving modified *Normal system* with *Fisher matrix* $\mathbf{A}^{(N-n)}$ and *gradient* $\nabla\Psi^{(N-n)}$ of smaller dimensions: $(N-n)\times(N-n)$ and $(N-n)$ correspondingly. The details are shown in Appendix C. It is important to note that the described reorganization of the *Normal system* is rather straightforward and is not time consuming.

Discussion Paper | Discussion Paper | Discussion Paper | Discussion Paper |

AMTD

3, 4967–5077, 2010

Statistically optimized inversion algorithm for enhanced retrieval

O. Dubovik et al.

5 Algorithm functionality and sensitivity tests

The algorithm is designed to retrieve rather extended set of parameters describing the atmospheric aerosol and underlying surface reflectance. The list of the parameters is given in the Table 1. The algorithm derives basically the same group of aerosol parameters in both scenarios of observation over ocean or land. At the same time, there is some flexibility in setting the representation of aerosol size distribution. The sized distribution can be modeled using different number of size bins N_i: (i) large number of the size bins ($N_i \geq 10$) modeled as tri-angle functions; (ii) small number of the size bins ($N_i < 10$) modeled as log-normal size functions with different assumed width. The smaller number of bins can be set for reducing retrieval implementation time. The retrieval of large number size bins can be preferable options in situation when observations are more sensitive to detail of aerosol properties. For example, contribution of the atmospheric aerosol dominates the POLDER observations over dark ocean surface. The modeling of ocean surface reflection fully follows the approach the currently operational POLDER algorithm (Deuzé et al., 2000; Herman el al., 2005). The only difference assumed in the developed algorithm is a possibility to retrieve one single parameter (wind speed) of horizontally isotropic Cox-Munk model.

The design of the inversion algorithm allows two complementary inversion scenarios. The conventional *Single-Pixel Inversion* is designed to retrieve all above aerosol and surface parameters for each single pixel of observation. The *Multi-Pixel Retrieval* implements the simultaneous inversion of satellite observations over a group of the neighboring pixels obtained during the limited time period (e.g. several weeks). This strategy allows applying rather diverse constraints on variability of every retrieved parameter in space and time. It also allows assumption of time or space pixel independence of any single parameter or a group of the retrieved parameters. Based on the known experience in aerosol and land surface retrieval developments, and on general understanding of limitations of the information content (checked in sensitivity tests) the following

AMTD
3, 4967–5077, 2010

combination of assumptions has been chosen for applying to POLDER/PARASOL observations.

For aerosol (within each single pixel):

- The aerosol size distribution is assumed smooth;
- The spectral dependence of $n(\lambda_i)$ and $k(\lambda_i)$ is assumed smooth;

For aerosol (between pixels):

- The moderate spatial variability is assumed for all aerosol parameters with the exception of aerosol loading (driven by aerosol total concentration);
- Significant spatial variability of aerosol loading (total concentration) is allowed;

For surface reflectance (within each single pixel):

- $\rho_o(\lambda)$ is assumed moderately spectrally smooth;
- $\kappa(\lambda)$ and $\Theta(\lambda)$ are assumed strongly spectrally smooth (nearly constant).
- (if retrieved) $h_o(\lambda)$ is assumed moderately spectrally smooth;
- $B(\lambda_i)$ is assumed strongly to moderately spectrally smooth;

For surface reflectance (between pixels):

- All parameters of surface reflectance are assumed constant during ~7 days;
- *No constraints are applied at spatial variability of the parameters*;

Table 5 summarizes the above assumptions and Tables 3 and 4 show the Lagrange parameters used form applying smoothness constraints on the size or spectral dependencies of the retrieved aerosol and surface properties in each single pixel and on the spatial and temporal variability of the any single retrieved parameter between the different pixels.

AMTD
3, 4967–5077, 2010

A series of the sensitivity tests has been performed to verify the performance and potential of the developed algorithm. The tests have been designed to provide rather compact and conclusive illustration of capabilities and limitations of the algorithm to derive full set of aerosol and surface reflectance parameters from POLDER type satellite observations. The discussion bellow will be focused on the satellite observations over land surfaces. The tests verifying the performance of the algorithm over dark surfaces are not discussed in this paper. Nonetheless such tests were also performed and they showed rather robust retrieval all aerosol parameters in most tested situations. Some results of such tests have been shown in the paper by Kokhanovsky et al. (2010) that discusses the outcome of the series of aerosol retrieval "blind test". In the framework of this study the observations of aerosol over dark surface by different satellites were simulated for a single chosen undisclosed aerosol model. These observations were distributed to different research groups involved in aerosol retrieval developments. The groups willing to participate in such test have derived the aerosol properties from the obtained synthetic observations and returned the obtained aerosol retrieval results to the distributor of the data. Once all retrieval results were collected, the assumed aerosol model has been disclosed and compared with the collected retrieval results. Based on the analysis of the "blind test" outcome the present algorithm (mentioned in the paper by Kokhanovsky et al., 2010 as "LOA-2") was rated among the algorithms providing most comprehensive and rather accurate results. The retrieval results provided for studies by Kokhanovsky et al. (2010) were obtained using conventional pixel-by-pixel retrieval approach.

The sensitivity tests for retrieval over land surface were aimed to verify the performance of the retrieval approach in the conditions maximally reproducing the real environment. With that purpose, the POLDER observation geometry, the aerosol and surface characteristics have been assumed to mimic closely the observations over two AERONET (Holben et al., 1998) observations site: Banizoumbou (Niger) and Mongu (Zambia). The properties of both aerosol and surface reflectance were expensively studied and discussed in the scientific literature. For example, the observations over

Banizoumbou were discussed in a number of papers (Rajot et al., 2008; Formenti et al., 2008; Johnson et al., 2009; Sow et al., 2009, etc), the observations over Mongu were discussed in many studies (Dubovik et al., 2002a; Eck et al., 2003; Schmid et al., 2003; Haywood et al., 2003; Lyapustin et al., 2006; Sinuyk et al., 2007, etc). Two rather distinct aerosol types dominate the aerosol over AERONET sites: desert dust and biomass burning. Mongu is highly affected by biomass burning aerosol. The aerosol over Banizoumbou site is strongly impacted by the desert dust outbreaks with notable seasonal contributions of smoke. The biomass burning is known to be dominated by fine absorbing spherical particles. All optical properties of biomass burning aerosol (extinction, single scattering albedo, etc) generally have distinctly decreasing spectral dependence (e.g. Eck et al., 1999; Dubovik et al., 2002a; Reid et al., 2005, etc). In a contrast, desert dust is dominated by coarse non-spherical and weakly absorbing particles. Therefore, the extinction of desert dust is generally spectrally flat (e.g. Eck et al., 1999; Holben et al., 2001, etc). Dust particles generally are nearly non-absorbing in visible with some moderate absorption appearing at ~0.5 micron and increasing towards UV spectral range (e.g. Kaufman et al., 2001; Dubovik et al., 2002a; Lafon et al., 2006, etc). Biomass fine aerosol particles strongly polarize the scatted light, while the polarization by coarse non-spherical desert dust particles is weak (e.g. Volten et al., 2001; Dubovik et al., 2006; etc). The two series of tests were conducted: (i) when desert dust was dominating and (ii) when biomass burning was dominating. The sensitivity tests were carried out for a wide range of aerosol loadings. The 16 test scenarios were designed to cover the range from $\tau(0.44) = 0.01$ to $\tau(0.44) = 4$. The size distributions: for both biomass and desert dust aerosol models were adapted from original observations over Banizoumbou and Mongu AERONET sites. The 22 AERONET size distribution bins were used for generating synthetic observations. Since the size distributions were adapted from actual AERONET observations, they did not have perfect multi-modal shape. This fact makes the tests more challenging but more realistic. The values of complex refractive index for $\lambda = 0.44$, 0.67, 0.87 and 1.02 µm were adapted from actual AERONET observations. The values for intermediate spectral channels

AMTD
3, 4967–5077, 2010

$\lambda = 0.49$ and $0.55\,\mu$m were obtained by the interpolation. At the same time it should be noted that values chosen for both the size distribution and complex refractive index are generally close to the values reported from AERONET retrieval climatology for dust and biomass burning by Dubovik et al. (2002a).

The random noise at the level of 1% for intensity and 0.5% for degree of linear polarization of PARASOL signal have been added to the simulated "synthetic" PARASOL observations. These synthetic observations were inverted by the present algorithm using two retrieval scenarios: conventional pixel-by-pixel and multi-pixel retrieval. In the first scenario all synthetic observations were inverted fully independently. For multi-pixel retrieval, the "synthetic" PARASOL observations were assumed to be observed during ~ one week in four consequent observations (with time difference of 1 to 2 days). It was assumed that the four neighboring pixels were observed at each observation time. For example, Fig. 5 shows situation, when 9 (3×3, where $N_x = 3$ and $N_y = 3$) pixels observed during 3 consequent observations. One can imagine similar case when 4 (2×2, where $N_x = 2$ and $N_y = 2$) pixels observed during 4 consequent observations. The constraints were applied on the inter-pixel variability of the retrieved aerosol and surface properties as described above in this Section and summarized in Tables 2–5. Specifically, the properties of the surface reflectance were assumed constant during the week for the same pixels and all aerosol parameters (except loading) was assumed only weakly variable horizontally during the same day. No constraints were applied on neither temporal nor horizontal variability of aerosol concentration. All retrievals in the tests are conducted using most detailed size distribution representation: 16 logarithmically equidistant size bins covering the range of aerosol particle radii from 0.1 to 7 microns. The same initial guess was used for the unknown parameters in every pixel. It is described in Table 6.

Figures 7–10 show the results of the sensitivity test for retrieving biomass burning aerosol over Mongu. Each figure shows the retrieval results for three situations. Left part of each figure shows the results of the retrieval for the case with no noise added. It should be noted however, that some discrepancies were present even in this case since

AMTD
3, 4967–5077, 2010

the size distribution is modeled using 22 logarithmically equidistant size bins covering range of particle radii from 0.05 to 15 microns, while retrieval uses only 16 size bins covering radii from 0.1 to 7 microns. The central and the right parts of each figure show the results of the retrieval with no noise added at the level of 1% for total radiances and 0.5% for degree of linear polarization. Both the left and central parts show the results obtained using conventional pixel-to-pixel retrieval approach, while the right part of each figure shows results obtained using multi-pixels retrieval strategy. Figures 11–14 are analogous to Figs. 7–10 with the difference that they illustrate the retrieval results of desert dust over Banizoumbou (Niger).

The analysis of the results shows, that in situation when no noise added all aerosol characteristics are retrieved rather accurately. Some notable deviations are seen for single scattering albedo and size distribution in situations with very low aerosol loading when $\tau(0.44) \leq 0.2$. The deviations are particularly notable for the size distribution retrievals of the course size particles and for single scattering albedo of biomass burning at long wavelengths. These deviations can be explained by the fact that at such low aerosol loadings the aerosol contribution into radiation observed by satellite is negligible compare to the contribution of land surface reflectance. Therefore even minor perturbations of the observation may significantly affect the retrieval results. In a contrast, in situations with very high aerosol loading $\tau(0.44) \geq \sim 2$–2.5, the contribution of aerosol dominates in the observed reflected radiation and the reflectance properties of the underlying land surface become nearly invisible for satellite. Correspondingly, the retrievals of surface reflectance become unstable, as it is seen for retrieved surface reflectance values at short wavelengths. All these tendencies become pronounced once the random noise is added. As one can see from central parts of Figs. 7–14, the size distribution and single scattering albedo retrieved by conventional pixel-by-pixel approach deteriorate in most of the cases including the situations with moderate and even high aerosol loading with $\tau(0.44)$ reaching 0.4 and even 0.8 (for single scattering albedo in particular). In addition one can see the significant complications in the retrieval of shape of aerosol size distribution, in particular for larger particle sizes. The

AMTD
3, 4967–5077, 2010

size distribution retrieved for desert dust (see Fig. 12) becomes much wider and the maximum shifts towards smaller sizes. In retrievals of biomass burning size distributions (Fig. 8) there are also significant complications for the large radii. This difficulty can be explained by well-known fact (e.g. see Bohren and Huffman, 1983) of strongly decreasing scattering efficiency (per unite of particle volume) for particles with sizes much larger than the wavelengths of observations. Therefore retrieving accurate shape of size distribution for radii $\geq\sim 3\,\mu m$ from POLDER/PARASOL observations appears to be very difficult. The retrieval of aerosol optical thickness $\tau(0.44)$ seems to be rather reliable in situations when random noise is added with the exceptions of the cases of very high aerosol loading $\tau(0.44) \geq\sim 3$ where the retrieval errors reach the values of 0.5 or even larger (see Fig. 7). These high errors can be explained by the fact that in such situations the reflected radiances are dominated by the multiple scattering of very high orders and they have less dependence on scattering angle. Correspondingly, deriving detailed aerosol and surface properties becomes more difficult. The analysis of the right parts of Figs. 7–14 shows that using multi-pixel approach significantly improves the retrievals of all aerosol and surface parameters. This tendency is not surprising because added constraints allow propagation and consolidation of useful information from different observational situations. For example, in the situations with low aerosol loading the satellite observes mainly surface reflectance properties. Correspondingly, once the constraints limiting time variability of the surface reflectance are applied, this information is supplied into the interpretations of observations corresponding moderate and high aerosol loading over the same pixel. Similarly, the constraints of horizontal variability of aerosol properties help improving the retrieval of aerosol by benefiting from observations of the same or similar aerosol properties over several pixels with somewhat different conditions of observations (geometry, surface reflectance, aerosol loading).

It should be noted that, such retrieved parameters as aerosol mean height, fraction of spherical particles, detailed parameters of BRF and BPRF, are not shown in Figs. 7–14. All these parameters have been included in the tests. However, in order to keep the article size reasonably limited, the results for each parameter are not included in the figures. The results are shown only for most significant aerosol and surface parameters commonly discussed in remote sensing retrieval analysis. In a future study, it is planned to implement the comprehensive sensitivity analysis of the retrieval approach suggested here. The sensitivity studies shown in the present paper are aimed to provide insightful but preliminary outlook at the expected performance of the retrieval. Nonetheless, it is possible to state here that the tests have shown reasonably robust retrieval of all sought parameters. Figures 11 and 14 show the retrieval of total albdeo of the surface reflectance. The retrievals of the detailed BRF and BPRF parameters generally demonstrate the same trends. In pixel-by-pixel retrieval scenario all parameters were retrieved rather accurately in situations with low and moderate aerosol loading. Using multi-pixel retrieval helped to achieve stable retrieval of all surface reflectance parameters in all situations including the cases with high aerosol loading. In a contrast, the retrieval of the mean altitude of the aerosol layer h_a was retrieved robustly when aerosol loading was moderate or high. When pixel-by-pixel retrieval scenario was used, h_a was retrieved with accuracy better than 1 km for $\tau(0.44) \geq\sim 0.5$ and better than 0.5 km for $\tau(0.44) \geq\sim 1.0$. Once the multi-pixel scenario was applied, h_a was retrieved with accuracy better than 0.5 km for $\tau(0.44) \geq\sim 0.5$ and better than 0.3 km for $\tau(0.44) \geq\sim 1.0$. The retrieval of the spherical particle fraction was rather successful for desert dust aerosol, where the coarse mode is dominant. When pixel-by-pixel retrieval scenario was used, C_{sph} was retrieved with the accuracy of ~50% in situation with $\tau(0.44) \geq\sim 0.2$ and better than 20% for $\tau(0.44) \geq\sim 1.0$. In multi-pixel retrieval scenario it was retrieved with the accuracy of ~30% in situations with $\tau(0.44) \geq\sim 0.2$ and better than 10% for $\tau(0.44) \geq\sim 1.0$.

Finally, Figs. 15–18 summarize the performance of the retrieval in an extended series of numerical tests with added random noise. The series were composed by the tests analogous to those illustrated in Figs. 7–14, with the different that each test was repeated 100 times with different realizations of the generated noise. The random noise was added at the level of standard deviation $\sigma = 1\%$ for total radiances and

Discussion Paper | Discussion Paper | Discussion Paper | Discussion Paper |

AMTD

3, 4967–5077, 2010

Statistically optimized inversion algorithm for enhanced retrieval

O. Dubovik et al.

$\sigma = 0.5\%$ for polarized radiances. Thus the Figs. 15–18 show the results of 3200 inversions = 100 × 16 × 2 (100 – noise realizations; 16 – aerosol loading covering $\tau(0.44)$ from 0.01 to 4.0; 2 – number of observational sites: Banizoumbou and Mongu). Figures 15–18 show the differences: (τ (retrieved) – τ(“true”))/τ(“true”) and ϖ_0 (retrieved) – ϖ_0 (“true”) for λ 0.44 and 1.02 µm. All retrievals were conducted using most robust multi-pixel retrieval scenario. Table 7 provides the brief summary of the tests outcome. These estimates can be considered as the reference values for the expected retrieval errors. It should be noted that the real error are likely to have 2 times higher levels than the errors modeled. Therefore, the actual retrieval errors should be expected higher by about two times than the numbers given in the Table 7. In any case, these estimates are to be verified in a more comprehensive sensitivity analysis.

6 Algorithm applications to real POLDER/PARASOL observations

As a final stage of this study the developed algorithm was applied to actual observations by POLDAER/PARASOL. For coherency with the sensitivity test, the algorithm was used to process full 2009 year of POLDAER/PARASOL data over Banizoumbou (Niger) and Mongu (Zambia) AERONET sites. Specifically, the algorithm was applied for 4 POLDER/PARASOL pixels surrounding the exact locations of the sites. The multi-pixel inversion scenario was employed in the retrieval. Since the current studies did not address the cloud-screening of the satellite data, the algorithm was applied to the PARASOL data identified as cloud-free by current operational POLDER algorithm (Deuzé et al., 2000; Herman el al., 2005). In addition, the retrieval outliers with the fitting residual higher than 5% were eliminated from the final results. The retrieval results were compared with availiabe AERONET data. The comparisons showed rather robust performance of the algorithm. The retrieved values of aerosol optical thickness closely followed the AERONET observation with correlation coefficient of ∼0.9 for Banizoumbou and ∼0.87 for Mongu. The values of aerosol single scattering albedo also agreed reasonably well with AERONET data for observations with high aerosol loading. The differences between the values of $\omega_0(0.44)$ obtained from PARASOL and from AERONET did not exceed 0.03–0.05 for the cases when $\tau(0.44) \geq\sim 0.5$.

Figures 19–20 illustrate the comparison of POLDER/PARASOL retrievals with the AERONET observations during 2 months over Banizoumbou and Mongu. These particular periods were chosen for the illustrations, because they corresponded to the most complete and continuous AERONET data records during the seasons with the presence of the high aerosol loadings. As can be seen from the illustrations the aerosol loading trends retrieved from PARASOL agrees well with the AERONET observations. The values of aerosol single scattering albedo are also in reasonable agreement with AERONET values when $\tau(0.44) \sim 0.5$ or larger. At the same time, one can identify some notable differences between AERONET data and PARASOL retrievals in some single points. Nonetheless, our analysis showed that usually these points correspond to the days when AERONET data indicate the some partial cloudiness during the day as identified by Smirnov et al. (2000) cloud-screening procedure. Therefore, such outliers can probably be explained by some sky inhomogeneities in the one or all PARASOL observed pixels that cover area of 12 × 12 km around AERONET site. It should be also noted that comparisons of AERONET observations and PARASOL retrieval results showed that obtained retrievals tend to underestimate spectral dependence of retrieved aerosol properties. The desert dust retrievals tend to show more pronounced spectral dependence of aerosol properties, while the aerosol properties retrieved for biomass burning tend to have smaller spectral dependence than observed from AERONET. As it follows from sensitivity tests and general understanding, this issue is likely to be originated from very low sensitivity of satellite observations to the shape of aerosol size distribution for large particle radii. Indeed, the contribution of very large particles ($r > 3$ µm) into radiation reflected to the space is significantly smaller than from fine particles, while the spectral variability of aerosol properties is very sensitive to the presence of such large particles. Therefore, deriving fully adequate spectral dependence of aerosol optical properties from satellite observations appears to be harder task than deriving aerosol loading especially over bright land surfaces considered in

AMTD
3, 4967–5077, 2010

Statistically optimized inversion algorithm for enhanced retrieval

O. Dubovik et al.

present test. Apart of this relatively minor issue the present analysis showed very encouraging performance of the developed algorithm over bright land surfaces, i.e. in the conditions that are considered traditionally as the most difficult for retrieval of aerosol from satellites. This result is particularly encouraging because the algorithm is designed to provide rather extensive set of the retrieved parameters providing detailed characterization of the properties of aerosol and underlying surface. At the same time, the results presented are preliminary. Further testing, verification and tuning of the presented algorithm are planned.

7 Conclusions

The paper has discussed in details a concept of new state-of-the-art algorithm developed for deriving detailed properties of atmospheric aerosol from satellite observations. The proposed retrieval does not use precalculated look-up tables commonly utilized in the satellite retrievals for fitting observations. Instead, more general approach is applied that searches in continuous space of the solutions and optimizes statistical properties of the obtained retrieval. Such optimization can be achieved by adjusting the structure of the deviations in the efforts to fit observations by theoretical model under condition that the amount of observations exceeds the number of retrieved parameters. The set of observations provided by modern enhanced spectral multi-viewing spectral polarimeters allows applying such optimization. The algorithm described in this paper was adapted for applying to the observations of POLDER/PARASOL imager that registers atmospheric radiances at six wavelengths in up to 16 directions. The algorithm fits total and polarized radiances observed in all directions in all available spectral channels using generalized multi-term *Least Square* type numerical inversion formulation. That formulation allows fitting several sets of both observations and a priori data. The concept complementarily unites advantages of a variety of practical inversion approaches, such as *Phillips-Tikhonov-Twomey* constrained inversion, *Kalman filter*, *Newton-Gauss* and *Levenberg-Marquardt* iterations, etc. This methodology has

AMTD
3, 4967–5077, 2010

resulted from the multi-year efforts on developing inversion algorithms for retrieving comprehensive aerosol properties from AERONET ground-based observations. The algorithm is driven by large number of unknowns and designed as a retrieval of extended set of parameters affecting measured radiation. For example, over land the algorithm is set to retrieve parameters of the land surface reflectance together with detailed information about aerosol sizes, shape, absorption and composition (refractive index) and aerosol layer elevation.

In addition, the algorithm is developed as simultaneous inversion of a large group of pixels within one or several images. Such, multi-pixel retrieval regime takes advantage from known limitations on spatial and temporal variability in both aerosol and surface properties. Specifically the pixel-to-pixel and/or day-to-day variations of the retrieved parameters are enforced to be smooth by additional appropriately set a priori constraints. This concept is aimed to achieve higher consistency satellite retrieval, because in such approach the solution over each single pixel is benefiting from information contained in co-incident observations over neighboring pixels, as well, from the information about surface reflectance (over land) obtained in preceding and consequent observations over the same pixels. The paper provided detailed description of full set of formulations necessary for realizing this concept.

The performance of the developed algorithm has been demonstrated by application to both synthetically generated and real POLDER/PARASOL observations. First, a series of sensitivity tests was conducted by applying the algorithm to the synthetic POLDER/PARASOL observations over green vegetated and desert surfaces. The simulations were designed to mimic satellite observations over well-studied AERONET network sites in Mongu (Zambia) and Banizoumbou (Niger). The synthetic POLDER/PARASOL signals were perturbed by random noise prior applying the retrieval algorithm. Both the conventional pixel-by-pixel and newly suggested multi-pixel retrieval approaches were tested. The results of the tests showed that the complete set of aerosol parameters can be robustly derived with acceptable accuracy in both situations over both vegetated and desert surfaces. The summary of the error analysis is

AMTD
3, 4967–5077, 2010

provided. In addition, the algorithm was applied to one year of PARASOL observations over both Mongu and Banizoumbou AEROENT sites. The comparison of the derived aerosol properties with available observations by AERONET ground-based sun/sky-radiometers indicated encouraging consistency of PARASOL derived optical thickness and single scattering albedo with those obtained by AERONET. At the same time, the presented tests and analysis of the retrieval from actual PARASOL observation had somewhat limited character and were aimed to provide an introduction and some limited illustration of the proposed retrieval algorithm. More comprehensive studies for testing and tuning the developed algorithm are planned in the future efforts.

It is should be noted that the research efforts described in the paper considerably relied on the accumulated experience and many aspects of the retrieval, as well as, actual computer tools were inherited from precedent efforts on development of currently operating AERONET retrieval and PARASOL aerosol retrieval algorithms.

Appendix A

Matrices of multi-pixel smoothness constraints

In order to determine the index of pixels we will follow first the changes of x_i – coordinates ($i = 1, ..., N_x$) than y_i – coordinates ($i = 1, ..., N_y$) and t_i – time coordinates ($i = 1, ..., N_t$). For the simples case when $N_x = N_y = N_t$=2, the total vector of unknowns $\boldsymbol{a}$ is composed from the vectors $\boldsymbol{a}_i$ of each i-th pixel as:

AMTD
3, 4967–5077, 2010

$$\boldsymbol{a} = \begin{pmatrix} \boldsymbol{a}\,(x_1;\, y_1;\, t_1) \\ \boldsymbol{a}\,(x_2;\, y_1;\, t_1) \\ \boldsymbol{a}\,(x_1;\, y_2;\, t_1) \\ \boldsymbol{a}\,(x_2;\, y_2;\, t_1) \\ \boldsymbol{a}\,(x_1;\, y_1;\, t_2) \\ \boldsymbol{a}\,(x_2;\, y_1;\, t_2) \\ \boldsymbol{a}\,(x_1;\, y_2;\, t_2) \\ \boldsymbol{a}\,(x_2;\, y_2;\, t_2) \end{pmatrix}. \tag{A1}$$

The spatial and time smoothness constraints are applied separately along correspondent coordinates, i.e. constraints of variability over x_i – coordinates are applied only to the vectors with the same values of y_i and t_i; constraints of variability over y_i – coordinates are applied only to the vectors with the same values of x_i and t_i and constraints of variability over t_i – coordinates are applied only to the vectors with the same values of x_i and y_i. Therefore, if $\Delta x = x_{i+1} - x_i$ =const, $\Delta y = y_{i+1} - y_i$ =const and $\Delta t = t_{i+1} - t_i$ =const, for the vector $\boldsymbol{a}$ defined by Eq. (A1) the correspondent matrices of first differences are defined as:

$$\mathbf{S}_x = \begin{pmatrix} 1 & -1 & 0 & 0 & 0 & 0 & 0 & 0 \\ 0 & 0 & 1 & -1 & 0 & 0 & 0 & 0 \\ 0 & 0 & 0 & 0 & 1 & -1 & 0 & 0 \\ 0 & 0 & 0 & 0 & 0 & 0 & 1 & -1 \end{pmatrix}; \quad \mathbf{S}_y = \begin{pmatrix} 1 & 0 & -1 & 0 & 0 & 0 & 0 & 0 \\ 0 & 1 & 0 & -1 & 0 & 0 & 0 & 0 \\ 0 & 0 & 0 & 0 & 1 & 0 & -1 & 0 \\ 0 & 0 & 0 & 0 & 0 & 1 & 0 & -1 \end{pmatrix}; \quad \mathbf{S}_t = \begin{pmatrix} 1 & 0 & 0 & 0 & -1 & 0 & 0 & 0 \\ 0 & 1 & 0 & 0 & 0 & -1 & 0 & 0 \\ 0 & 0 & 1 & 0 & 0 & 0 & -1 & 0 \\ 0 & 0 & 0 & 1 & 0 & 0 & 0 & -1 \end{pmatrix} \tag{A2}$$

Correspondingly the terms of matrix $\mathbf{\Omega}_{\text{inter}}$ can be written in the form of the following array matrices:

$$\mathbf{S}_x^T\,\mathbf{S}_x = \begin{pmatrix} \begin{pmatrix} \mathbf{D} & \mathbf{0} \\ \mathbf{0} & \mathbf{D} \end{pmatrix} & \begin{pmatrix} \mathbf{0} & \mathbf{0} \\ \mathbf{0} & \mathbf{0} \end{pmatrix} \\ \begin{pmatrix} \mathbf{0} & \mathbf{0} \\ \mathbf{0} & \mathbf{0} \end{pmatrix} & \begin{pmatrix} \mathbf{D} & \mathbf{0} \\ \mathbf{0} & \mathbf{D} \end{pmatrix} \end{pmatrix}; \quad \mathbf{S}_y^T\,\mathbf{S}_y = \begin{pmatrix} \begin{pmatrix} \mathbf{I}_{d_{11}} & \mathbf{I}_{d_{12}} \\ \mathbf{I}_{d_{21}} & \mathbf{I}_{d_{22}} \end{pmatrix} & \begin{pmatrix} \mathbf{0} & \mathbf{0} \\ \mathbf{0} & \mathbf{0} \end{pmatrix} \\ \begin{pmatrix} \mathbf{0} & \mathbf{0} \\ \mathbf{0} & \mathbf{0} \end{pmatrix} & \begin{pmatrix} \mathbf{I}_{d_{11}} & \mathbf{I}_{d_{12}} \\ \mathbf{I}_{d_{21}} & \mathbf{I}_{d_{22}} \end{pmatrix} \end{pmatrix}; \quad \mathbf{S}_t^T\,\mathbf{S}_t = \begin{pmatrix} \begin{pmatrix} \mathbf{I}_{d_{11}} & \mathbf{0} \\ \mathbf{0} & \mathbf{I}_{d_{11}} \end{pmatrix} & \begin{pmatrix} \mathbf{I}_{d_{12}} & \mathbf{0} \\ \mathbf{0} & \mathbf{I}_{d_{12}} \end{pmatrix} \\ \begin{pmatrix} \mathbf{I}_{d_{21}} & \mathbf{0} \\ \mathbf{0} & \mathbf{I}_{d_{21}} \end{pmatrix} & \begin{pmatrix} \mathbf{I}_{d_{22}} & \mathbf{0} \\ \mathbf{0} & \mathbf{I}_{d_{22}} \end{pmatrix} \end{pmatrix}, \tag{A3}$$

where smoothness matrix $\mathbf{D}$ is defined as:

$$\mathbf{D} = \begin{pmatrix} d_{11} & d_{12} \\ d_{21} & d_{22} \end{pmatrix} = \mathbf{S}_1^T\,\mathbf{S}_1 = \begin{pmatrix} 1 & -1 \\ -1 & 1 \end{pmatrix}, \tag{A4}$$

AMTD

3, 4967–5077, 2010

Statistically optimized inversion algorithm for enhanced retrieval

O. Dubovik et al.

where $\mathbf{S}_1$ is the matrix of first differences. The matrix $\mathbf{I}_{\mathrm{d}_{ij}}$ is a diagonal matrix of dimension $N_\mathrm{a} \times N_\mathrm{a}$ (N_a is dimension of corresponding vector $\boldsymbol{a}_i$) with the all elements on the diagonal equal to correspondent element d_{ij} of matrix $\mathbf{D}$, i.e.:

$$\mathbf{I}_{\mathrm{d}_{ij}} = d_{ij}\, \mathbf{I}_{(N_\mathrm{a} \times N_\mathrm{a})}. \tag{A5}$$

The definition of $\mathbf{\Omega}_\mathrm{inter}$ can rather easily generalized on situations with larger number of pixels. For example, for the case similar to above but for $N_x = N_y = N_t = 3$, the Eq. (A3) are transformed to the followings:

$$\mathbf{S}_x^T\,\mathbf{S}_x = \begin{pmatrix} \begin{pmatrix} \mathbf{D} & 0 & 0 \\ 0 & \mathbf{D} & 0 \\ 0 & 0 & \mathbf{D} \end{pmatrix} & \begin{pmatrix} 0 & 0 & 0 \\ 0 & 0 & 0 \\ 0 & 0 & 0 \end{pmatrix} & \begin{pmatrix} 0 & 0 & 0 \\ 0 & 0 & 0 \\ 0 & 0 & 0 \end{pmatrix} \\ \begin{pmatrix} 0 & 0 & 0 \\ 0 & 0 & 0 \\ 0 & 0 & 0 \end{pmatrix} & \begin{pmatrix} \mathbf{D} & 0 & 0 \\ 0 & \mathbf{D} & 0 \\ 0 & 0 & \mathbf{D} \end{pmatrix} & \begin{pmatrix} 0 & 0 & 0 \\ 0 & 0 & 0 \\ 0 & 0 & 0 \end{pmatrix} \\ \begin{pmatrix} 0 & 0 & 0 \\ 0 & 0 & 0 \\ 0 & 0 & 0 \end{pmatrix} & \begin{pmatrix} 0 & 0 & 0 \\ 0 & 0 & 0 \\ 0 & 0 & 0 \end{pmatrix} & \begin{pmatrix} \mathbf{D} & 0 & 0 \\ 0 & \mathbf{D} & 0 \\ 0 & 0 & \mathbf{D} \end{pmatrix} \end{pmatrix}; \mathbf{S}_y^T\,\mathbf{S}_y = \begin{pmatrix} \begin{pmatrix} \mathbf{I}_{\mathrm{d}_{11}} & \mathbf{I}_{\mathrm{d}_{12}} & \mathbf{I}_{\mathrm{d}_{13}} \\ \mathbf{I}_{\mathrm{d}_{21}} & \mathbf{I}_{\mathrm{d}_{22}} & \mathbf{I}_{\mathrm{d}_{23}} \\ \mathbf{I}_{\mathrm{d}_{31}} & \mathbf{I}_{\mathrm{d}_{32}} & \mathbf{I}_{\mathrm{d}_{33}} \end{pmatrix} & \begin{pmatrix} 0 & 0 & 0 \\ 0 & 0 & 0 \\ 0 & 0 & 0 \end{pmatrix} & \begin{pmatrix} 0 & 0 & 0 \\ 0 & 0 & 0 \\ 0 & 0 & 0 \end{pmatrix} \\ \begin{pmatrix} 0 & 0 & 0 \\ 0 & 0 & 0 \\ 0 & 0 & 0 \end{pmatrix} & \begin{pmatrix} \mathbf{I}_{\mathrm{d}_{11}} & \mathbf{I}_{\mathrm{d}_{12}} & \mathbf{I}_{\mathrm{d}_{13}} \\ \mathbf{I}_{\mathrm{d}_{21}} & \mathbf{I}_{\mathrm{d}_{22}} & \mathbf{I}_{\mathrm{d}_{23}} \\ \mathbf{I}_{\mathrm{d}_{31}} & \mathbf{I}_{\mathrm{d}_{32}} & \mathbf{I}_{\mathrm{d}_{33}} \end{pmatrix} & \begin{pmatrix} 0 & 0 & 0 \\ 0 & 0 & 0 \\ 0 & 0 & 0 \end{pmatrix} \\ \begin{pmatrix} 0 & 0 & 0 \\ 0 & 0 & 0 \\ 0 & 0 & 0 \end{pmatrix} & \begin{pmatrix} 0 & 0 & 0 \\ 0 & 0 & 0 \\ 0 & 0 & 0 \end{pmatrix} & \begin{pmatrix} \mathbf{I}_{\mathrm{d}_{11}} & \mathbf{I}_{\mathrm{d}_{12}} & \mathbf{I}_{\mathrm{d}_{13}} \\ \mathbf{I}_{\mathrm{d}_{21}} & \mathbf{I}_{\mathrm{d}_{22}} & \mathbf{I}_{\mathrm{d}_{23}} \\ \mathbf{I}_{\mathrm{d}_{31}} & \mathbf{I}_{\mathrm{d}_{32}} & \mathbf{I}_{\mathrm{d}_{33}} \end{pmatrix} \end{pmatrix}; \tag{A6}$$

$$\mathbf{S}_t^T\,\mathbf{S}_t = \begin{pmatrix} \begin{pmatrix} \mathbf{I}_{\mathrm{d}_{11}} & 0 & 0 \\ 0 & \mathbf{I}_{\mathrm{d}_{11}} & 0 \\ 0 & 0 & \mathbf{I}_{\mathrm{d}_{11}} \end{pmatrix} & \begin{pmatrix} \mathbf{I}_{\mathrm{d}_{12}} & 0 & 0 \\ 0 & \mathbf{I}_{\mathrm{d}_{12}} & 0 \\ 0 & 0 & \mathbf{I}_{\mathrm{d}_{12}} \end{pmatrix} & \begin{pmatrix} \mathbf{I}_{\mathrm{d}_{13}} & 0 & 0 \\ 0 & \mathbf{I}_{\mathrm{d}_{13}} & 0 \\ 0 & 0 & \mathbf{I}_{\mathrm{d}_{13}} \end{pmatrix} \\ \begin{pmatrix} \mathbf{I}_{\mathrm{d}_{21}} & 0 & 0 \\ 0 & \mathbf{I}_{\mathrm{d}_{21}} & 0 \\ 0 & 0 & \mathbf{I}_{\mathrm{d}_{21}} \end{pmatrix} & \begin{pmatrix} \mathbf{I}_{\mathrm{d}_{22}} & 0 & 0 \\ 0 & \mathbf{I}_{\mathrm{d}_{22}} & 0 \\ 0 & 0 & \mathbf{I}_{\mathrm{d}_{22}} \end{pmatrix} & \begin{pmatrix} \mathbf{I}_{\mathrm{d}_{23}} & 0 & 0 \\ 0 & \mathbf{I}_{\mathrm{d}_{23}} & 0 \\ 0 & 0 & \mathbf{I}_{\mathrm{d}_{23}} \end{pmatrix} \\ \begin{pmatrix} \mathbf{I}_{\mathrm{d}_{31}} & 0 & 0 \\ 0 & \mathbf{I}_{\mathrm{d}_{31}} & 0 \\ 0 & 0 & \mathbf{I}_{\mathrm{d}_{31}} \end{pmatrix} & \begin{pmatrix} \mathbf{I}_{\mathrm{d}_{32}} & 0 & 0 \\ 0 & \mathbf{I}_{\mathrm{d}_{32}} & 0 \\ 0 & 0 & I_{\mathrm{d}_{32}} \end{pmatrix} & \begin{pmatrix} \mathbf{I}_{\mathrm{d}_{33}} & 0 & 0 \\ 0 & \mathbf{I}_{\mathrm{d}_{33}} & 0 \\ 0 & 0 & \mathbf{I}_{\mathrm{d}_{33}} \end{pmatrix} \end{pmatrix}.$$

AMTD

3, 4967–5077, 2010

where the diagonal matrices $\mathbf{I}_{d_{ij}}$ are defined according to Eq. (A5) with the differences that the smoothness matrix $\mathbf{D}$ is generated on the base of matrix of first $\mathbf{S}_1$ or second differences $\mathbf{S}_2$ for $N_x = N_y = N_t = 3$ as:

$$\mathbf{D} = \mathbf{S}_1^T \mathbf{S}_1 = \begin{pmatrix} 1 & -1 & 0 \\ -1 & 2 & -1 \\ 0 & -1 & 1 \end{pmatrix}, \text{ or } \mathbf{D} = \mathbf{S}_2^T \mathbf{S}_2 = \begin{pmatrix} 1 & -2 & 1 \\ -2 & 4 & -2 \\ 1 & -2 & 1 \end{pmatrix}. \quad \text{(A7)}$$

The above two examples show clear pattern in defining the matrix $\mathbf{\Omega}_{\text{inter}}$ for $N_x = N_y = N_t = 2$ and 3 that can be easily generalized to the situation with higher dimensions. It can be observed from this pattern that $\mathbf{\Omega}_{\text{inter}}$ always retains the spare array structure. Specifically, the dimension of the matrix $\mathbf{\Omega}_{\text{inter}}$ is:

$$\left(N_{\text{a}} \times N_x \times N_y \times N_t\right) \times \left(N_{\text{a}} \times N_x \times N_y \times N_t\right), \quad \text{(A8)}$$

while the number of non-zero elements does not exceed the following value:

$$\left(N_a \times N_x \times N_y \times N_t\right) \times (2 \times m + 1), \quad \text{(A9)}$$

where m is order of used differences/derivatives used for inter-pixel smoothing. Obviously, the value of Eq. (A9) is generally significantly smaller and the $\mathbf{\Omega}_{\text{inter}}$ is essentially sparse matrix.

It should be noted that all above formulations are given for idealized situation when $\Delta x_i = x_{i+1} - x_i = \text{const}$, $\Delta y_i = y_{i+1} - y_i = \text{const}$, $\Delta t_i = t_{i+1} - t_i = \text{const}$ and $N_x = N_y = N_t$. In reality, none of these conditions are assured and the algorithm should be enabled to handle the most general situation when $\Delta x_i \neq \Delta y_i \neq \Delta t_i \neq \text{const}$, as well as, $N_x \neq N_y \neq N_t$. In such general situation the above equations describing the matrix $\mathbf{\Omega}_{\text{inter}}$ loose some of simplicity and transparency. Nonetheless, the general sparse structure of the matrix $\mathbf{\Omega}_{\text{inter}}$ is always conserved. Also, even the equations loose some transparency, the realization of inter-pixel smoothness constraints $\mathbf{\Omega}_{\text{inter}}$ is always rather simple on the algorithmic level and the most general case has been realized in the algorithm described here.

AMTD
3, 4967–5077, 2010

Appendix B

Constraining multiple-pixel retrieval by available information in the neighborhood of inverted pixel group

If the values of $\boldsymbol{a}^*_{\mathrm{nbr}}$ – parameters a in the pixels neighboring with inverted pixel group are known, then the basic system Eq. (32) can be complemented by the additional equations:

$$\left\{\begin{array}{rcl} \boldsymbol{f}^* & = & \boldsymbol{f}(\boldsymbol{a}) + \Delta \boldsymbol{f} \\ \boldsymbol{O}^*_{x,y,t} & = & \mathbf{S}_{x,y,t}\,\boldsymbol{a} + \Delta(\Delta\,\boldsymbol{a}) \\ \boldsymbol{s}^*_{x,\mathrm{edge}} & = & \mathbf{S}_{x,\mathrm{edge}}\,\boldsymbol{a} + \Delta(\Delta_x \boldsymbol{a}) \\ \boldsymbol{s}^*_{y,\mathrm{edge}} & = & \mathbf{S}_{y,\mathrm{edge}}\,\boldsymbol{a} + \Delta\left(\Delta_y\,\boldsymbol{a}\right) \\ \boldsymbol{s}^*_{t,\mathrm{edge}} & = & \mathbf{S}_{t,\mathrm{edge}}\,\boldsymbol{a} + \Delta(\Delta_t\,\boldsymbol{a}) \end{array}\right. , \tag{B1}$$

where $\mathbf{S}_{x,\mathrm{edge}}$ $\mathbf{S}_{y,\mathrm{edge}}$ $\mathbf{S}_{t,\mathrm{edge}}$ are the matrices containing the coefficients defining the m-th finite differences of parameters $\boldsymbol{a}$ describing the properties the inverted pixels group with $\boldsymbol{a}^*_{\mathrm{nbr}}$. These matrices can be trivially derived from $\mathbf{S}_m$ matrices (e.g. shown by Eq. 25b). For example, in a simple case when $N_x = 3$, $N_y = 1$ and $N_t = 1$, one can write:

$$\begin{pmatrix} \boldsymbol{a}^*_{\mathrm{before}} \\ \boldsymbol{a} \\ \boldsymbol{a}^*_{\mathrm{after}} \end{pmatrix} = \begin{matrix} \begin{pmatrix} a\,(x_1;\,y_1;\,t_1) \\ a\,(x_2;\,y_1;\,t_1) \\ a\,(x_3;\,y_1;\,t_1) \end{pmatrix} \\ \begin{pmatrix} a\,(x_4;\,y_1;\,t_1) \\ a\,(x_5;\,y_1;\,t_1) \\ a\,(x_6;\,y_1;\,t_1) \end{pmatrix} \\ \begin{pmatrix} a\,(x_7;\,y_1;\,t_1) \\ a\,(x_8;\,y_1;\,t_1) \\ a\,(x_9;\,y_1;\,t_1) \end{pmatrix} \end{matrix} = \begin{matrix} \begin{pmatrix} a^*_1 \\ a^*_2 \\ a^*_3 \end{pmatrix} \\ \begin{pmatrix} a_4 \\ a_5 \\ a_6 \end{pmatrix} \\ \begin{pmatrix} a^*_7 \\ a^*_8 \\ a^*_9 \end{pmatrix} \end{matrix} . \tag{B2}$$

AMTD

3, 4967–5077, 2010

Statistically optimized inversion algorithm for enhanced retrieval

O. Dubovik et al.

If Eq. (B1) uses second differences and continuity with $\boldsymbol{a}^*_{\text{before}}$ can be expressed using the following formulations:

$$\begin{cases} 0^*_1 = a^*_2 - 2\,a^*_3 + a_4 + \Delta_1 \\ 0^*_2 = a^*_3 - 2\,a_4 + a_5 + \Delta_2 \end{cases}. \tag{B3}$$

In matrix form this equation can be expressed as:

$$\begin{pmatrix} 0^*_1 \\ 0^*_2 \end{pmatrix} = \begin{pmatrix} 0 & 1 & -2 & 1 & 0 & 0 \\ 0 & 0 & 1 & -2 & 1 & 0 \end{pmatrix} \begin{pmatrix} \boldsymbol{a}^*_{\text{before}} \\ \boldsymbol{a} \end{pmatrix} + \begin{pmatrix} \Delta_1 \\ \Delta_2 \end{pmatrix} \quad . \tag{B4}$$

Then it can be transformed as

$$\begin{pmatrix} 0^*_1 \\ 0^*_2 \end{pmatrix} = \begin{pmatrix} 0 & 1 & -2 \\ 0 & 0 & 1 \end{pmatrix} \boldsymbol{a}^*_{\text{before}} + \begin{pmatrix} 1 & 0 & 0 \\ -2 & 1 & 0 \end{pmatrix} \boldsymbol{a} + \begin{pmatrix} \Delta_1 \\ \Delta_2 \end{pmatrix}. \tag{B5}$$

Then one can write:

$$\boldsymbol{s}^*_{x,b} = \mathbf{S}_{x,b}\,\boldsymbol{a} + \Delta\,(\Delta_x\,\boldsymbol{a}), \tag{B6}$$

where

$$\boldsymbol{s}^*_{x,b} = -\begin{pmatrix} 0 & 1 & -2 \\ 0 & 0 & 1 \end{pmatrix} \boldsymbol{a}^*_{\text{before}} \text{ and } \mathbf{S}_{x,b} = \begin{pmatrix} 1 & 0 & 0 \\ -2 & 1 & 0 \end{pmatrix}. \tag{B7}$$

Analogously, and continuity with $\boldsymbol{a}^*_{\text{after}}$ can be expressed as follows:

$$\begin{cases} 0^*_3 = a_5 - 2\,a_6 + a^*_7 + \Delta_3 \\ 0^*_4 = a_6 - 2\,a^*_7 + a^*_8 + \Delta_4 \end{cases} \tag{B8}$$

In matrix form this equation can be expressed as:

$$\begin{pmatrix} 0^*_3 \\ 0^*_4 \end{pmatrix} = \begin{pmatrix} 0 & 1 & -2 & 1 & 0 & 0 \\ 0 & 0 & 1 & -2 & 1 & 0 \end{pmatrix} \begin{pmatrix} \boldsymbol{a} \\ \boldsymbol{a}^*_{\text{after}} \end{pmatrix} + \begin{pmatrix} \Delta_3 \\ \Delta_4 \end{pmatrix}. \tag{B9}$$

Then it can be transformed as

$$\begin{pmatrix} 0^*_3 \\ 0^*_4 \end{pmatrix} = \begin{pmatrix} 0 & 1 & -2 \\ 0 & 0 & 1 \end{pmatrix} \boldsymbol{a} + \begin{pmatrix} 1 & 0 & 0 \\ -2 & 1 & 0 \end{pmatrix} \boldsymbol{a}^*_{\text{after}} + \begin{pmatrix} \Delta_3 \\ \Delta_4 \end{pmatrix}. \tag{B10}$$

Discussion Paper | Discussion Paper | Discussion Paper | Discussion Paper |

AMTD

3, 4967–5077, 2010

Then one can write:

$$s^*_{x,\mathrm{a}} = \mathbf{S}_{x,\mathrm{a}} + \Delta\left(\Delta_x\, \boldsymbol{a}\right), \tag{B11}$$

where

$$\mathbf{S}_{x,\mathrm{a}} = \begin{pmatrix} 1 & 0 & 0 \\ -2 & 1 & 0 \end{pmatrix} \text{ and } \boldsymbol{s}^*_{x,\mathrm{a}} = -\begin{pmatrix} 0 & 1 & -2 \\ 0 & 0 & 1 \end{pmatrix} \boldsymbol{a}^*_{\mathrm{after}} \tag{B12}$$

Finally, the using Eqs. (31) and (33) can define $\boldsymbol{s}^*_{x,\mathrm{edge}}$ and $\mathbf{S}_{x,\mathrm{edge}}$ used in Eq. (B1) as follows:

$$\boldsymbol{s}^*_{x,\mathrm{edge}} = \begin{pmatrix} \boldsymbol{s}^*_{x,\mathrm{b}} \\ \boldsymbol{s}^*_{x,\mathrm{a}} \end{pmatrix} \text{ and } \mathbf{S}_{x,\mathrm{edge}} = \begin{pmatrix} \mathbf{S}_{x,\mathrm{b}} \\ \mathbf{S}^*_{x,\mathrm{a}} \end{pmatrix}. \tag{B13}$$

Thus, the derivations shown by Eqs. (B1)–(B11) showed the principle of defining the constraints enforcing the continuity of retrieved properties with the those obtained for the pixels neighboring with inverted pixel group. Analogously the constraints can be included for continuity over coordinates y and t. In general case of large inverted pixel group one can use rather large number equations similar to those of Eqs. (B3) and (B8). The maximum number of such edge continuity equations can be estimated as:

$$N_\mathrm{a} \times \left(N_x \times N_y + N_x \times N_t + N_y \times N_t\right) \times (2 \times m), \tag{B14}$$

where m is order of used differences/derivatives used for inter-pixel smoothing.

Based on the added equations as shown in Eq. (B1), the constraining of the multi-pixel system solution by additional condition of continuity of aerosol and surface properties with values in the neighborhood of the inverted pixel group can be implemented by adding extra terms in the Eq. (20). The minimized quadratic form $\Psi(\boldsymbol{a}^\mathrm{p})$, its gradient $\nabla\Psi(\boldsymbol{a}^\mathrm{p})$ and Fisher Matrix $\mathbf{A}_\mathrm{p}$ formulated for inversion of combined multi-pixel Eq. (26) should modified as follows:

$$\Psi\left(\boldsymbol{a}^\mathrm{p}\right) = \left(\sum_{i=1}^{N_\mathrm{pixels}} \Psi_i\left(\boldsymbol{a}^\mathrm{p}\right)\right) + \left(\boldsymbol{a}^\mathrm{p}\right)^T \boldsymbol{\Omega}_\mathrm{inter}\, \boldsymbol{a}^\mathrm{p} + \Psi_\mathrm{edge}\left(\boldsymbol{a}^\mathrm{p}\right) \tag{B15}$$

AMTD
3, 4967–5077, 2010

where

$$\Psi_{\text{edge}}\left(\boldsymbol{a}^{\text{p}}\right) = \left(\mathbf{S}_{\text{edge}}\,\boldsymbol{a}^{\text{p}} - \boldsymbol{s}^{*}_{\text{edge}}\right)^{T}\left(\mathbf{S}_{\text{edge}}\,\boldsymbol{a}^{\text{p}} - \boldsymbol{s}^{*}_{\text{edge}}\right), \tag{B16}$$

$$\mathbf{S}_{\text{edge}} = \begin{pmatrix} \gamma_x^{1/2}\,\mathbf{S}_{x,\text{edge}} \\ \gamma_y^{1/2}\,\mathbf{S}_{y,\text{edge}} \\ \gamma_t^{1/2}\,\mathbf{S}_{t,\text{edge}} \end{pmatrix} \text{ and } \boldsymbol{s}^{*}_{\text{edge}} = \begin{pmatrix} \gamma_x^{1/2}\,\boldsymbol{s}_{x,\text{edge}} \\ \gamma_y^{1/2}\,\boldsymbol{s}_{y,\text{edge}} \\ \gamma_t^{1/2}\,\boldsymbol{s}_{t,\text{edge}} \end{pmatrix}. \tag{B17}$$

The *Fisher Matrix* $\mathbf{A}_{\text{p}}$ is modified as:

$$\mathbf{A}_{\text{p}} = \left[\begin{pmatrix} \mathbf{A}_{1,\text{p}} & \mathbf{0} & \dots & \mathbf{0} \\ \mathbf{0} & \mathbf{A}_{2,\text{p}} & \dots & \mathbf{0} \\ \dots & \dots & \dots & \dots \\ \mathbf{0} & \mathbf{0} & \dots & \mathbf{A}_{N,\text{p}} \end{pmatrix} + \boldsymbol{\Omega}_{\text{inter}} + \boldsymbol{\Omega}_{\text{edge}}\right], \tag{B18}$$

where $\boldsymbol{\Omega}_{\text{edge}}$ is equal to the edge smoothing inter-pixel matrix determined as

$$\boldsymbol{\Omega}_{\text{edge}} = \mathbf{S}^{T}_{x,\text{edge}}\,\mathbf{S}_{x,\text{edge}} + \mathbf{S}^{T}_{y,\text{edge}}\,\mathbf{S}_{y,\text{edge}} + \mathbf{S}^{T}_{t,\text{edge}}\,\mathbf{S}_{t,\text{edge}}. \tag{B19}$$

and the gradient $\nabla\Psi(\boldsymbol{a}^{\text{p}})$ will be:

$$\nabla\Psi\left(\boldsymbol{a}^{\text{p}}\right) = \begin{bmatrix} \nabla\Psi_1\left(\boldsymbol{a}^{\text{p}}_1\right) \\ \nabla\Psi_2\left(\boldsymbol{a}^{\text{p}}_2\right) \\ \dots \\ \nabla\Psi_N\left(\boldsymbol{a}^{\text{p}}_N\right) \end{bmatrix} + \boldsymbol{\Omega}_{\text{inter}}\,\boldsymbol{a}^{\text{p}} + \nabla\Psi_{\text{edge}}\left(\boldsymbol{a}^{\text{p}}\right), \tag{B20}$$

where

$$\nabla\Psi_{\text{edge}}\left(\boldsymbol{a}^{\text{p}}\right) = \mathbf{S}^{T}_{\text{edge}}\left(\mathbf{S}_{\text{edge}}\,\boldsymbol{a}^{\text{p}} - \boldsymbol{s}^{*}_{\text{edge}}\right). \tag{B21}$$

AMTD
3, 4967–5077, 2010

It should be noted that the illustrative derivations shown by Eqs. (B3–B12) are given for idealized situation when $\Delta x_i = x_{i+1} - x_i$ =const and $N_y = N_t = 1$. In reality, the edge continuity can be applied over all three coordinates x, y, t and the algorithm should be enabled to handle the most general situation when $\Delta x_i \neq \Delta y_i \neq \Delta t_i \neq$ const, as well as, $N_x \neq N_y \neq N_t$. In such general situation the above equations describing the matrix $\mathbf{\Omega}_{\text{edge}}$ loose the simplicity and transparency. Nonetheless, the general sparse structure of the matrix $\mathbf{\Omega}_{\text{edge}}$ is always conserved. Also, even the equations loose some transparency, the realization of inter-pixel smoothness edge constraints $\mathbf{\Omega}_{\text{edge}}$ is always rather simple on the algorithmic level and it takes negligible computer time to implement.

The values of Lagrange parameters γ_x, γ_y and γ_t used for applying the "edge" inter-pixel constraints are exactly the same as those used in Sect. 4.2.1 describing inter-pixel smoothness constraints application in the simultaneous inversion of a group of pixels.

Appendix C

Assumption of inter-pixels constant parameters in the retrieval

The general idea of this technique of imposing an extra assumption of equal parameters can be illustrated using the following simple illustration. Assuming, Eq. (17) is represented by the following simple system:

$$\mathbf{U}\,\boldsymbol{a} = \boldsymbol{f}^* + \Delta\,\boldsymbol{f}, \tag{C1}$$

Then the correspondent *Normal system* $\mathbf{A}\boldsymbol{a} = \nabla\Psi(\boldsymbol{a})$ is defined as

$$\mathbf{U}^T\,\mathbf{U}\,\boldsymbol{a} = \mathbf{U}^T\,\boldsymbol{f}^*. \tag{C2}$$

If two parameters a_1 and a_2 are retrieved from single observation f_1^*, the one can write:

$$\mathbf{U} = \begin{pmatrix} u_1 & u_2 \end{pmatrix}; \boldsymbol{f}^* = \begin{pmatrix} f_1^* \end{pmatrix};\ \boldsymbol{a} = \begin{pmatrix} a_1 \\ a_2 \end{pmatrix}. \tag{C3}$$

AMTD
3, 4967–5077, 2010

For such situation the *Fisher matrix* **A** and *gradient* $\nabla\Psi(\boldsymbol{a})$ are

$$\mathbf{A}^{(2)} = \mathbf{U}^T\,\mathbf{U} = \begin{pmatrix} u_1^2 & u_1\,u_2 \\ u_2\,u_1 & u_2^2 \end{pmatrix};\ \nabla\,\Psi^{(2)} = \mathbf{U}^T\,\boldsymbol{f}^* = \begin{pmatrix} u_1\,f_1^* \\ u_2\,f_1^* \end{pmatrix}. \tag{C4}$$

If only it is assumed $a_1 = a_2$ and only one parameter retrieved then the definitions given by Eq. (C3) should be replaced by:

$$\mathbf{U} = (u_1 + u_2);\ \boldsymbol{f}^* = (f_1^*);\ \boldsymbol{a} = (a_1). \tag{C5}$$

Correspondingly, the the *Fisher matrix* **A** and *gradient* $\nabla\Psi(\boldsymbol{a})$ become the followings:

$$\mathbf{A}^{(1)} = \mathbf{U}^T\,\mathbf{U} = (u_1 + u_2)^2;\ \nabla\,\Psi^{(1)} = \mathbf{U}^T\,\boldsymbol{f}^* = (u_1 + u_2)\,f_1^*. \tag{C6}$$

Comparing Eqs. (C4) and (C5) one can note the following trivial relation between $\mathbf{A}^{(1)}$, $\nabla\Psi^{(1)}$ and $\mathbf{A}^{(2)}$, $\nabla\Psi^{(2)}$:

$$\mathbf{A}^{(1)} = \left(\mathbf{A}_{11}^{(2)} + \mathbf{A}_{21}^{(2)}\right) + \left(\mathbf{A}_{11}^{(2)} + \mathbf{A}_{12}^{(2)}\right);\ \nabla\,\Psi^{(1)} = \nabla\,\Psi_1^{(2)} + \nabla\,\Psi_2^{(2)}. \tag{C7}$$

These relationships can be easily generalized. Let assume one has defined Fisher matrix $\mathbf{A}^{(N)}$ and gradient $\nabla\Psi^{(N)}$ for deriving N parameters a_i. Then it was decided that $n+1$ represent the same single parameter, i.e. $a_i = a_{i_k}$ $(k = 1, \ldots, n+1)$. In this situation, the new Fisher matrix $\mathbf{A}^{(N-n)}$ and gradient $\nabla\Psi^{(N-n)}$ can be obtained as follows:

$$\mathbf{A}_{m,N-n}^{(N-n)} = \mathbf{A}_{N-n,m}^{(N-n)} = \sum_{k=1,\ldots,n} \mathbf{A}_{i_k m}^{(N)}\ -\ \text{non}-\text{diagonal elements}, \tag{C8}$$

$$\mathbf{A}_{N-n,N-n}^{(N-n)} = \sum_{p=1,\ldots,n} \left(\sum_{k=1,\ldots,n} \mathbf{A}_{i_k j_p}^{(N)} \right) - \text{diagonal elements}, \tag{C9}$$

$$\nabla\,\Psi^{(N-n)} = \sum_{k=1,\ldots,n} \nabla\,\Psi_{i_k}^{(N)}. \tag{C10}$$

AMTD
3, 4967–5077, 2010

Statistically optimized inversion algorithm for enhanced retrieval

O. Dubovik et al.

The resulting matrix $\mathbf{A}^{(N-n)}$ has reduced dimension $(N-n)\times(N-n)$.

Thus, Eqs. (C7–C9) allow significant flexibility in designing the retrieval. The option is fully implemented in the present retrieval algorithm.

Acknowledgements. PARASOL/POLDER is the second microsatellite in the Myriade series developed by the French Space Agency (CNES). The authors thank the ICARE Data and Services Center for providing access to the PARASOL data and for general assistance and development support. This research has been supported by CNES, CNRS, the University of Lille, and Region Nord-Pas-de-Calais. Finally, the authors are very thankful to AERONET and PHOTONS for establishing and maintaining the sites used in this work. The publication of this article is financed by CNRS-INSU.

The publication of this article is financed by CNRS-INSU.

References

Carrer, D., Roujean, J. L., Hautecoeur, O., and Elias, T.: Daily estimates of aerosol optical thickness over land surface based on a directional and temporal analysis of SEVIRI MSG visible observations, J. Geophys. Res., 115, D10208, doi:10.1029/2009JD012272, 2010.

Cattrall, C., Reagan, J., Thome, K., and Dubovik, O.: Variability of aerosol lidar, backscatter and extinction ratios of key aerosol types derived from selected AERONET locations, J. Geophys. Res., 110, D10S11, doi:10.1029/2004JD005124, 2005.

Chowdhary, J., Cairns, B., and Travis, L. D.: Case studies of aerosol Retrievals over the ocean from multiangle, multispectral photopolarimetric remote sensing data, J. Atmos. Sci., 59, 383–397, 2002.

Chowdhary, J., Cairns, B., Mishchenko, M. I., Hobbs, P. V., Cota, G. F., Redemann, J., Rutledge, K., Holben, B. N., and Russell, E.: Retrieval of aerosol scattering and absorption properties from photopolarimetric observations over the ocean during the CLAMS experiment, J. Atmos. Sci., 62, 1093–1117, 2005.

Cox, C. and Munk, W.: Measurements of the roughness of the sea surface from photographs of the Sun's glitter, J. Opt. Soc. Am., 44, 838–850, 1954.

Derimian, Y., Leon, J.-F., Dubovik, O., Chiapello, I., Tanré, D., Sinyuk, A., Auriol, F., Podvin, T., Brogniez, G., and Holben, B. N.: Radiative properties of aerosol mixture observed during the dry season 2006 over M'Bour, Senegal (African Monsoon Multidisciplinary Analysis campaign), J. Geophys. Res., 113, D00C09, doi:10.1029/2008JD009904, 2008.

Deschamps, P. Y., Bréìon, F. M., Leroy, M., Podaire, A., Bricaud, A., Buriez, J. C., and Seze, G.: The POLDER mission: Instrument charac- teristics and scientific objectives, IEEE T. Geosci. Remote, 32, 598–615,1994.

Deuzé, J. L., Bréon, F. M., Devaux, C., Goloub, P., Herman, M., Lafrance, B., Maignan, F., Marchand, A., Perry, G., and Tanré, D.: Remote Sensing of aerosols over land surfaces from POLDER/ADEOS-1 polarized measurements, J. Geophys. Res., 106, 4913–4926, 2001.

Diner, D. J., Beckert, J. C., Reilly, T. H., Bruegge, C. J., Conel, J. E., Kahn, R. A., Martonchik, J. V., Ackerman, T. P., Davies, R., Gerstl, S. A. W., Gordon, H. R., Muller, J. P., Myneni, R. B., Sellers, P. J., Pinty, B., and Verstraete, M. M.: Multi-angle Imaging SpectroRadiometer (MISR) - Instrument description and experiment overview, IEEE T. Geosci. Remote, 36, 1072–1087, 1998.

Diner, D. J., Braswell, B. H., Davies, R., Gobron, N., Hu, J. N., Jin, Y. F., Kahn, R. A., Knyazikhin, Y., Loeb, N., Muller, J. P., Nolin, A. W., Pinty, B., Schaaf, C. B., Seiz, G., and Stroeve, J.: The value of multiangle measurements for retrieving structurally and radiatively consistent properties of clouds, aerosols, and surfaces, Remote Sens. Environ., 97, 495–518, 2005.

Dubovik, O., Smirnov, A., Holben, B. N., King, M. D., Kaufman, Y. J., Eck, T. F., and Slutsker, I.: Accuracy assessment of aerosol optical properties retrieval from AERONET sun and sky radiance measurements, J. Geophys. Res., 105, 9791–9806, 2000.

Dubovik, O. and King, M. D.: A flexible inversion algorithm for retrieval of aerosol optical properties from Sun and sky radiance measurements, J. Geophys. Res., 105, 20673–20696, 2000.

Dubovik, O., Holben, B. N., Eck, T. F., Smirnov, A., Kaufman, Y. J., King, M. D., Tanré, D., and Slutsker, I.: Variability of absorption and optical properties of key aerosol types observed in worldwide locations, J. Atmos. Sci., 59, 590–608, 2002a.

Dubovik, O., Holben, B. N., Lapyonok, T., Sinyuk, A., Mishchenko, M. I., Yang, P., and Slutsker, I.: Non-spherical aerosol retrieval method employing light scattering by spheroids, Geophys. Res. Lett., 29, 1415, doi:10.1029/2001GL014506, 2002b.

Dubovik, O.: Optimization of Numerical Inversion in Photopolarimetric Remote Sensing, in: Photopolarimetry in Remote Sensing, edited by: Videen, G., Yatskiv, Y., and Mishchenko, M., Kluwer Academic Publishers, Dordrecht, The Netherlands, 65–106, 2004.

Dubovik, O., Sinyuk, A., Lapyonok, T., Holben, B. N., Mishchenko, M., Yang, P., Eck, T. F., Volten, H., Munoz, O., Veihelmann, B., van der Zander, W. J., Sorokin, M., and Slutsker, I.: Application of light scattering by spheroids for accounting for particle non-sphericity in remote sensing of desert dust, J. Geophys. Res., 111, D11208, doi:10.1029/2005JD006619d, 2006.

Dubovik, O., Lapyonok, T., Kaufman, Y. J., Chin, M., Ginoux, P., Kahn, R. A., and Sinyuk, A.: Retrieving global aerosol sources from satellites using inverse modeling, Atmos. Chem. Phys., 8, 209–250, doi:10.5194/acp-8-209-2008, 2008.

Eck, T. F., Holben, B. N., Ward, D. E., Mukelabai, M. M., Dubovik, O., Smirnov, A., Schafer, J. S., Hsu, N. C., Piketh, S. J., Queface, A., Le Roux, J., Swap, S. J., and Slutsker, I.: Variability of biomass burning aerosol optical characteristics in southern Africa during the SAFARI 2000 dry season campaign and a comparison of single scattering albedo estimates from radiometric measurements, J. Geophys. Res., 108, 8477, doi:10.1029/2002JD002321, 2003.

Eck, T. F., Holben, B. N., Dubovik, O., Smirnov, A., Gouloub, P., Chen, H. B., Chatenet, B., Gomes, L., Zhang, X.-Y., Tsay, S.-C., Ji, Q., Giles, D., and Slutsker, I.: Columnar aerosol optical properties at AERONET sites in Central-eastern Asia and aero-sol transport to the tropical mid Pacific, J. Geophys. Res., 110, D06202, doi:10.1029/2004JD005274, 2005.

Formenti, P., Rajot, J. L., Desboeufs, K., Caquineau, S., Chevaillier, S., Nava, S., Gaudichet, A., Journet, E., Triquet, S., Alfaro, M., Haywood, J., Coe, H., and Highwood, E.: Regional variability of the composition of mineral dust from western Africa: Results from the AMMA SOP0/DABEX and DODO field campaigns, J. Geophys Res., 113, D00C13, doi:10.1029/2008JD009903, 2008.

AMTD
3, 4967–5077, 2010

Statistically optimized inversion algorithm for enhanced retrieval

O. Dubovik et al.

García, O. E., Díaz, A. M., Exposito, F. J., Díaz, J. P., Dubovik, O., Dubuisson, P., Roger, J.-C., Eck, T. F., Sinyuk, A., Derimian, Y., Dutton, E. G., Schafer, J. S., Holben, B. N., and García, C. A.: Validation of AERONET estimates of atmospheric solar fluxes and aerosol radiative forcing by ground-based broadband measurements, J. Geophys. Res., 113, D21207, doi:10.1029/2008JD010211, 2008.

Gatebe, C. K., Dubovik, O., King, M. D., and Sinyuk, A.: Simultaneous retrieval of aerosol and surface optical properties from combined airborne- and ground-based direct and diffuse radiometric measurements, Atmos. Chem. Phys., 10, 2777–2794, doi:10.5194/acp-10-2777-2010, 2010.

Gérard, B., Déuze, J. L., Herman, M., Kaufman, Y. J., Lallart, P., Oudard, C., Remer, L. A., Roger, B., Six, B., and Tanré, D.: Comparisons between POLDER 2 and MODIS/Terra aerosol retrievals over ocean, J. Geophys. Res., 110, D24211, doi:10.1029/2005JD006218, 2005.

Govaerts, Y. M., Wagner, S., Lattanzio, A., and Watts, P.: MSG/SEVIRI observations with an optimal estimation approach: 1. Theory, J. Geophys. Res., 111, D02203, doi:10.1029/2009JD011779, 2010.

Hansen, J. E.: Multiple scattering of polarized ling in planetary atmospheresm Part 2: Sunlight reflected by terrestrial water clouds, J. Atmos. Sci., 28(8), 1400–1426, 1971.

Hasekamp, O. P. and Landgraf, J.: Linearization of vector radiative transfer with respect to aerosol properties and its use in satellite remote sensing, J. Geophys. Res., 110, D04203, doi:10.1029/2004JD005260, 2005a.

Hasekamp, O. P. and Landgraf, J.: Retrieval of aerosol properties over the ocean from multispectral single-viewing-angle measurements of intensity and polarization: Retrieval approach, information content, and sensitivity study, J. Geophys. Res., 110 , D20207, doi:10.1029/2005JD006212, 2005b.

Hasekamp, O. P. and Landgraf, J.: Retrieval of aerosol properties over land surfaces: capabilities of multiple-viewing-angle intensity and polarization measurements, Appl. Optics, 46 , 3332–3344, 2007.

Haywood, J. M., Francis, P., Dubovik, O., Glew, M., and Holben, B. N.: Comparison of aerosol size distributions, radiative properties and optical depths determined by aircraft observations and sunphotometers during SAFARI-2000, J. Geophys. Res., 108, 8471, doi:10.1029/2002JD002250, 2003.

Herman, M., Deuzé, J.-L., Marchant, A., Roger, B., and Lallart, P.: Aerosol remote sensing from POLDER/ADEOS over the ocean: Improved retrieval using a nonspherical particle model, J. Geophys. Res., 110, D10S02, doi:10.1029/2004JD004798, 2005.
Higurashi, A. and Nakajima, T.: Development of a two-channel aerosol retrieval algorithm on a global scale using NOAA AVHRR, J. Atmos. Sci., 56, 924–941, 1999.
Holben, B. N., Eck, T. F., Slutsker, I., et al.: AERONET – A federated instrument network and data archive for aerosol characterization, Remote Sens. Environ., 66, 1–16, 1998.
Holben, B. N., Tanré, D., Smirnov, A., et al.: An emerging ground-based aerosol climatology: Aerosol optical depth from AERONET, J. Geophys. Res., 106, 12067–12097, 2001.
Johnson, B. T., Christopher, S., Haywood, J. M., Osborne, S. R., McFarlane, S., Hsu, C., Salustro, C., and Kahn, R.: Measurements of aerosol properties from aircraft, satellite and ground-based remote sensing: A case-study from the Dust and Biomass-burning Experiment (DABEX), Q. J. Roy. Meteor. Soc., 135, 922–934, 2009.
Justice, C. O., Vermote, E., Townshend, J. R. G., Defries, R., Roy, D. P., Hall, D. K., Salomonson, V. V., Privette, J. L., Riggs, G., Strahler, A., Lucht, W., Myneni, R. B., Knyazikhin, Y., Running, S. W., Nemani, R. R., Wan, Z. M., Huete, A. R., van Leeuwen, W., Wolfe, R. E., Giglio, L., Muller, J. P., Lewis, P., and Barnsley, M. J.: The Moderate Resolution Imaging Spectroradiometer (MODIS): Land remote sensing for global change research, IEEE T. Geosci. Remote, 36, 1228–1249, 1998.
Kahn, R. A., Gaitley, B. J., Martonchik, J. V., Diner, D. J., Crean, K. A., and Holben, B. N.: Multiangle Imaging Spectroradiometer (MISR) global aerosol optical depth validation based on 2 years of coincident Aerosol Robotic Network (AERONET) observations, J. Geophys. Res., 110, D10S04, doi:10.1029/2004JD004706, 2005.
Kahn, R. A., Garay, M. J., Nelson, D. L., Yau, K. K., Bull, M. A., Gaitley, B. J., Martonchik, J. V., and Levy, R. C.: Satellite-derived aerosol optical depth over dark water from MISR and MODIS: Comparisons with AERONET and implications for climatological studies, J. Geophys. Res., 112, D18205, doi:10.1029/2006JD008175, 2007.
Kahn, R. A., Nelson, D. L., Garay, M. J., Levy, R. C., Bull, M. A., Diner, D. J., Martonchik, J. V., Paradise, S. R., Hansen, E. G., and Remer, L. A.: MISR aerosol product attributes, and statistical comparisons with MODIS, IEEE T. Geosci. Remote, 47, 4095–4114, 2009.
Kalashnikova, O. V., Kahn, R., Sokolik, I. N., and Li, W. H.: Ability of multiangle remote sensing observations to identify and distinguish mineral dust types: Optical models and retrievals of optically thick plumes, J. Geophys. Res., 110, D18S14, doi:10.1029/2004JD004550, 2005.

AMTD
3, 4967–5077, 2010

Kalashnikova, O. V. and Kahn, R.: Ability of multiangle remote sensing observations to identify and distinguish mineral dust types: 2. Sensitivity over dark water, J. Geophys. Res., 111, D11207, doi:10.1029/2005JD006756, 2006.

Kalman, R. E.: A New approach to linear filtering and prediction problems, J. Basic Eng., 82, 35–40, 1960.

Kaufman, Y. J., Tanré, D., Gordon, H. R., Nakajima, T., Lenoble, J., Frouin, R., Grassl, H., Herman, B. M., King, M., and Teillet, P. M.: Operational remote sensing of tropospheric aerosol over land from EOS moderate resolution imaging spectroradiometer, J. Geophys. Res., 102(D14), 17051–17067, 1997.

Kaufman, Y. J., Tanre, D., Dubovik, O., Karnieli, A., and Remer, L. A.: Absorption of sunlight by dust as inferred from satellite and ground-based remote sensing, Geophys. Res. Lett., 28, 1479–1483, 2001.

King, M. D., Byrne, D. M., Herman, B. M., and Reagan, J. A.: Aerosol size distributions obtained by inversion of spectral optical depth measurements, J. Atmos. Sci., 21, 2153–2167, 1978.

King, M. D.: Sensitivity of constrained linear inversions to the selection of the Lagrange multiplier, J. Atmos. Sci., 39, 1356–1369, 1982.

Kokhanovsky, A. A., Breon, F. M., Cacciari, A., Carboni, E., Diner, D., Di Nicolantonio, W., Grainger, R. G., Grey, W. M. F., Holler, R., Lee, K.-H., Li, Z., North, P. R. J., Sayer, A. M., Thomas, G. E., and von Hoyningen-Huene, W.: Aerosol remote sensing over land: A comparison of satellite retrievals using different algorithms and instruments, Atmos. Res., 85, 372–394, 2007.

Kokhanovsky, A. A., Deuzé, J. L., Diner, D. J., Dubovik, O., Ducos, F., Emde, C., Garay, M. J., Grainger, R. G., Heckel, A., Herman, M., Katsev, I. L., Keller, J., Levy, R., North, P. R. J., Prikhach, A. S., Rozanov, V. V., Sayer, A. M., Ota, Y., Tanré, D., Thomas, G. E., and Zege, E. P.: The inter-comparison of major satellite aerosol retrieval algorithms using simulated intensity and polarization characteristics of reflected light, Atmos. Meas. Tech., 3, 909–932, doi:10.5194/amt-3-909-2010, 2010.

Lafon, S., Sokolik, I. N., Rajot, J.-L., Caquineau, S., and Gaudichet, A.: Characterization of iron oxides in mineral dust aerosols: Implications for light absorption, J. Geophys. Res., 111, D21207, doi:10.1029/2005JD007016, 2006.

Lenoble, J., Herman, M., Deuze, J. L., Lafrance, B., Santer, R., and Tanre, D.: A successive order of scattering code for solving the vector equation of transfer in the earth's atmosphere with aerosols, J. Quant. Sprectrosc. Ra., 107(3), 479–507, 2007.
Levy, R., Remer, L., and Dubovik, O.: Global aerosol optical models and applica-tion to MODIS aerosol retrieval over land, J. Geophys. Res., 112, D13210, doi:10.1029/2006JD007815, 2007a.
Levy, R. C., Remer, L. R., Mattoo, S., Vermote, E. F., and Kaufman, Y. J.: Second-generation operational algorithm: Retrieval of aerosol properties over land from inversion of Moderate Resolution Imaging Spectroradiometer spectral reflectance, J. Geophys. Res., 112, D13211, doi:10.1029/2006JD007811, 2007b.
Li, X. and Strahler, A. H.: Geometrical-optical bidirectional reflectance modeling of the discrete crown vegetation canopy: effect of crown shape and mutual shadowing. IEEE T. Geosci. Remote, 30, 276–292, 1992.
Li, Z., Goloub, P., Dubovik, O., Blarel, L., Zhang, W., Podvin, T., Sinyuk, A., Sorokin, M., Chen, H., Holben, B. N., Tanré, D., Canini, M., and Buis, J.-P.: Improvements for ground-based remote sensing of atmospheric aerosol properties by additional po-larimetric measurements, J. Quant. Spectrosc. Ra., 110, 1954–1961, 2009.
Litvinov, P., Hasekamp, O., Cairns, B., and Mishchenko, M.: Reflection models for soil and vegetation surfaces from multiple-viewing angle photopolarimetric measurements, J. Quant. Spectrosc. Ra., 111, 529–539, 2010a.
Litvinov, P., Hasekamp, O., and Mishchenko, M.: Models for surface reflection of radiance and polarized radiance: 2 comparison with airborne multi-angle photo-polarimetric 3 measure-ments and implications for modeling top-of-atmosphere measurements, Remote Sensing of Environment, in press, 2010b.
Liu, Y., Sarnat, J. A., Coull, B. A., Koutrakis, P., and Jacob, D. J.: Validation of multiangle imaging spectroradiometer (MISR) aerosol optical thickness measurements using aerosol robotic network (AERONET) observations over the contiguous United States, J. Geophys. Res., 109, D06205, doi:10.1029/2003JD003981, 2004.
Lyapustin, A., Wang, Y., Martonchik, J., Privette, J. L., Holben, B. N., Slutsker, I., Sinyuk, A., and Smirnov, A.: Local analysis of MISR surface BRF and albedo over GSFC and Mongu AERONET sites, IEEE T. Geosci. Remote, 44, 1707–1718, 2006.

Lyapustin, A., Wang, Y., and Frey, R.: An automatic cloud mask algorithm based on time series of MODIS measurements, J. Geophys. Res., 113, D16207, doi:10.1029/2007JD009641, 2008.

Lyapustin, A., and Wang, Y.: The Time Series Technique for Aerosol Retrievals Over Land from MODIS, in: Satellite aerosol remote sensing over land, edited by: Kokhanovky, A. and De Leeuw, G., Springer Praxis Books, IBSN: 978-3-540-69396-3, 69–99, 2009.

Maignan, F., Breon, F. M., and Lacaze, R.: Bidirectional reflectance of Earth targets: Evaluation of analytical models using a large set of spaceborne measurements with emphasis on the Hot Spot, Remote Sens. Environ., 90, 210–220, 2004.

Maignan, F., Breìon, F. M., Feìdelle, E., and Bouvier, M.: Polarized reflectances of natural surfaces: Spaceborne measurements and analytical modeling, Remote Sens. Environ., 113, 2642–2650, 2009.

Martonchik, J. V., Diner, D. J., Kahn, R., Verstraete, M. M., Pinty, B., Gordon, H. R., and Ackerman, T. P.: Techniques for the retrieval of aerosol properties over land and ocean using mul-tiangle data, IEEE T. Geosci. Remote, 36, 1212–1227, 1998.

Martonchik, J. V., Diner, D. J., Kahn, R. A., Gaitley, B., and Holben, B. N.: Comparison of MISR and AERONET aerosol optical depths over desert sites, Geophys. Res. Lett., 31, L16102, doi:10.1029/2004GL019807, 2004.

Mishchenko, M. I. and Travis, L. D.: Satellite retrieval of aerosol properties over the ocean using polarization as well as intensity of reflected sunlight, J. Geophys. Res., 102(D14), 16989–17013, 1997a.

Mishchenko, M. I., Travis, L. D., Kahn, R. A., et al.: Modeling phase functions for dustlike tropospheric aerosols using a shape mixture of randomly oriented polydisperse spheroids, J. Geophys. Res., 102, 16831–16847, 1997b.

Mishchenko, M. I., Geogdzhayev, I. V., Cairns, B., Rossow, W. B., and Lacis, A.: Aerosol retrievals over the oceans by use of channels 1 and 2 AVHRR data: Sensitivity analysis and preliminary results, Appl. Optics, 38, 7325–7341, 1999.

Mishchenko, M. I., Cairns, B., Kopp, G., Schueler, C. F., Fafaul, B. A., Hansen, J. E., Hooker, R. J., Itchkawich, T., Merimg, H. B., and Travis, L. D.: Accurate monitoring of terrestrial aerosol and total solar irradiance: introducing the Glory, Mission, B. Am. Meteorol. Soc., 88(N5), 677–691, 2007.

Nadal, F. and Breon, F.-M.: Parameterization of Surface Polarized Reflectance Derived from POLDER Spaceborne Measurements, IEEE T. Geosci. Remote, 37, 1709–1718, 1999.

AMTD

3, 4967–5077, 2010

Nakajima, T., Tanaka, M., and Yamauchi, T.: Retrieval of the optical properties of aerosols from aureole and extinction data, Appl. Optics, 22, 2951–2959, 1983.
Nakajima, T. and Tanaka, M.: Algorithms for radiative intensity calculations in moderately thick atmospheres using a truncation approximation, J. Quant. Spectrosc. Ra., 40, 51–69, 1988.
Nakajima, T., Tonna, G., Rao, R., Boi, P., Kaufman, Y., and Holben, B.: Use of sky bright-ness measurements from ground for remote sensing of particulate polydisper-sions, Appl. Optics, 35, 2672–2686, 1996.
Phillips, B. L.: A technique for numerical solution of certain integral equation of first kind, J. Assoc. Comp. Mach., 9, 84–97, 1962.
Pilewskie, P., Pommier, J., Bergstrom, R., Gore, W., Howard, S., Rabbette, M., Schmid, B., Hobbs, P. V., and Tsay, S. C.: Solar spectral radiative forcing during the Southern African Regional Science Initiative, J. Geophys. Res., 108, D138486, doi:10.1029/2002JD002411, 2003.
Rahman, H., Pinty, B., and Verstrate, S. C.: Coupled surface-atmosphere reflectance (CSAR) model 2. Semiempirical surface model usable with NOAA/AVHRAA data, J. Geophys. Res., 98, 20791–20801, 1993.
Rajot, J. L., Formenti, P., Alfaro, S., Desboeufs, K., Chevaillier, S., Chatenet, B., Gaudichet, A., Journet, E., Marticorena, B., Triquet, S., Maman, A., Mouget, N., and Zakou, A.: AMMA dust experiment: An overview of measurements performed during the dry season special observation period (SOP0) at the Banizoumbou (Niger) supersite, J. Geophys. Res., 113, D00C14, doi:10.1029/2008JD009906, 2008.
Reid, J. S., Halflidi, H., Maring, H. B., Smirnov, A., Savoie, D. L., Cliff, S. S., Reid, E. A., Livingston, J. M., Meier, M. M., Dubovik, O., and Tsay, S.-C.: Comparison of Size and Morphological Measurements of Coarse Mode Dust Particles from Africa, J. Geophys. Res., 108, 8593, doi:10.1029/2002JD002485, 2003.
Reid, J. S., Eck, T. F., Christopher, S. A., Koppmann, R., Dubovik, O., Eleuterio, D. P., Holben, B. N., Reid, E. A., and Zhang, J.: A review of biomass burning emissions part III: intensive optical properties of biomass burning particles, Atmos. Chem. Phys., 5, 827–849, doi:10.5194/acp-5-827-2005, 2005.
Remer, L. A., Kaufman, Y. J., Tanré, D., Mattoo, S., Chu, D. A., Martins, J. V., Li, R.-R., Ichoku, C., Levy, R. C., Kleidman, R. G., Eck, T. F., Vermote, E., and Holben, B. N.: The MODIS aerosol algorithm, products, and validation, J. Atmos. Sci., 62, 947–973, 2005.

AMTD
3, 4967–5077, 2010

Statistically optimized inversion algorithm for enhanced retrieval

O. Dubovik et al.

Rodgers, C. D.: Inverse methods for atmospheric sounding: theory and practice, World Scientific, Singapore, 2000.
Rondeaux, G. and Herman, M.: Polarization of light reflected by crop canopies, Remote Sens. Environ., 38, 63–75, 1991.
Ross, J. K.: The radiation regime and architecture of plant stands, Dr. W. Junk Publishers, The Hague, 1981.
Rozanov, V. V. and Lyapustin, A. I.: Similarity of radiative transfer equation: Error analysis of phase function truncation techniques, J. Quant. Spectrosc. Ra., 111, 1964–1979, 2010.
Schmid, B., Redemann, J., Russell, P. B., Hobbs, P. V., Hlavka, D. L., McGill, M. J., Holben, B. N., Welton, E. J., Campbell, J. R., Torres, O., Kahn, R. A., Diner, D. J., Helmlinger, M. C., Chu, D. A., Robles-Gonzalez, C., and de Leeuw, G.: Coordinated airborne, spaceborne, and ground-based measurements of massive thick aerosol layers during the dry season in southern Africa, J. Geophys. Res., 108(D13), 8496, doi:10.1029/2002JD002297, 2003.
Sinuyk, A., Dubovik, O., Holben, B. N., Eck, T. F., Breon, F.-M., Martonchik, J., Kahn, R., Diner, D. J., Vermote, E. F., Roger, J.-C., Lapyonok, T., and Slutser, I.: Simultaneous retrieval of aerosol and surface properties from a combination of AERONET and satellite data, Remote Sens. Environ., 107, 90–108, doi:10.1016/j.rse.2006.07.02, 2007.
Smirnov, A., Holben, B. N., Eck, T. F., Dubovik, O., and Slutsker, I.: Cloud screening and quality control algorithms for the AERONET data base, Remote Sens. Environ., 73, 337–349, 2000.
Sokolik, I. N. and Toon, O. B.: Incorporation of mineralogical composition into models of the radiative properties of mineral aerosol from UV to IR wavelengths, J. Geophys. Res., 104, 9423–9444, 1999.
Sow, M., Alfaro, S. C., Rajot, J. L., and Marticorena, B.: Size resolved dust emission fluxes measured in Niger during 3 dust storms of the AMMA experiment, Atmos. Chem. Phys., 9, 3881–3891, doi:10.5194/acp-9-3881-2009, 2009.
Stowe, L. L., Ignatov, A. M., and Sigh, R. R.: Development, validation,and potential enhancements to the second-generation operational aerosol product at the National Environmental Satellite, Data, and Information Service of the National Oceanic and Atmospheric Administration, J. Geophys. Res., 102, 16923–16932, 1997.
Tanré, D., Kaufman, Y. J., Herman, M., and Mattoo, S.: Remote sensing of aerosol properties over oceans using the MODIS/EOS spectral radiances, J. Geophys. Res., 102(D14), 16971–16988, 1997.

AMTD
3, 4967–5077, 2010

Tikhonov, A. N.: On the solution of incorrectly stated problems and a method of regu-larization, Dokl. Akad. Nauk SSSR, 151, 501–504, 1963.

Torres, O., Bhartia, P. K., Herman, J. R., Ahmad, Z., and Gleason, J.: Derivation of aerosol properties from satellite measurements of backscattered ultraviolet radiation: Theoretical basis, J. Geophys. Res., 103, 17099–17110, 1998.

Twomey, S.: On the numerical solution of Fredholm integral equations of the first kind by the inversion of the linear system produced by quadrature, J. Assoc. Comp. Mach., 10, 97–101, 1963.

Veselovskii, I., Dubovik, O., Kolgotin, A., Lapyonok, T., Di Girolamo, P., Summa, D., Whiteman, D. N., Mishchenko, M., and Tanré, D.: Application of randomly oriented spheroids for retrieval of dust particle parameters from multi-wavelength lidar measurements, J. Geophys. Res., 115, D21203, doi:10.1029/2010JD014139, 2010.

Volten, H., Munoz, O., Rol, E., de Haan, J. F., Vassen, W., Hovenier, J. W., Muinonen, K., and Nousiainen, T.: Scattering matrices of mineral aerosol particles at 441.6 nm and 632.8 nm, J. Geophys. Res., 106, 17375–17401, 2001.

Wagner, S. C., Govaerts, Y. M., and Lattanzio, A.: Joint retrieval of surface reflectance and aerosol optical depth from MSG/SEVIRI observations with an optimal estimation approach: 2. Implementation and evaluation, J. Geophys. Res., 115, D02204, doi:10.1029/2009JD011780, 2010.

Wanner, W., Li, X., and Strahler, A. H.: On the derivation of kernels for kernel-driven models of bidirectional reflectance, J. Geophys. Res., 100(D10), 21077–21089, 1995.

Waquet, F., Goloub, P., Deuze, J.-L., Leon, J.-F., Auriol, F., Verwaerde, C., Balois, J.-Y., and Francois, P.: Aerosol retrieval over land using a multiband polarimeter and comparison with path radiance method, J. Geophys. Res., 112, D11214, doi:10.1029/2006JD008029, 2007.

Waquet, F., Cairns, B., Knobelspiesse, K., Chowdhary, J., Travis, L. D., Schmid, B., and Mishchenko, M. I.: Polarimetric remote sensing of aerosols over land, J. Geophys. Res., 114, D01206, doi:10.1029/2008JD010619, 2009a.

Waquet, F., Leon, J.-F., Cairns, B., Goloub, P., Deuze, J.-L., and Auriol, F.: Analysis of the spectral and angular response of the vegetated surface polarization for the purpose of aerosol remote sensing over land, Appl. Optics, 48, 1228–1236, 2009b.

AMTD

3, 4967–5077, 2010

Statistically optimized inversion algorithm for enhanced retrieval

O. Dubovik et al.

Table 1. List of measured and retrieved characteristics considered in POLDER/PARASOL algorithm.

POLDER/PARASOL measurements	
MESUREMENT TYPE:	
$I(\mu_0;\mu_1;\varphi_0;\varphi_1;\lambda_i) = I(\Theta_j;\ \lambda_i)$	– I reflected total radiances ;
$Q(\mu_0;\mu_1;\varphi_0;\varphi_1;\lambda_i) = Q(\Theta_j;\ \lambda_i)$	– Q component of polarized reflected radiances;
$U(\mu_0;\mu_1;\varphi_0;\varphi_1;\lambda_i) = U(\Theta_j;\ \lambda_i)$	– U component of polarized reflected radiances;
OBSERVATION SPECIFICATIONS:	
ANGULAR:	
$I(\Theta_j;\ \lambda_i)$, $Q(\Theta_j;\ \lambda_i)$ and $U(\Theta_j;\ \lambda_i)$ measured in up to 16 viewing directions, that may cover the range of scattering angle Θ from $\sim 80^\circ$ to 180°.	
SPECTRAL:	
$I(\Theta_j;\ \lambda_i)$ measured in 6 window channels $\lambda_i = 0.44$, 0.49, 0.565, 0.675, 0.87, and 1.02 µm	
$Q(\Theta_j;\ \lambda_i)$ and $U(\Theta_j;\ \lambda_i)$ measured in 3 window channels $\lambda_i = 0.49$, 0.675 and 0.87 µm	
Retrieved characteristics	
AEROSOL PARAMETERS:	
C_v	– total volume concentration of aerosol (µm^3/µm^2);
$dV(r_i)/d\ln r$	– ($i = 1, ..., N_r$) values of volume size distribution in N_r size bins r_i, normalized by C_v;
C_{sph}	– faction of spherical particles
$n(\lambda_i)$	– ($i = 1, ..., N_\lambda$) the real part of the refractive index at every λ_i of the POLDER/PARASOL sensor;
$k(\lambda_i)$	– ($i = 1, ..., N_\lambda$) the imaginary part of the refractive index at every λ_i of the POLDER/PARASOL sensor;
h_0	– mean height of aerosol layer.
Option: algorithm allows the retrieval of multi-component aerosol. In that case, all above parameters are retrieved for each aerosol component	
SURFACE REFLECTION PARAMETERS:	
Rahman et al. (1993) MODEL:	
$\rho_o(\lambda_i)$	– ($i = 1, ..., N_\lambda$) first RPV BRF parameter (characterizes intensity of reflectance);
$\kappa(\lambda_i)$	– ($i = 1, ..., N_\lambda$) second RPV BRF parameter (characterizes anisotropy of reflectance);
$\Theta(\lambda_i)$	– ($i = 1, ..., N_\lambda$) third RPV BRF parameter (characterizes forward/backscattering contributions)
$h_0(\lambda_i)$	– ($i = 1, ..., N_\lambda$) fourth RPV BRF parameter (characterizes hot spot effect)
NOTE: $h_0(\lambda)$ is retrieved only for the observation conditions: $\pm 7.5^\circ$ close to backscattering. In other situations, it is fixed as related to $h_0(\lambda) = \rho_0(\lambda)$.	
Maignan et al. (2009) MODEL:	
$B(\lambda_i)$	– ($i = 1, ..., N_\lambda$) free parameter;
Option: algorithm allows using alternative surface models: Ross-Li model for BRF and Nadal-Breon model for BPRF.	

AMTD

3, 4967–5077, 2010

Statistically optimized inversion algorithm for enhanced retrieval

O. Dubovik et al.

Title Page
Abstract | Introduction
Conclusions | References
Tables | Figures
◀I | ▶I
◀ | ▶
Back | Close
Full Screen / Esc
Printer-friendly Version
Interactive Discussion

Table 2. Definition of the measurement vector $\boldsymbol{f}^*$ and the vector of unknowns $\boldsymbol{a}$.

	$\boldsymbol{f}^*$ – vector of measurements:	
$\{\boldsymbol{f}^*_{\mathrm{I}}\}_i = \ln\left(I\left(\Theta_j;\, \lambda_i\right)\right)$, where $I\left(\Theta_j;\, \lambda_i\right)$ is total radiance observed by POLDER/PARASOL;		
$\{\boldsymbol{f}^*_{\mathrm{P}}\}_i = \ln\left(P\left(\Theta_j;\, \lambda_i\right)\right)$, where $P\left(\Theta_j;\, \lambda_i\right) = \frac{\sqrt{\left(Q(\Theta_j;\, \lambda_i)\right)^2 + \left(U(\Theta_j;\, \lambda_i)\right)^2}}{I\left(\Theta_j;\, \lambda_i\right)}$ is degree of linear polarization obtained from POLDER/PARASOL observations;		
	$\boldsymbol{a}$ – vector of unknowns	
Notation	Definition	Variability limits
	AEROSOL parameters:	
$\boldsymbol{a}_{\mathrm{v}}$	$\{\boldsymbol{a}_{\mathrm{v}}\}_i = \ln\left(\frac{dV(r_i)}{d\ln r}\right)$, $i = 1, ..., N_{\mathrm{r}}$	$0.00001 \leq \frac{dV(r_i)}{d\ln r}$
a_{Vc}	$a_{\mathrm{Vc}} = \ln(C_{\mathrm{v}})$	$0.001 \leq C_{\mathrm{v}} \leq 5.0\ \left(\mu\mathrm{m}^3/\mu\mathrm{m}^2\right)$
a_{sph}	$a_{\mathrm{sph}} = \ln(C_{\mathrm{sph}})$	$0.001 \leq C_{\mathrm{sph}} \leq 1.0$
$\boldsymbol{a}_n$	$\{\boldsymbol{a}_n\}_i = \ln(n(\lambda_i))$, $i = 1, ..., N_\lambda$	$1.33 \leq n(\lambda_i) \leq 1.6$
$\boldsymbol{a}_{\mathrm{k}}$	$\{\boldsymbol{a}_k\}_i = \ln(k(\lambda_i))$, $i = 1, ..., N_\lambda$	$0.0005 \leq k(\lambda_i) \leq 0.1$
	Surface BRF and BPRF parameters:	
$\boldsymbol{a}_{\mathrm{brf},1}$	$\{\boldsymbol{a}_{\mathrm{brf},1}\}_i = \ln(\rho_0(\lambda_i))$, $i = 1, ..., N_\lambda$	$0.001 \leq \rho_0(\lambda_i) \leq 0.7$
$\boldsymbol{a}_{\mathrm{brf},2}$	$\{\boldsymbol{a}_{\mathrm{brf},2}\}_i = \ln(\kappa(\lambda_i))$, $i = 1, ..., N_\lambda$	$0.1 \leq \kappa(\lambda_i) \leq 1.0$
$\boldsymbol{a}_{\mathrm{brf},3}$	$\{\boldsymbol{a}_{\mathrm{brf},3}\}_i = \ln(1 + \Theta(\lambda_i))$, $i = 1, ..., N_\lambda$	$-0.5 \leq \Theta(\lambda_i) \leq 0.5$
$\boldsymbol{a}_{\mathrm{brf},4}$	$\{\boldsymbol{a}_{\mathrm{brf},4}\}_i = \ln(h_0(\lambda_i))$, $i = 1, ..., N_\lambda$	$0.001 \leq h_0(\lambda_i) \leq 0.7$
$\boldsymbol{a}_{\mathrm{bprf}}$	$\{\boldsymbol{a}_{\mathrm{bprf}}\}_i = \ln(B(\lambda_i))$, $i = 1, ..., N_\lambda$	$0.01 \leq B(\lambda_i) \leq 10.0$

AMTD

3, 4967–5077, 2010

Statistically optimized inversion algorithm for enhanced retrieval

O. Dubovik et al.

Table 3. The finite differences used for smoothness constrains and the correspondent values of Lagrange multipliers $\gamma_{\Delta,i}$.

	Order of finite differences	Values of $\gamma_{\Delta,i}$
AEROSOL:		
$dV(r_i)/d\ln r$ ($i = 1, ..., N_r$)	3	0.005
$n(\lambda_i)$ ($i = 1, ..., N_\lambda$)	1	0.1
$k(\lambda_i)$ ($i = 1, ..., N_\lambda$)	2	0.01
Surface BRF:		
$\rho_o(\lambda_i)$ ($i = 1, ..., N_\lambda$)	3	0.005
$\kappa(\lambda_i)$ ($i = 1, ..., N_\lambda$)	1	0.1
$\Theta(\lambda_i)$ ($i = 1, ..., N_\lambda$)	1	0.1
$h_0(\lambda_i)$ ($i = 1, ..., N_\lambda$)	2	0.01
Surface BPRF:		
$B(\lambda_i)$ ($i = 1, ..., N_\lambda$)	1	0.1

AMTD

3, 4967–5077, 2010

Statistically optimized inversion algorithm for enhanced retrieval

O. Dubovik et al.

Table 4. The types of the finite differences and the correspondent values of Lagrange multipliers $\gamma_{\Delta,i}$ used in the algorithm for applying inter-pixel smoothness constrains.

	Order of finite differences		Values of $\gamma_{\Delta,i}$	
	horizontal (x, y) continuity	temporal (t) continuity	horizontal (x, y) continuity	temporal (t) continuity
AEROSOL:				
C_v	2	–	0.01	–
$dV(r_i)/d\ln r$ $(i=1, ..., N_r)$	1	–	0.1	–
C_{sph}	1	–	0.1	–
h_a	1	–	0.1	–
$n(\lambda_i)$ $(i=1, ..., N_\lambda)$	1	–	0.1	–
$k(\lambda_i)$ $(i=1, ..., N_\lambda)$	1	–	0.1	–
Surface BRF:				
$\rho_o(\lambda_i)$ $(i=1, ..., N_\lambda)$	–	3	–	0.1
$\kappa(\lambda_i)$ $(i=1, ..., N_\lambda)$	–	1	–	0.1
$\Theta(\lambda_i)$ $(i=1,..., N_\lambda)$	–	1	–	0.1
$h_0(\lambda_i)$ $(i=1, ..., N_\lambda)$	–	2	–	0.1
Surface BPRF:				
$B(\lambda_i)$ $(i=1, ..., N_\lambda)$	–	1	–	0.1

AMTD
3, 4967–5077, 2010

Table 5. Summary of the a priori assumptions applied for constraining of each element of the vector of unknowns.

AEROSOL:		
Parameter:	Single–Pixel constraints	Inter–Pixel constraints
C_v	no	t – no; X – mild; Y – mild
$dV(r_i)/d\ln r$	weak size smoothness	t – constant during 7 days; *X–Y (horizontal)* – mild
$n(\lambda_i)$	strong spectral smoothness	t – constant during 7 days; *X–Y (horizontal)* – mild
$k(\lambda_i)$	mild spectral smoothness	t – constant during 7 days; *X–Y (horizontal)* – mild
SURFACE REFLECTANCE:		
Parameter:	Single–Pixel constraints	Inter–Pixel constraints
$\rho_o(\lambda_i)$	weak spectral smoothness	t – constant during 7 days; *X–Y (horizontal)* – mild
$\kappa(\lambda_i)$	strong spectral smoothness	t – constant during 7 days; *X–Y (horizontal)* – mild
$\Theta(\lambda_i)$	strong spectral smoothness	t – constant during 7 days; *X–Y (horizontal)* – mild
$h_0(\lambda_i)$	weak spectral smoothness	t – constant during 7 days; *X–Y (horizontal)* – mild
$B(\lambda_i)$	strong spectral smoothness	t – constant during 7 days; *X–Y (horizontal)* – mild

AMTD
3, 4967–5077, 2010

Table 6. Definition of " the initial guess" of the vector of unknowns.

Aerosol Properties	Surface Reflectance
$C_v = C_0$ (corresponding to the value of τ_{aer} (0.44)~0.05);	$\rho_o(\lambda_i) = 0.05$ ($i = 1, ..., N_\lambda$)
$dV(r_i)/d\ln r = 0.1$; ($i = 1, ..., N_r$)	$\kappa(\lambda_i) = 0.75$ ($i = 1, ..., N_\lambda$)
$C_{sph} = 0.7$	$\Theta(\lambda_i) = -0.1$ ($i = 1, ..., N_\lambda$)
$n(\lambda_i) = 1.4$ ($i = 1, ..., N_\lambda$)	$h_0(\lambda_i) = \rho_o(\lambda_i)$ ($i = 1, ..., N_\lambda$)
$k(\lambda_i) = 0.005$ ($i = 1, ..., N_\lambda$)	$B(\lambda_i) = 0.03$ ($i = 1, ..., N_\lambda$)

AMTD
3, 4967–5077, 2010

Table 7. The summary of the sensitivity tests for aerosol retrievals from simulations mimicking POLDER observations over Mongu (Zambia) and over Banizoumbou (Niger) with the added random noise at the level of standard deviation $\sigma = 1\%$ for total radiances and $\sigma = 0.5\%$ for polarized radiances.

	Biomass over Mongu (Zambia)		Desert dust over Banizoumbou (Niger)	
$\left\lvert \frac{\Delta\tau}{\tau}(0.44) \right\rvert$	$\tau(0.44) \geq \sim 0.1$ $\leq \sim 20\%$	$\tau(0.44) \geq \sim 0.5$ $\leq \sim 15\%$	$\tau(0.44) \geq \sim 0.1$ $\leq \sim 25\%$	$\tau(0.44) \geq \sim 0.5$ $\leq \sim 20\%$
$\lvert \Delta\omega_0(0.44) \rvert$	$\tau(0.44) \geq \sim 0.5$ $\leq \sim 0.02$	$\tau(0.44) \geq \sim 1.0$ $\leq \sim 0.01$	$\tau(0.44) \geq \sim 0.5$ $\leq \sim 0.02$	$\tau(0.44) \geq \sim 1.0$ $\leq \sim 0.015$
$\left\lvert \frac{\Delta\tau}{\tau}(1.02) \right\rvert$	$\tau(1.02) \geq \sim 0.1$ $\leq \sim 25\%$	$\tau(1.02) \geq \sim 0.3$ $\leq \sim 20\%$	$\tau(1.02) \geq \sim 0.1$ $\leq \sim 25\%$	$\tau(0.44) \geq \sim 0.5$ $\leq \sim 20\%$
$\lvert \Delta\omega_0(1.02) \rvert$	$\tau(1.02) \geq \sim 0.1$ $\leq \sim 0.04$	$\tau(1.02) \geq \sim 0.1$ $\leq \sim 0.02$	$\tau(1.02) \geq \sim 0.5$ $\leq \sim 0.01$	$\tau(0.44) \geq \sim 1.0$ $\leq \sim 0.005$

AMTD
3, 4967–5077, 2010

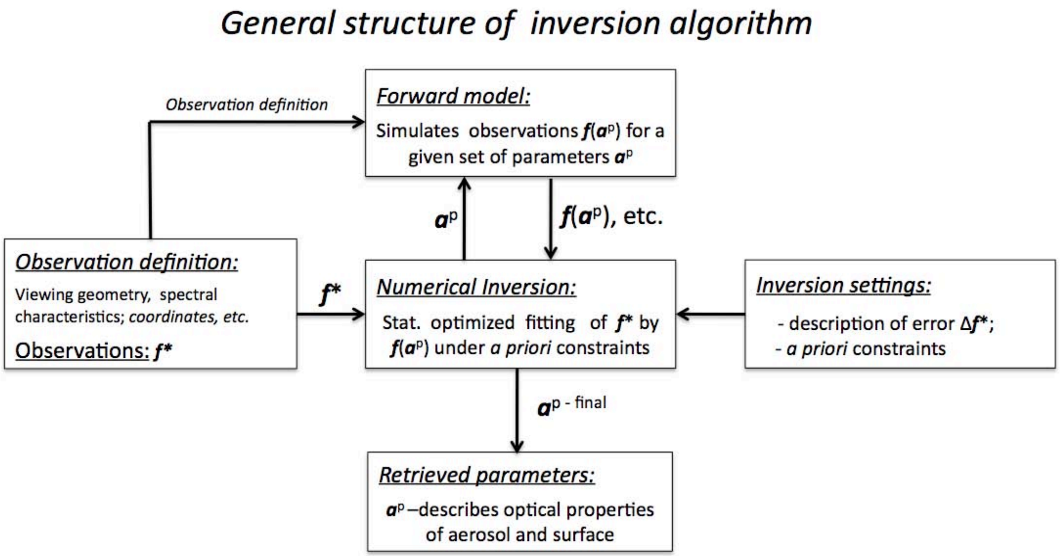

Fig. 1. The general structure of the retrieval algorithm.

AMTD
3, 4967–5077, 2010

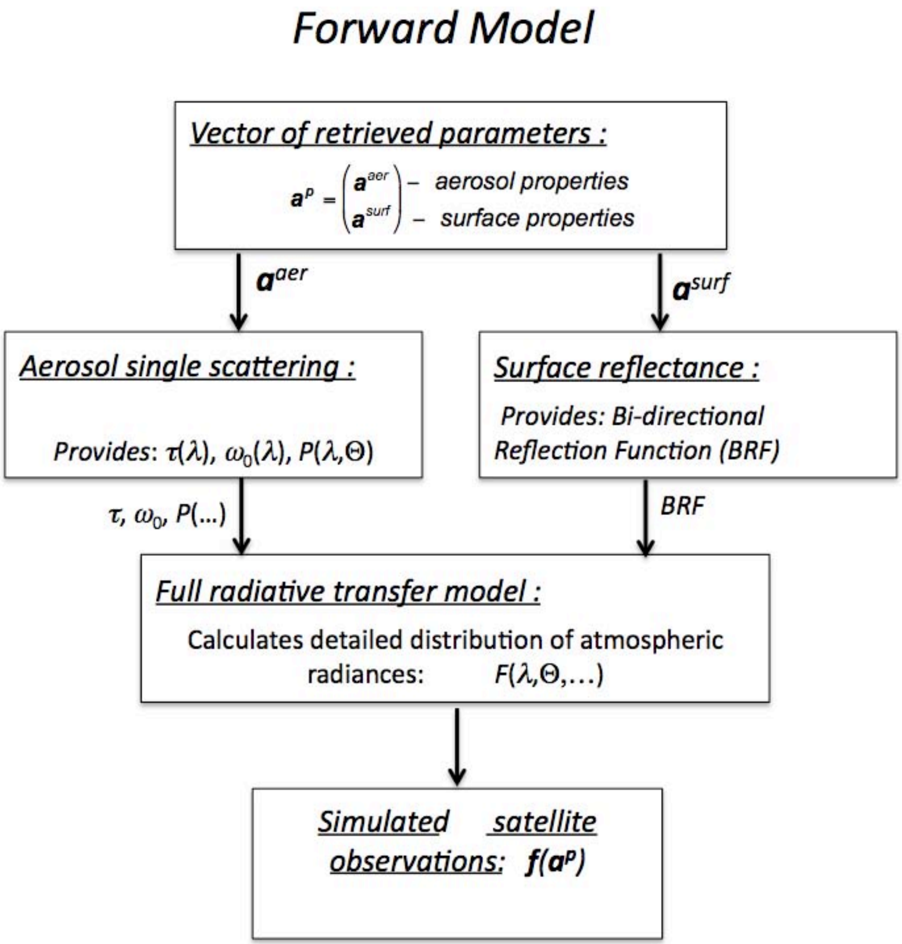

Fig. 2. The organization of the forward calculations of atmospheric radiance measured from a satellite.

AMTD
3, 4967–5077, 2010

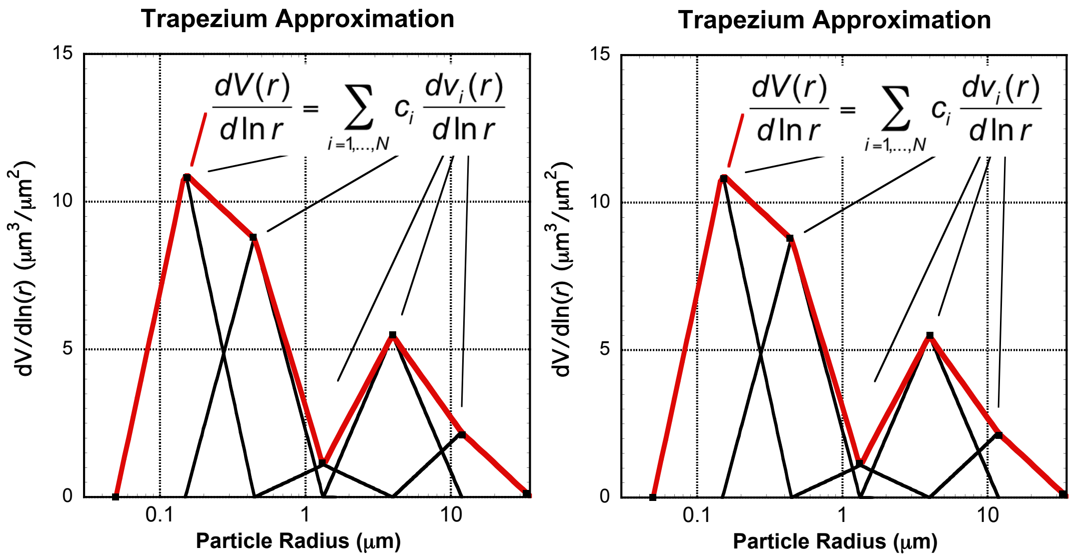

Fig. 3. The illustration of modeling aerosol size distribution by five ($N_r = 5$) triangular (left) or log-normal (right) size bins.

AMTD
3, 4967–5077, 2010

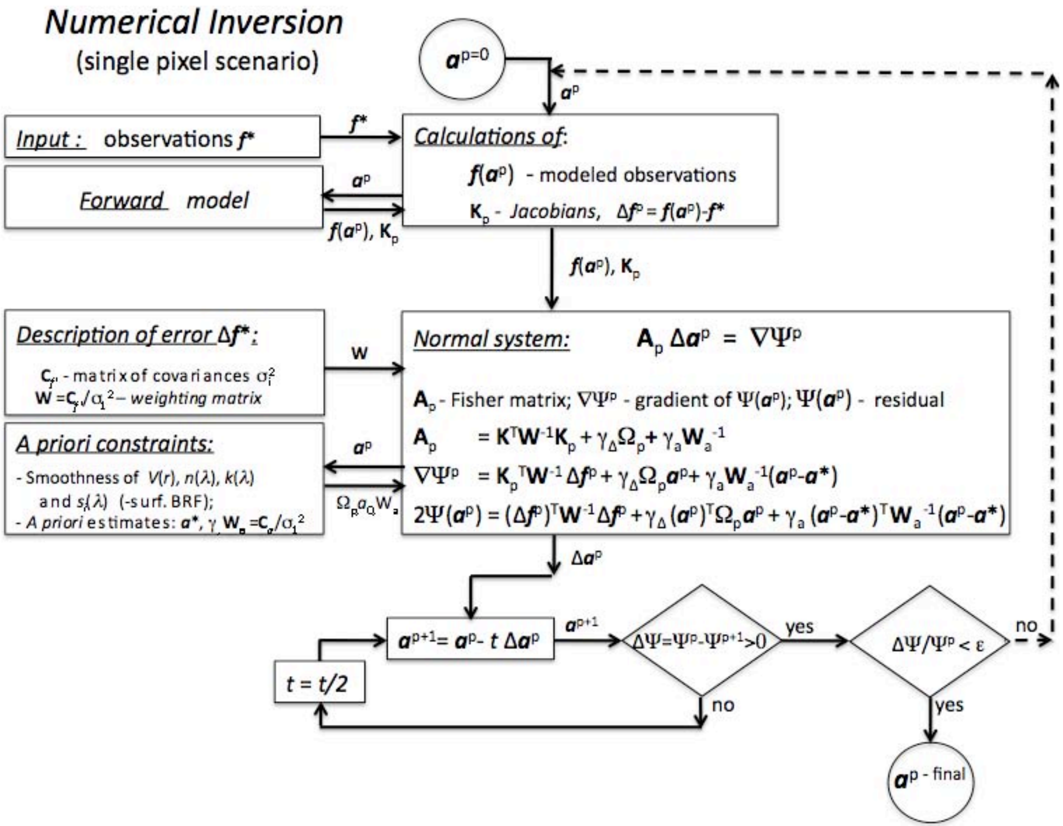

Fig. 4. The general structure of the numerical inversion data flow implemented for the retrieval of aerosol over single pixel.

AMTD

3, 4967–5077, 2010

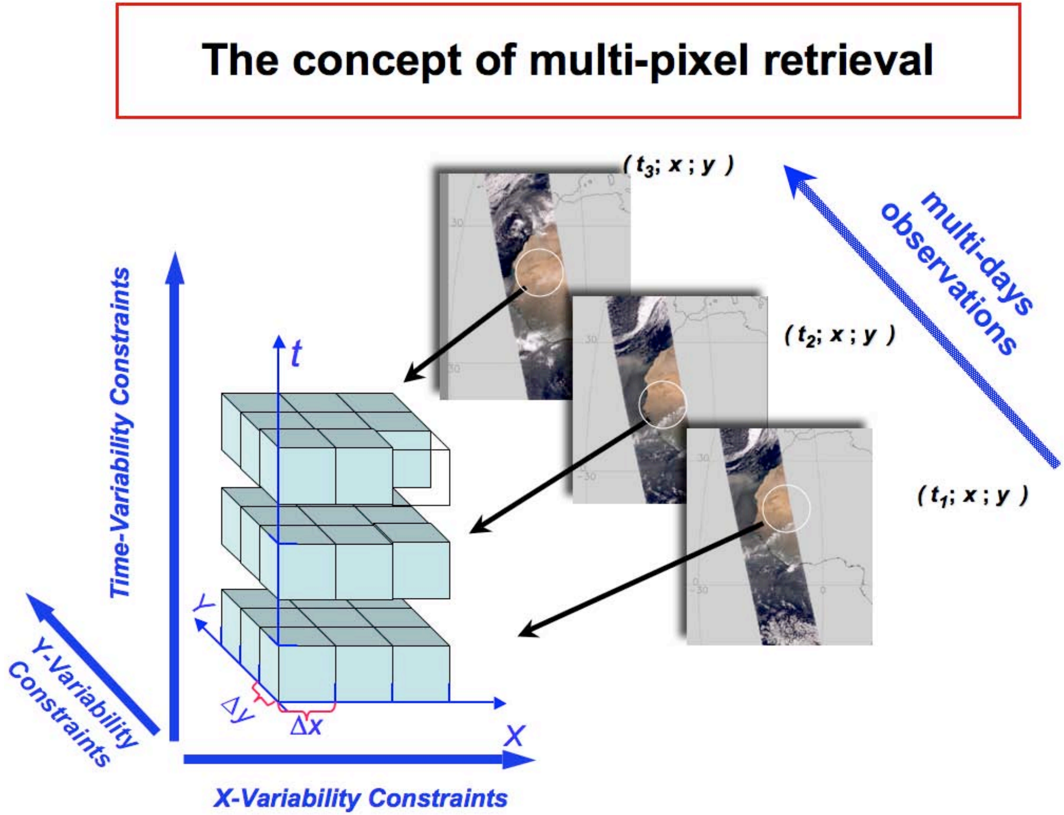

Fig. 5. The diagram illustrates the approach for retrieval aerosol from multiple pixels of POLDER/PARASOL.

AMTD
3, 4967–5077, 2010

Statistically optimized inversion algorithm for enhanced retrieval

O. Dubovik et al.

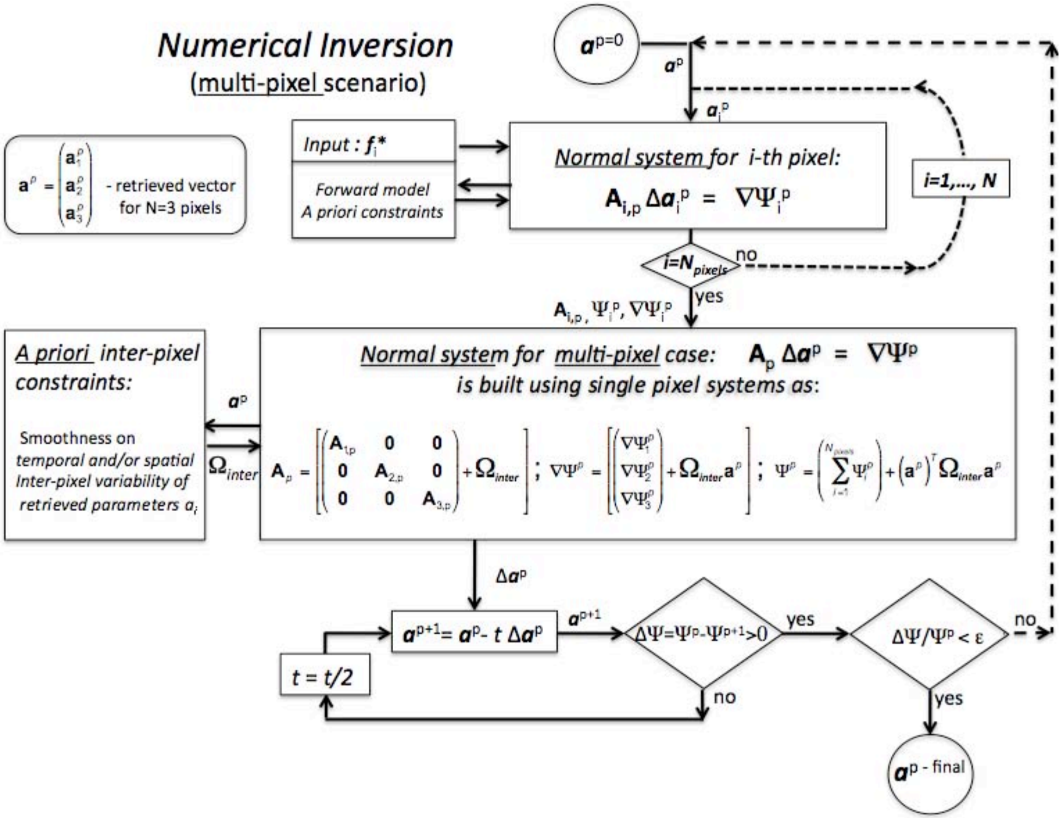

Fig. 6. The diagram illustrating the numerical inversion data flow implemented for the simultaneous retrieval of aerosol properties over multiple pixels.

AMTD
3, 4967–5077, 2010

Statistically optimized inversion algorithm for enhanced retrieval

O. Dubovik et al.

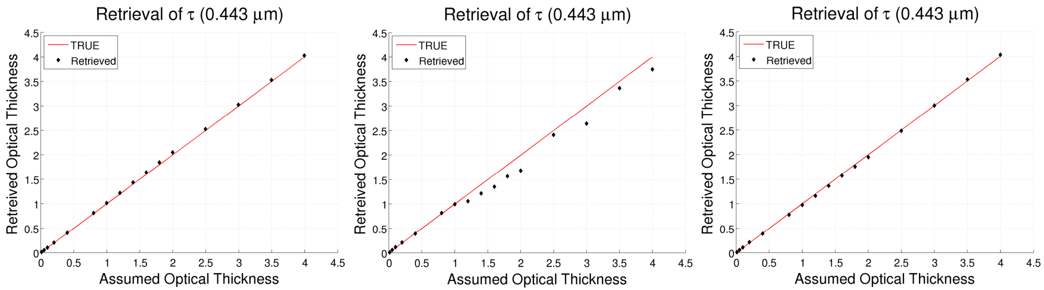

Fig. 7. Retrieval of biomass burning optical thickness over Mongu: (left) Single- pixel retrieval with no noise added; (center) Single-pixel retrieval with the random noise added; (right) Multi-pixel retrieval with the random noise added.

AMTD
3, 4967–5077, 2010

Statistically optimized inversion algorithm for enhanced retrieval

O. Dubovik et al.

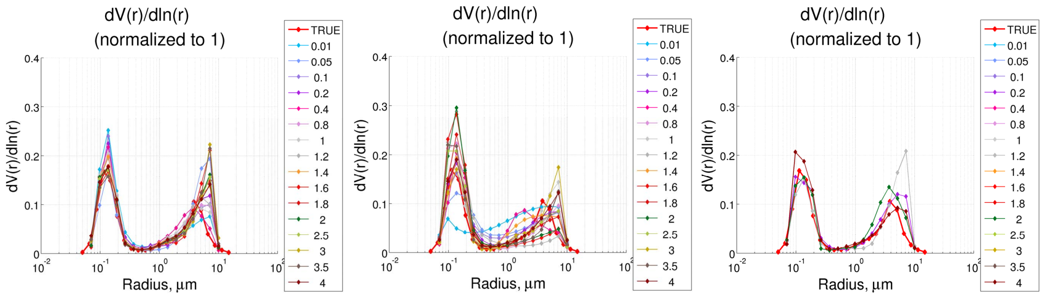

Fig. 8. Retrieval of biomass burning size distribution over Mongu: (left) Single- pixel retrieval with no noise added; (center) Single-pixel retrieval, with the random noise added; (right) Multi-pixel retrieval, with the random noise added.

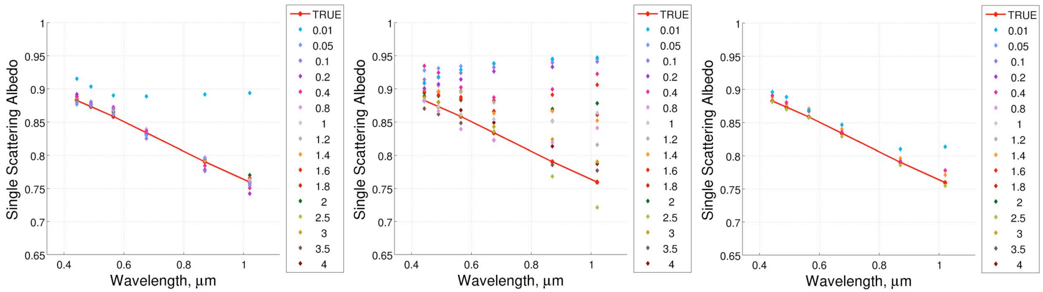

Fig. 9. Retrieval of biomass burning single scattering albedo over Mongu: (left) Single-pixel retrieval with no noise added; (center) Single-pixel retrieval with the random noise added; (right) Multi-pixel retrieval with the random noise added.

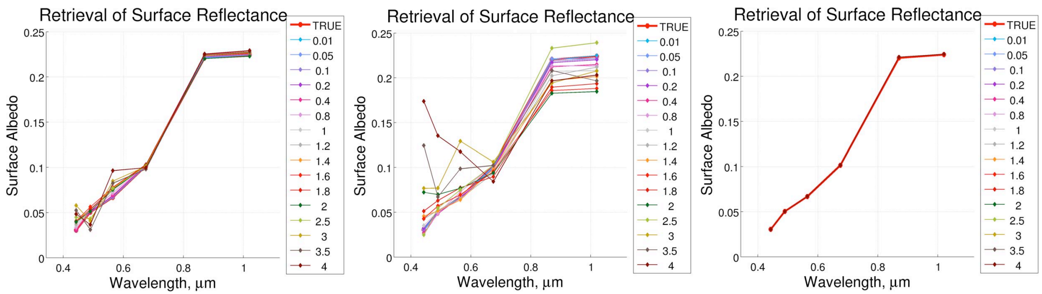

Fig. 10. Retrieval of the surface albedo over Mongu: (left) Single-pixel retrieval with no noise added; (center) Single-pixel retrieval with the random noise added; (right) Multi-pixel retrieval with the random noise added.

AMTD

3, 4967–5077, 2010

Statistically optimized inversion algorithm for enhanced retrieval

O. Dubovik et al.

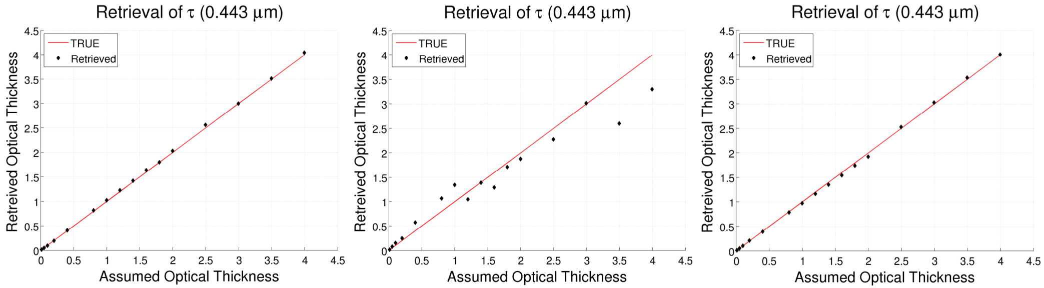

Fig. 11. Retrieval of desert dust optical thickness over Banizoumbou: (left) Single pixel retrieval with no noise added; (center) Single-pixel retrieval with the random noise added; (right) Multi-pixel retrieval with the random noise added.

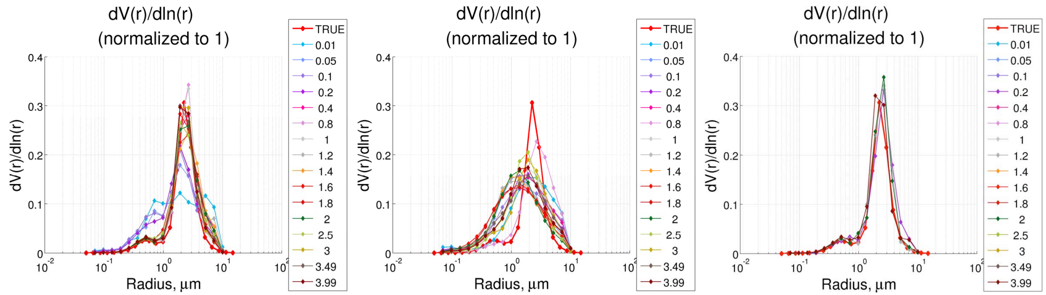

Fig. 12. Retrieval of desert dust size distribution over Banizoumbou: (left) Single pixel retrieval with no noise added; (center) Single-pixel retrieval, with the random noise added; (right) Multi-pixel retrieval with the random noise added.

AMTD
3, 4967–5077, 2010

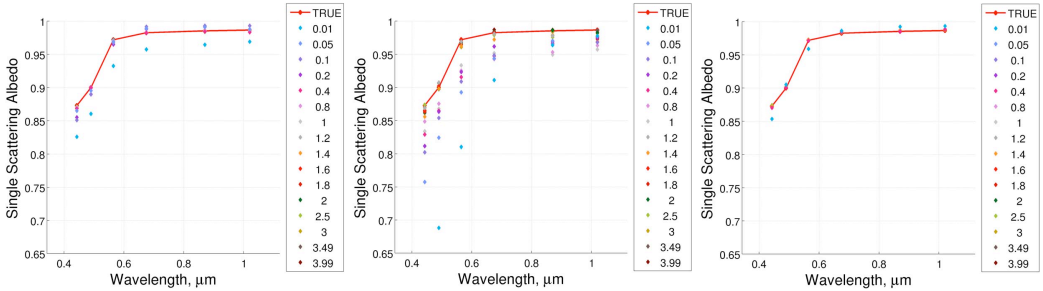

Fig. 13. Retrieval of desert dust single scattering albedo over Banizoumbou: (left) Single pixel retrieval with no noise added; (center) Single-pixel retrieval with the random noise added; (right) Multi-pixel retrieval with the random noise added.

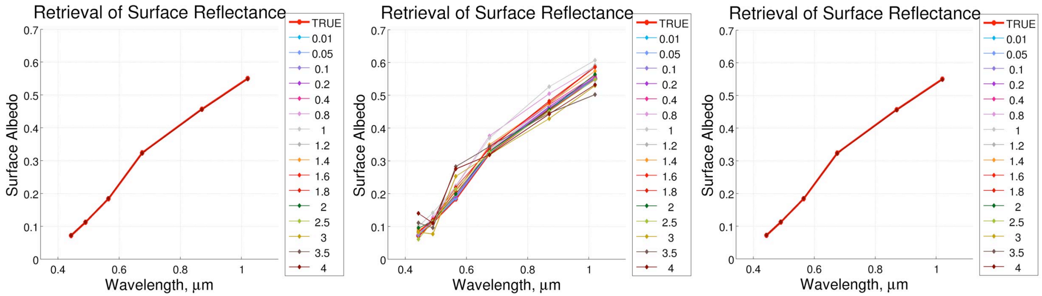

Fig. 14. Retrieval of surface albedo over Banizoumbou: (left) Single-pixel retrieval with no noise added; (center) Single-pixel retrieval with the random noise added; (right) Multi-pixel retrieval with the random noise added.

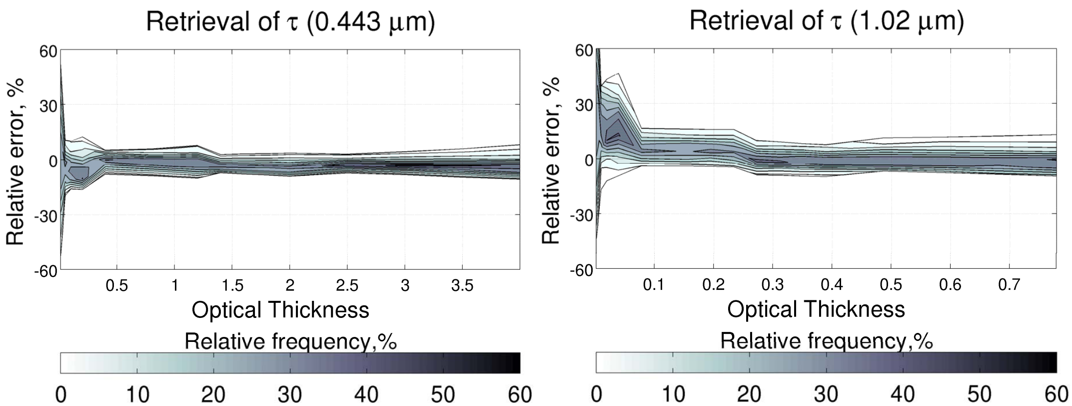

Fig. 15. Statistics of the retrieval errors of biomass burning optical thickness over Mongu in the series of the numerical tests for 100 different realizations of random noise added (multi-pixel retrieval): (left) 0.44 μm; (right) 1.02 μm.

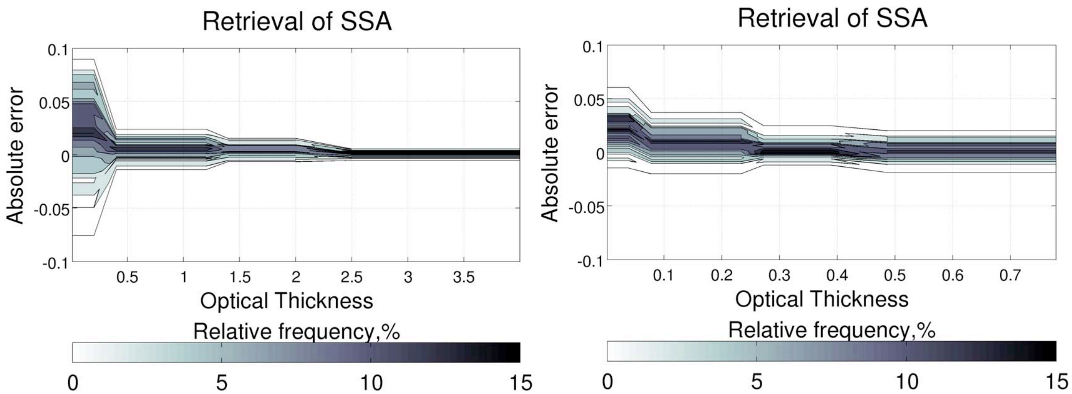

Fig. 16. Statistics of the retrieval errors of biomass burning single scattering albedo over Mongu in the series of the numerical tests for 100 different realizations of random noise added (multi-pixel retrieval): (left) 0.44 µm; (right) 1.02 µm.

AMTD
3, 4967–5077, 2010

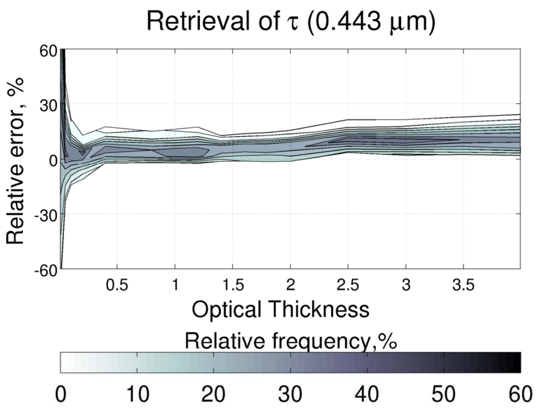

Fig. 17. Statistics of the retrieval errors of desert dust optical thickness over Banizoumbou in the series of the numerical tests for 100 different realizations of random noise added (multi-pixel retrieval): (left) 0.44 μm; (right) 1.02 μm.

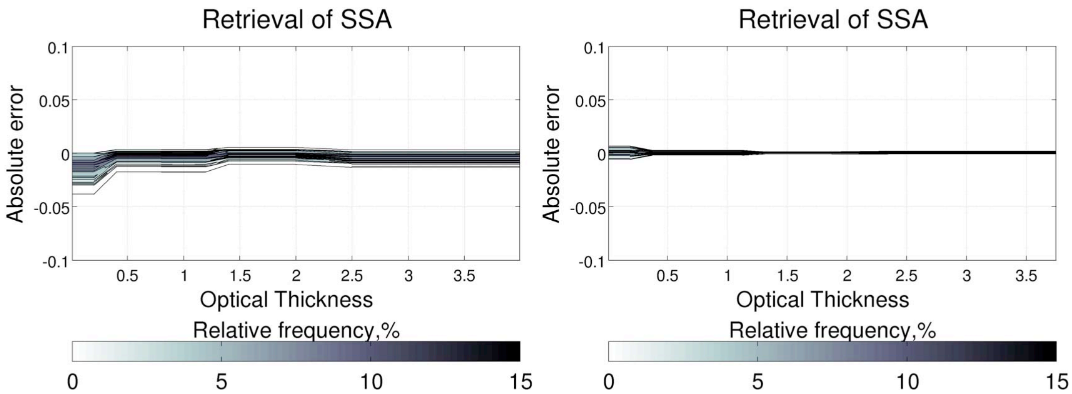

Fig. 18. Statistics of the retrieval errors of desert dust single scattering albedo over Banizoumbou in the series of the numerical tests for 100 different realizations of random noise added (multi-pixel retrieval): (left) 0.44 µm; (right) 1.02 µm.

AMTD
3, 4967–5077, 2010

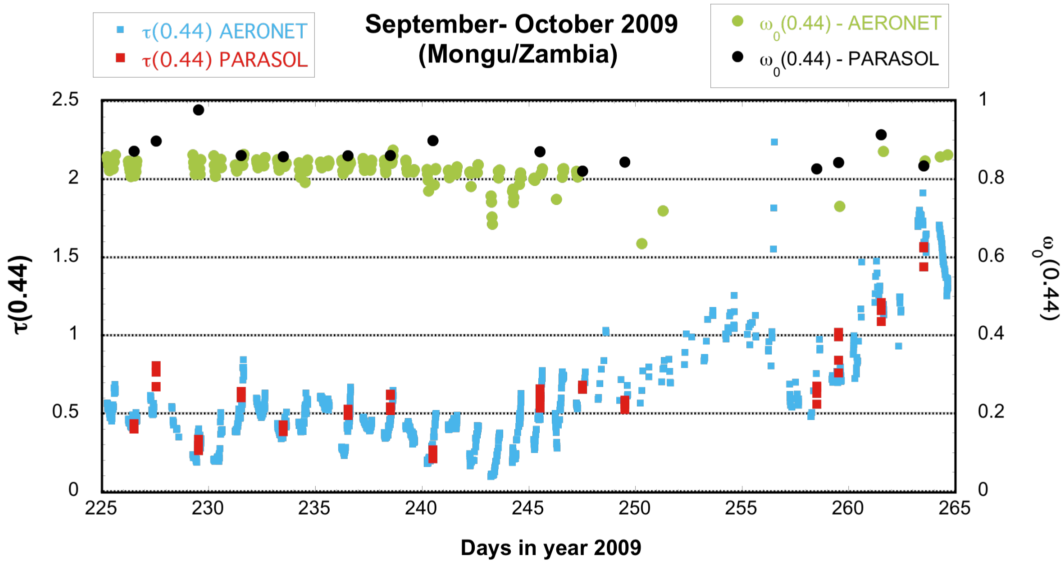

Fig. 19. The comparison of $\tau(0.44)$ and $\omega_0(0.44)$ retrieved from POLDER/PARASOL during September–October 2009 over Mongu with the correspondent values provided by AERONET.

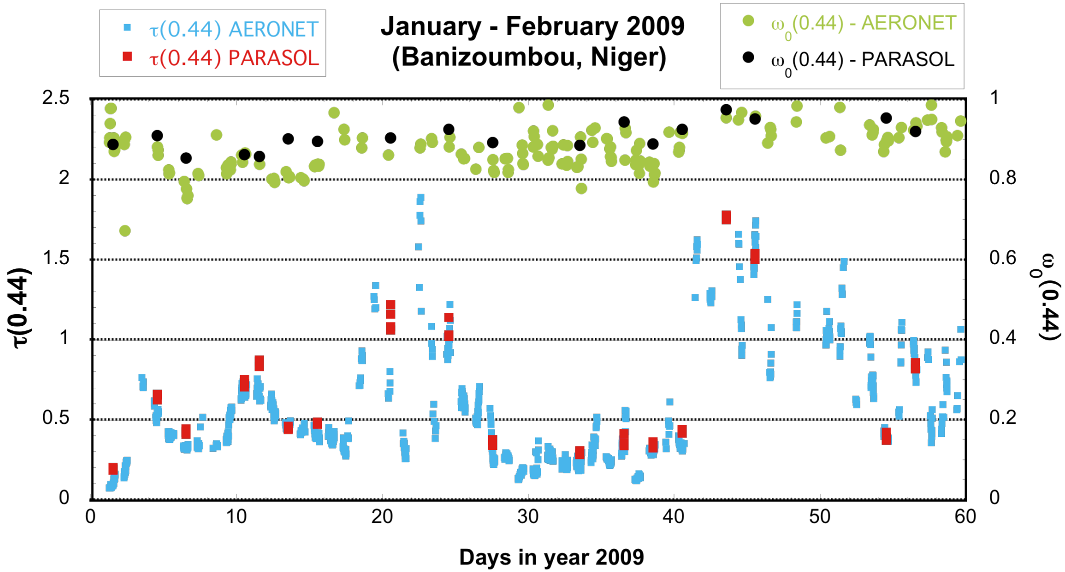

Fig. 20. The comparison of $\tau(0.44)$ and $\omega_0(0.44)$ retrieved from POLDER/PARASOL during January–February 2009 over Banizoumbou with the correspondent values provided by AERONET.